MULTIBAND ORTHOGONAL FREQUENCY DIVISION MULTIPLEXING FOR ULTRA-WIDEBAND WIRELESS COMMUNICATION: ANALYSIS, EXTENSIONS, AND IMPLEMENTATION ASPECTS

by

CHRISTOPHER SNOW

B.E.Sc., The University of Western Ontario, 2003
B.Sc., The University of Western Ontario, 2003

A THESIS SUBMITTED IN PARTIAL FULFILLMENT OF
THE REQUIREMENTS FOR THE DEGREE OF

DOCTOR OF PHILOSOPHY

in

THE FACULTY OF GRADUATE STUDIES

(Electrical and Computer Engineering)

THE UNIVERSITY OF BRITISH COLUMBIA

February 2008

© Christopher Snow, 2008

Abstract

Ultra-Wideband (UWB) wireless communication systems employ large bandwidths and low transmitted power spectral densities, and are suitable for operation as underlay systems which reuse allocated spectrum. The subject of this dissertation is Multiband Orthogonal Frequency Division Multiplexing (MB-OFDM) UWB for high data-rate communication. We address four main questions: (1) What are the theoretical performance limits and practical system performance of MB-OFDM? (2) What extensions can be used to increase the system power efficiency and range? (3) Is it possible to estimate the system error rate without resorting to time-consuming simulations? and (4) What is the effect of interference from narrowband systems on MB-OFDM, and can this interference be mitigated?

As for questions 1 and 2, we investigate the MB-OFDM performance, and propose system enhancements consisting of advanced error correcting codes and OFDM bit-loading. Our methodology includes the development of information-theoretic performance measures and the comparison of these measures with performance results for MB-OFDM and our proposed extensions, which improve the power efficiency by over 6 dB at a data rate of 480 Mbps.

To address question 3, we develop novel analytical methods for bit error rate (BER) estimation for a general class of coded multicarrier systems (of which MB-OFDM is one example) operating over quasi-static fading channels. One method calculates system per-

formance for each channel realization. The other method assumes Rayleigh distributed subcarrier channel gains, and leads directly to the average BER. Both methods are also able to account for sum-of-tones narrowband interference.

As for question 4, we first present an exact analysis of the uncoded BER of MB-OFDM in the presence of interference from incumbent systems such as IEEE 802.16 ("WiMAX"). We also present a Gaussian approximation for WiMAX interference, and establish its accuracy through comparison with exact analysis and simulations. We then propose a two-stage interference mitigation technique for coded MB-OFDM, consisting of interference estimation during silent periods, followed by metric weighting during decoding, which provides substantial gains in performance in return for modest increases in complexity, and without requiring any modifications to the MB-OFDM transmitter.

Contents

List of Tables

List of Figures

List of Abbreviations

3GPP	3rd Generation Partnership Project
AR	Autoregressive
AWGN	Additive White Gaussian Noise
BER	Bit Error Rate
BICM	Bit Interleaved Coded Modulation
BPSK	Binary Phase Shift Keying
BWA	Broadband Wireless Access
CC	Convolutional Code
CDF	Cumulative Distribution Function
CDMA	Code Division Multiple Access
CE	Consumer Electronics
CIR	Channel Impulse Response
CL	Clustered Loading
CM	Channel Model
CP	Cyclic Prefix
CSI	Channel State Information
DAA	Detect and Avoid
DAB	Digital Audio Broadcasting
DCM	Dual Carrier Modulation

DFT	Discrete Fourier Transform
DS	Direct Sequence
DSL	Digital Subscriber Line
DS-UWB	Direct-Sequence Ultra-Wideband
DVB	Digital Video Broadcasting
ECMA	European Computer Manufacturers Association
EIRP	Effective Isotropic Radiated Power
FCC	Federal Communications Commission
FDS	Frequency-Domain Spreading
FFT	Fast Fourier Transform
GTF	Generalized Transfer Function
IEEE	Institute of Electrical and Electronic Engineers
IFFT	Inverse Fast Fourier Transform
i.i.d.	Independent and Identically Distributed
LDPC	Low Density Parity Check
LOS	Line of Sight
LSE	Least-Square Error
MB-OFDM	Multiband Orthogonal Frequency Division Multiplexing
MIMO	Multiple-Input Multiple-Output
MMSE	Minimum Mean Square Error
MRC	Maximum Ratio Combining
MTM	Multi-Taper Method
OFDM	Orthogonal Frequency Division Multiplexing
OLA	Overlap and Add
pdf	Probability Density Function

PEP	Pairwise Error Probability
PSD	Power Spectral Density
QAM	Quadrature Amplitude Modulation
QPSK	Quaternary Phase Shift Keying
RA	Repeat-Accumulate
RF	Radio Frequency
SC	Single Carrier
SIR	Signal to Interference Ratio
SNR	Signal to Noise Ratio
TC	Turbo Code
TDS	Time-Domain Spreading
TFC	Time-Frequency Code
TG	Task Group
USB	Universal Serial Bus
UWB	Ultra-Wideband
WLAN	Wireless Local Area Network
WMAN	Wireless Metropolitan Area Network
WPAN	Wireless Personal Area Network
ZP	Zero Padded

Notation

Bold upper case and lower case letters denote matrices and vectors, respectively. The remaining notation and operators used in this thesis are listed as follows:

$(\cdot)^*$	complex conjugate
$[\cdot]^T$	transpose
$[\cdot]^H$	Hermitian transpose
$\text{diag}(\boldsymbol{x})$	a matrix with the elements of vector $\boldsymbol{x}$ on the main diagonal
$\text{Re}\{\cdot\}$	the real part of a complex number
$\text{Im}\{\cdot\}$	the imaginary part of a complex number
$\mathbb{E}(\cdot)$	expectation
$\Pr\{\cdot\}$	the probability of some event
$\text{DFT}(\cdot)$	Discrete Fourier Transform
$Q(\cdot)$	Gaussian Q-function [1]
$\oplus$	the element-wise XOR operation
$\otimes$	the convolution operator
$\boldsymbol{I}_\eta$	identity matrix of dimension $\eta \times \eta$
$\mathbf{0}_\eta$	all-zero matrix of dimension $\eta \times \eta$
$\mathbf{0}_{\eta \times 1}$	all-zero column vector of length η
$\det(\cdot)$	matrix determinant
$\|\| \cdot \|\|$	the ℓ_2 vector norm

Acknowledgments

My deepest thanks to my co-advisors, Professor Lutz Lampe and Professor Robert Schober, for providing the perfect supervisory environment to support my graduate studies. Their energy, drive, and determination to succeed are infectious, and the positive attitude with which they have constantly supported my work has been invaluable. Their contributions are more than just technical — they have also fostered an environment of curiosity and learning, and this work reflects those ideals.

I would also like to thank the members of my doctoral committee, the University examiners, and the External examiner Professor Norman Beaulieu for the time and effort they have put forth and the feedback they have provided.

My thanks as well to the members of the Communications Theory Group, who have provided a very congenial workplace and many fruitful discussions, as well as invaluable feedback at many points over the years.

Without the constant support of my family, I would not be in the position I am in today. A heartfelt and deep thanks go to them.

Finally, to my wife Sarah: you have been my constant companion and the rock upon which my successes have been built. Truly, I could not have done it without you. Thank you, from the bottom of my heart.

The financial support of NSERC through its Canada Graduate Scholarship program and the support of the Canadian Wireless Telecommunications Association are gratefully acknowledged.

1 Introduction

The majority of wireless communication systems, past and present, have employed relatively narrow transmission bandwidths. This trend has been followed by most system designers for several reasons: (a) the radio spectrum is a scarce resource, and access to it is often limited to those users willing to buy spectrum allocations (for example, for mobile phone or television broadcasting systems); (b) the complexity of both transmitter and receiver designs tends to increase with increasing operating bandwidth; and (c) regulators, operators and system designers have often preferred to segment whatever bandwidth allocation they may have in order to support multiple users. While recent techniques such as Code Division Multiple Access (CDMA) have allowed multiple users to share spectrum, the majority of currently-deployed wireless systems still follow the narrowband approach.

1.1 Ultra-Wideband Communication Systems

Ultra-Wideband (UWB) communication systems are a paradigm shift in the wireless field. The traditional high-power, narrow bandwidth approach is abandoned, and instead the transmitted signal is spread over an extremely large bandwidth with very low power spectral density (PSD). There are several advantages to this approach, including:

1. fine time resolution of received signals, due to the wide bandwidth, which can be

used for accurate ranging measurements between UWB devices;

2. robustness to multipath fading due to the fine time resolution, which allows individual reflected signal components to be distinguished at the receiver;

3. the possibility of covert signal transmission as a result of the low PSD; and

4. traditional narrowband systems are not affected by UWB transmissions, again as a result of the low UWB PSD.

We are particularly interested in the fourth point, which allows UWB to be employed in spectral underlay systems for the reuse of previously-allocated spectrum [2]. This is particularly important due to the rapid deployment of many types of wireless communication systems and the resultant high demand for spectrum allocations.

Historically, the first UWB systems were employed in the radar field. However, several proposals were also made for wide bandwidth communication systems in the past [3]. These proposals were "impulse radio" systems, namely, carrierless systems employing baseband pulses with ultra-wide bandwidth. The theory of impulse radio systems is covered in a classic paper by Bennett and Ross [4].

During the mid-to-late 1990s, several researchers began (re-)investigating the potential of impulse radio systems, resulting in a number of publications which sparked a resurgence of interest in UWB [5–8]. This trend continued in the early 2000s [9, 10], to the point that a special issue of the IEEE Journal on Selected Areas in Communications was published in 2002 [11]. There are several excellent overview papers which cover the early development and evolution of impulse radio and other early UWB systems [12–14].

In 2002, the Federal Communications Commission (FCC) in the United States released a decision updating its Part 15 regulations, which govern unintentional and intentional radiation from electronic devices. The new ruling allows for several types of UWB transmissions:

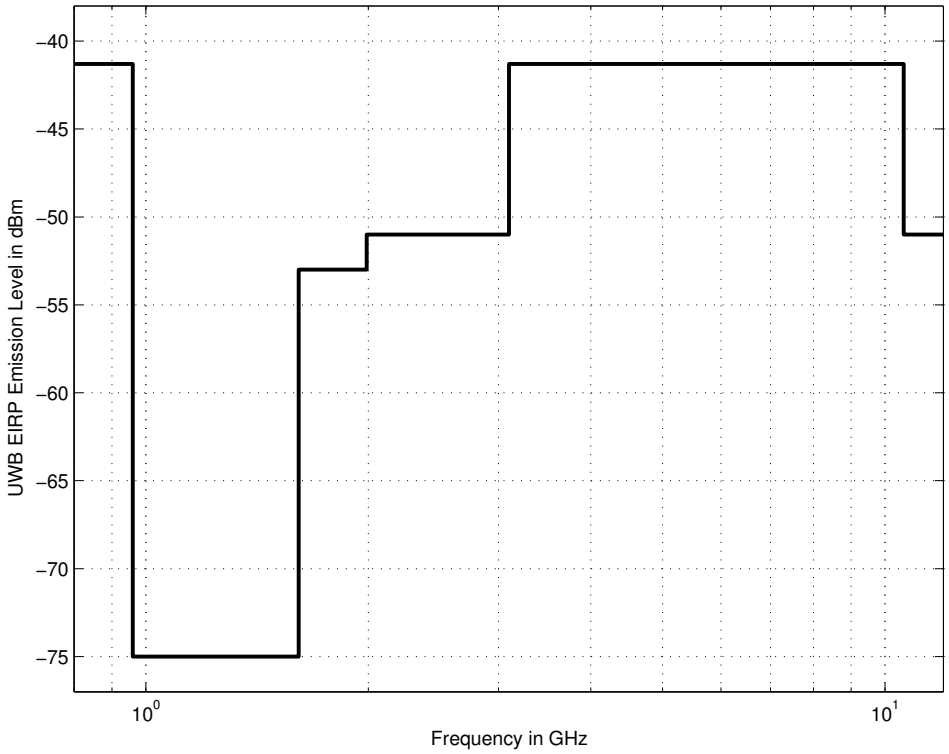

Figure 1.1: PSD mask required by the FCC [15].

1. imaging systems such as: ground penetrating radar, wall imaging systems, medical systems, and surveillance systems;

2. vehicular radar systems; and

3. communication and measurement systems.

For communication systems, the FCC allows intentionally-radiated UWB transmissions in the 3.1–10.6 GHz band [15]. The FCC defines a UWB device as "an intentional radiator that, at any point in time, has a fractional bandwidth equal to or greater than 0.20 or has a UWB bandwidth equal to or greater than 500 MHz, regardless of the fractional bandwidth", and limits the UWB Effective Isotropic Radiated Power (EIRP) for communications to -41.3 dBm/MHz in the 3.1–10.6 GHz band. Figure 1.1 summarizes the spectral mask set out in the 2002 ruling.

Before proceeding, some clarification of terms is in order. In the literature, especially that prior to the development of industry standards for UWB systems (to be discussed below), "UWB" is often used as a synonym of "impulse radio". In this thesis, we will use the term UWB in a more general sense, to denote any system which transmits with large bandwidth and low PSD, in compliance with the FCC regulations mentioned above. This expansive definition is more appropriate, due to the proliferation of UWB systems which adopt carrier-based transmissions, as will be discussed in the next section.

1.2 Standardization Efforts for UWB

The FCC decision to allow UWB transmission for wireless communication systems caused a flurry of activity on the part of both academics and industry practitioners. In response to the increased interest in UWB, the IEEE formed two groups to consider standardization of technology for both high data-rate and low-rate UWB systems.

Both standardization groups were formed under the auspices of the IEEE 802.15 Wireless Personal Area Networks (WPANs) group. In order to develop the new standards for UWB, the 802.15 group formed two task groups: TG3a (formed in 2002), to develop a new physical-layer specification for short-range, high data-rate wireless communications [16]; and TG4a (formed in 2003), responsible for a low data-rate communication and positioning standard [17]. The focus of this thesis is high-rate UWB — thus, we refer readers interested in low-rate UWB systems to [17] for more details regarding their standardization.

The process of standardization in IEEE task groups is as follows. First, a repeated down-selection voting procedure is used to remove the proposal with least support, resulting in (after a number of rounds of voting) one remaining proposal. During the down-selection procedure, a simple plurality voting system is used, meaning that the

final proposal is selected by a majority of the task group attendees. Once a proposal has been selected, it then requires a 75% majority vote in order to be confirmed as a draft standard.

Many contributors in TG3a brought forward proposals for UWB systems employing a variety of technologies. However, the task group quickly boiled the proposals down to two: Multiband Orthogonal Frequency Division Multiplexing (MB-OFDM) [18], and Direct-Sequence (DS) UWB (DS-UWB) [19]. Both of these proposals are extensions of well-explored narrowband transmission techniques: MB-OFDM employs OFDM technology, which has seen widespread use in systems such as Digital Subscriber Lines (DSL) [20], Digital Audio Broadcasting (DAB), Digital Video Broadcasting (DVB), IEEE 802.11a/g for wireless local area networks (WLANs) [21], and IEEE 802.16 for Broadband Wireless Access (BWA) [22]; DS-UWB employs a variation of the DS-CDMA technology which has been used in various systems, such as cdma2000 and UMTS for third-generation mobile phone systems. The proposals extend these base technologies to tailor them to the requirements of short-range high-rate communications, as well as to meet the FCC requirements for UWB emissions.

Because of the distribution of votes in support of the MB-OFDM and DS-UWB standard proposals, several consecutive meetings of TG3a were held in which one of the two proposals was down-selected, but was then unable to achieve the 75% majority required for confirmation. As a result, in 2006 TG3a abandoned the standardization efforts without agreeing on a high-rate UWB standard.

In the next section, we will focus on the development of MB-OFDM, post TG3a breakup.

1.3 The Fate of MB-OFDM

With the breakup of TG3a, support and development of the MB-OFDM proposal was undertaken by the WiMedia Alliance, a consortium of industry partners whose goal is to "promote and enable the rapid adoption and standardization of UWB worldwide for high-speed wireless, multimedia-capable personal-area connectivity in the PC [personal computer], CE [consumer electronics] and mobile market segments" [23]. With the support of WiMedia, the MB-OFDM physical layer proposal was standardized by ECMA (the European Computer Manufacturers Association) as ECMA-368 [24]. In addition, MB-OFDM has recently been adopted for use as the physical-layer technology for wireless Universal Serial Bus (USB) [25], and for the next generation of Bluetooth devices (Bluetooth 3.0).

1.4 MB-OFDM Literature Review

In this dissertation, we will address several relevant aspects of the MB-OFDM system in detail, as elaborated upon in Section 1.5. Before proceeding, we review below pertinent work that has been done on other aspects of MB-OFDM systems in the recent past.

Briefly, the MB-OFDM system is composed of OFDM-based multicarrier modulation [20, 26], combined with Bit-Interleaved Coded Modulation (BICM) for error correction [27], as well as frequency hopping to support multiple access. We will have more to say about the technical details of MB-OFDM in Chapter 2. In [28], the authors of the MB-OFDM standard provide a description of the system, and relate it to other communication techniques. This paper is a good starting point in a literature study of MB-OFDM developments. Comparisons of MB-OFDM and DS-UWB schemes can be found in [29].

There have been several papers attacking the problem of performance analysis of MB-OFDM systems [30–33]. Amongst them, [30] is notable in that it incorporates properties of realistic UWB channel models, and characterizes the MB-OFDM performance in terms of channel model parameters. Unfortunately, it does not consider the effect of error correction coding, which is part of the MB-OFDM standard. Error correction coding is considered in [31, 32], but not the same codes and interleaver structures as employed in MB-OFDM. In [33], the appropriate error correction codes are considered, but not suitable UWB channel models.

Several papers propose extensions in order to improve the MB-OFDM system performance. Techniques such as modulation diversity have been studied, either as an additional layer in the MB-OFDM system [34–36], or as a replacement for some portion of the system [37]. Fast-frequency hopping, which is a special case of modulation diversity, has also been considered [38]. Multiple-input multiple-output (MIMO) extensions for MB-OFDM have been considered [39–41], and have also been combined with differential modulation schemes [42]. The application of Low-Density Parity-Check (LDPC) codes is studied in [43, 44]. Subband and power allocation schemes are considered in [45, 46]. In addition, recent proposals have considered cooperative communication techniques in conjunction with MB-OFDM [47].

There are also several recent works which consider practical system effects in MB-OFDM. These effects include limited numerical precision [48], imperfect channel state information [49], timing jitter [50], imperfect synchronization [51, 52], the peak-to-average power ratio (PAPR) [53], estimation of signal arrival times [54], digital-to-analog conversion error [55], simple demodulator implementations [56, 57], interference from simultaneously-operating piconets [58], and the effects and suppression of impulsive noise [59].

The effects of narrowband interference on MB-OFDM systems have been considered.

In particular, interference resilient transmission schemes [60] and interference cancellation techniques [61] have been studied, and analysis of interference mitigation, including practical system effects such as quantization noise in analog-to-digital conversion, has been performed [62, 63].

Several authors have recently considered techniques for coexistence of MB-OFDM systems with incumbent narrowband devices [64], and transmission adaptation schemes for interference avoidance [65, 66]. There has also been recent work on the application of cognitive radio techniques [67] to MB-OFDM systems [68, 69].

The list above should not be construed as a complete list of publications relevant to MB-OFDM. However, it, along with further references to more specific prior work which will be given in the coming chapters, should serve as a good starting point for the interested reader to delve further into the literature in this area.

1.5 Thesis Contributions and Organization

This thesis considers four main areas of interest in relation to MB-OFDM:

1. the theoretical performance limits, and practical system performance;
2. extensions to increase the system performance and range;
3. the possibility of quickly and accurately estimating the system performance without time-consuming simulation techniques; and
4. the effect of interference from incumbent systems on MB-OFDM, and techniques to mitigate the interference effects.

We will address each of these questions in detail in the coming chapters.

In order to set the stage for the remainder of this thesis, in Chapter 2 we explain the pertinent features of the MB-OFDM transmission system. Readers already familiar with

MB-OFDM may wish to skip this chapter, or peruse it briefly for review, while those readers who have not previously encountered MB-OFDM should find sufficient detail in Chapter 2 to follow the remainder of the thesis.

Because of the nature of UWB communication, novel models are required in order to accurately capture the propagation effects of UWB channels. In Chapter 3, we first review the channel models developed for IEEE 802.15 TG3a, which we will consider in this thesis. Then, as a first step towards understanding the (potential) performance of MB-OFDM, we conduct a study of the channel model from a frequency-domain perspective suited for OFDM transmission, and quantify several parameters of interest.

In Chapter 4 we conduct a performance analysis of the MB-OFDM system, as well as propose and study system performance enhancements through the application of Turbo and Repeat-Accumulate (RA) codes, and OFDM bit-loading. Our methodology consists of (a) development and quantification of appropriate information-theoretic performance measures; (b) comparison of these measures with simulation results for the MB-OFDM standard as well as our proposed extensions; and (c) the consideration of the influence of practical, imperfect channel estimation. We find that MB-OFDM sufficiently exploits the frequency selectivity of the UWB channel, and that the system performs in the vicinity of the channel cutoff rate. Turbo codes and a reduced-complexity clustered bit-loading algorithm improve the system power efficiency by over 6 dB at a data rate of 480 Mbps, which translates into a 100% range improvement for MB-OFDM transmissions.

Chapter 5 is concerned with the development of techniques to estimate the performance of MB-OFDM systems without resorting to time-consuming simulations. We present two novel analytical methods for bit error rate (BER) estimation for coded MB-OFDM operating over frequency-selective quasi-static channels with non-ideal interleaving. In the first method, the approximate performance of the system is calculated for each realization of the channel, which is suitable for obtaining the outage BER perfor-

mance. The second method assumes Rayleigh distributed frequency-domain subcarrier channel gains and knowledge of their correlation matrix, and can be used to directly obtain the average BER performance. Both techniques are also able to account for narrowband interference (modeled as a sum of tone interferers), which is particularly relevant for MB-OFDM due to its spectral underlay behaviour and the resultant interference from incumbent narrowband devices. The methods developed in this chapter are applicable to a general class of convolutionally coded interleaved multicarrier systems, which includes IEEE 802.11a/g [21] and IEEE 802.16 [22] in addition to MB-OFDM.

In Chapter 6 we continue to address the issue of narrowband interference in MB-OFDM. Because the most likely interferer for first-generation MB-OFDM systems is the IEEE 802.16 WiMAX system operating in the 3.5 GHz band, we adopt the WiMAX signal model for this chapter. We perform an analysis of the performance of MB-OFDM in the presence of interference from WiMAX systems. We first present an exact analysis of the uncoded MB-OFDM BER, based on Laplace transform techniques. We also present a simple Gaussian approximation for the WiMAX interference, and establish its relative accuracy and usefulness by means of comparison with the exact analysis and simulations. Such a Gaussian approximation is especially useful for simplified performance analysis, as well as for the design of interference mitigation techniques. Motivated by the Gaussian approximation, we propose a simple two-stage interference mitigation technique for coded MB-OFDM transmissions, consisting of interference spectrum estimation during silent periods followed by appropriate bit metric weighting during Viterbi decoding. We compare parametric and non-parametric spectrum estimation techniques for various scenarios of interest. In the presence of WiMAX interference, the two-stage interference mitigation provides substantial gains in performance in return for modest increases in complexity and without requiring any modifications to the MB-OFDM transmitter or signal structure.

Finally, in Chapter 7 we provide some perspective on the results given in this dissertation, as well as several proposals for future work based on the results presented herein.

1.6 Related Publications

The following is a list of publications that are based on the research conducted for this thesis.

Journal Papers

1. C. Snow, L. Lampe, and R. Schober. Impact of WiMAX Interference on MB-OFDM UWB Systems: Analysis and Mitigation. Submitted to the *IEEE Transactions on Communications*.

2. C. Snow, L. Lampe, and R. Schober. Error Rate Analysis for Coded Multicarrier Systems over Quasi-Static Fading Channels. *IEEE Transactions on Communications*, 55(9):1736-1746, September 2007.

3. C. Snow, L. Lampe, and R. Schober. Performance Analysis and Enhancement of Multiband OFDM for UWB Communications. *IEEE Transactions on Wireless Communications*, 6(6):2182-2192, June 2007.

Book Chapters

4. C. Snow, L. Lampe, and R. Schober. Performance Analysis of MB-OFDM UWB Systems. To appear in *Emerging Wireless LANs, Wireless PANs, and Wireless MANs* (Yang Xiao and Yi Pan, eds.), Wiley, 2008.

Conference Papers

5. C. Snow, L. Lampe, and R. Schober. Interference Mitigation for Coded MB-OFDM UWB. In *Proc. IEEE Radio and Wireless Symposium*, Orlando, FL, USA, January 2008. **Invited paper.**

6. C. Snow, L. Lampe, and R. Schober. Analysis of the Impact of WiMAX-OFDM Interference on Multiband OFDM. In *Proc. IEEE International Conference on Ultra-WideBand*, Singapore, September 2007.

7. C. Snow, L. Lampe, and R. Schober. WiMAX Interference to MB-OFDM UWB Systems. In *Proc. IEEE Pacific Rim Conference on Communications, Computers and Signal Processing*, Victoria, August 2007.

8. C. Snow, L. Lampe, and R. Schober. Error Rate Analysis for Coded Multicarrier Systems over Quasi-Static Fading Channels. In *Proc. IEEE Global Telecommunications Conference*, San Francisco, November-December 2006.

9. C. Snow, L. Lampe, and R. Schober. Impact of Tone Interference on Multiband OFDM. In *Proc. IEEE International Conference on Ultra-Wideband*, Waltham MA, September 2006.

10. C. Snow, L. Lampe, and R. Schober. Enhancing Multiband OFDM Performance: Capacity-Approaching Codes and Bit Loading. In *Proc. IEEE International Conference on Ultra-Wideband*, Zurich, September 2005.

11. C. Snow, L. Lampe, and R. Schober. Performance Analysis of Multiband OFDM for UWB Communication. In *Proc. IEEE International Conference on Communications*, Seoul, May 2005.

2 MB-OFDM Transmission Model

In this chapter, the MB-OFDM transmission system is introduced. We describe the transmitter of the ECMA-368 MB-OFDM standard [18, 24]. The block diagram of the MB-OFDM transmitter described in this chapter is shown in Figure 2.1.

2.1 Channel Coding

Channel coding in MB-OFDM consists of classical BICM, i.e., a convolutional encoder followed by an interleaver and a memoryless mapper [27]. The base convolutional code is rate $R = 1/3$, constraint length 7, with generator polynomials $(133, 165, 171)_8$ (in octal).

In order to provide low-latency decoding and to reduce memory requirements during receiver processing, the convolutional code inputs are zero-terminated (driving the encoder back to the all-zero state, and allowing separate decoding of each block) every six OFDM symbols, which we will refer to as a "code block". Because of possible time/frequency spreading (cf. Section 2.5), the number of information bits per code block is a function of the data rate, and is summarized in Table 2.1.

Figure 2.1: Block diagram of the MB-OFDM transmission system. FDS: frequency-domain spreading; TDS: time-domain spreading; IFFT: inverse fast Fourier transform.

2.2 Puncturing

The convolutional code outputs are (optionally) punctured in order to support code rates R_c =1/3, 1/2, 5/8, and 3/4. The puncturing patterns for each punctured rate are given below, where each row represents the puncturing pattern for one of the three code outputs, and each column represents one time instant.

$$\text{Pat}_{1/2} = \begin{bmatrix} 1 \\ 0 \\ 1 \end{bmatrix} \qquad \text{Pat}_{5/8} = \begin{bmatrix} 1 & 0 & 1 & 0 & 1 \\ 1 & 0 & 1 & 0 & 1 \\ 0 & 1 & 0 & 1 & 0 \end{bmatrix} \qquad \text{Pat}_{3/4} = \begin{bmatrix} 1 & 0 & 0 \\ 1 & 0 & 0 \\ 0 & 1 & 1 \end{bmatrix}$$

2.3 Interleaving

After coding and puncturing, the bit stream is interleaved before being modulated. The interleaving process is a crucial component of BICM — it guarantees that bits which are "nearby" when output from the convolutional coder will be separated before being transmitted over the channel, which in turn means they will be subject to different fading gains, and thus the diversity present in the channel can be exploited during decoding at the receiver.

The MB-OFDM interleaver consists of three stages: symbol interleaving (between MB-OFDM symbols), tone interleaving (within each OFDM symbol), and intra-symbol cyclic shifts [18, 24]. A detailed description of the implementation of each interleaver can be found in the standard [24].

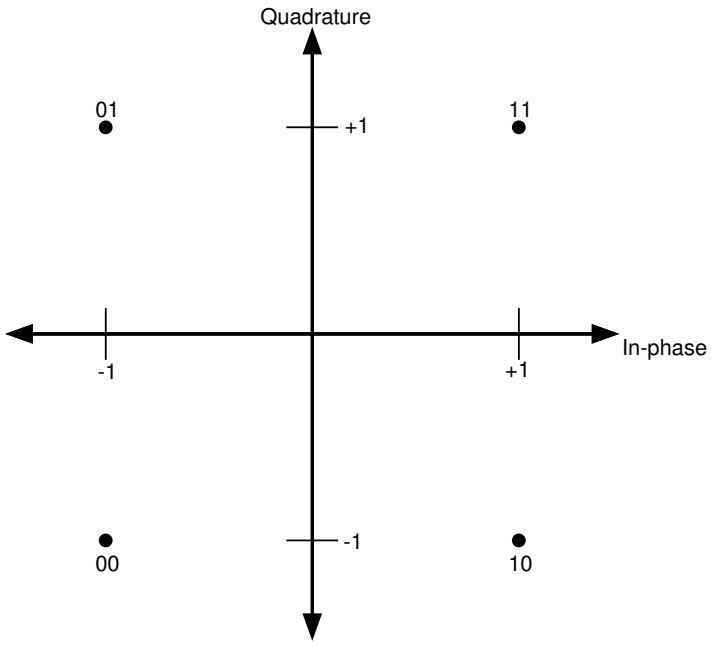

Figure 2.2: MB-OFDM QPSK constellation.

2.4 Modulation

2.4.1 Quaternary Phase Shift Keying

The interleaved bits are modulated using Quaternary Phase Shift Keying (QPSK), which maps two bits onto one of four signal points on the unit circle in the complex plane [1]. The QPSK constellation is shown in Figure 2.2.

2.4.2 Dual-Carrier Modulation

A late addition to the final ECMA-368 MB-OFDM standard was a new modulation scheme, referred to as Dual-Carrier Modulation (DCM). DCM is employed for the high data-rate modes (those with no time/frequency repetition, cf. Section 2.5), whereas in all previous versions of the standard QPSK modulation was employed for all data rates.

In DCM, the data stream is mapped to a four-dimensional constellation (two 2-

dimensional complex signal points) in groups of 4 bits at a time. This technique ensures that the information from each bit is represented in two different constellation points (which are then mapped to non-adjacent subcarriers in the OFDM symbol), which provides robustness against channel fading.

Because of the very late addition of DCM to the MB-OFDM standard relative to the progress of this work, we have not considered it in this dissertation. We will have more to say about DCM in Section 7.2.

2.5 Time/Frequency Spreading

In order to provide increased performance for low data rates, the MB-OFDM system includes support for frequency and time spreading, which provide repetition of the same data symbols over multiple subcarriers and/or OFDM symbols. Frequency-domain spreading (FDS) repeats the same data symbol over two different subcarriers in the same OFDM symbol, while time-domain spreading (TDS) repeats the entire OFDM symbol in two consecutive time slots. This spreading reduces the data rate by a factor of 2 (TDS alone) or 4 (TDS and FDS), which provides a performance gain for low data rate modes.

A total of eight data rates are supported in MB-OFDM, through a combination of code rates and use of TDS/FDS. The different rates and parameters are summarized in Table 2.1.

2.6 OFDM Symbol Framing

After the optional FDS/TDS discussed in Section 2.5, groups of 100 data symbols are formed into OFDM symbols, using $N = 128$ subcarriers. The non-data subcarriers are

Table 2.1: MB-OFDM data rates and number of bits per code block [24].

Data Rate (Mbps)	**Code Rate**	**FDS**	**TDS**	**Coded Bits per block**	**Info Bits per block**
53.3	1/3	Yes	Yes	300	100
80	1/2	Yes	Yes	300	150
106.7	1/3	No	Yes	600	200
160	1/2	No	Yes	600	300
200	5/8	No	Yes	600	375
320	1/2	No	No	1200	600
400	5/8	No	No	1200	750
480	3/4	No	No	1200	900

used for pilot tones, guard subcarriers, and other purposes [24].

2.7 Time-domain Processing

Each OFDM symbol is converted to the time domain using a 128-point Inverse Fast Fourier Transform (IFFT). A guard interval of time duration $T_g = 70.07$ ns (37 samples) is appended to each OFDM symbol before transmission. Each padded OFDM symbol thus consists of 165 samples, at a sampling rate of 528 Msamples/sec, for a total OFDM symbol duration of $T_s = 312.5$ ns.

2.7.1 Cyclic Prefix versus Zero Padding

Traditional OFDM systems employ a cyclic prefix (CP) guard interval, to protect against inter-OFDM-symbol interference as well as to convert the multipath fading channel into parallel single-tap fading channels affecting each subcarrier separately [1, 26]. The cyclic prefix is formed by padding the start of the OFDM symbol using a copy of some fraction of the samples from the end of the symbol. At the receiver, the prefix samples are discarded, and the remainder of the samples are converted back into the frequency domain using the Fast Fourier Transform (FFT).

The MB-OFDM system has adopted zero-padding (ZP) instead of a CP. In ZP, the end of each OFDM symbol is postfixed with a number of "0" guard samples. The two major benefits of zero padding are:

1. No energy is required to transmit the "0" samples (i.e., the transmitter can shut off during this time), as opposed to the CP technique which requires that the CP be transmitted, which consumes energy but does not convey any "useful" information.

2. The spectrum of an OFDM system with CP has regular frequency "spikes", due to the periodic nature of the CP-OFDM signal. On the other hand, the spectrum of the ZP signal does not have such spikes, which is a major benefit for UWB systems due to the PSD limits mandated by the FCC.

However, ZP-OFDM systems require that, at the receiver, the postfix samples be overlapped and added (OLA) with the data samples before the FFT, which introduces correlation between the samples [70].

Because the use of ZP introduces additional complexity in OFDM system analysis, we have assumed throughout this thesis that the MB-OFDM system employs a CP. While, at first glance, this may seem like an inappropriate assumption, it has been shown that ZP-OFDM and CP-OFDM have similar performance for most reasonable values of system parameters [70].[1] This has been verified by our own experience — we have found minimal differences in performance between ZP-based and CP-based MB-OFDM systems, which justifies our assumption.

[1]It should be noted that ZP-OFDM may offer better performance in the presence of various transmission impairments, such as carrier frequency offset [71].

2.7.2 Packetization

Transmission is organized in packets of varying payload lengths. Each packet header contains two pilot OFDM symbols (all tones are pilots) per frequency band, which are used at the receiver to perform channel estimation (see Section 4.3.1). Other details of packetization, which are unimportant for our purposes, can be found in the standard [24].

2.8 RF Processing and Frequency Hopping

The transmitted MB-OFDM symbol occupies a bandwidth of 528 MHz. In order to support multiple unsynchronized, simultaneously-operating MB-OFDM piconets, the standard employs a frequency-hopping technique in which the carrier frequency of MB-OFDM transmission is changed after each OFDM symbol. The standard specifies a total of 14 subbands organized into five band groups, as detailed in Table 2.2 [24].

Different piconets select different time-frequency codes (TFCs), which describe the order in which the subbands are hopped. For first-generation devices, band group 1 (three subbands) is used, which provides a total of six different TFCs, given in Table 2.3 [24].

2.9 Relevant System Parameters

The relevant parameters of the MB-OFDM system used in this thesis are summarized in Table 2.4.

Table 2.2: Subbands of the MB-OFDM standard [24].

Band Group	**Band**	**Lower Freq. (MHz)**	**Center Freq. (MHz)**	**Upper Freq. (MHz)**
1	1	3168	3432	3696
	2	3696	3960	4224
	3	4224	4488	4752
2	4	4752	5016	5280
	5	5280	5544	5808
	6	5808	6072	6336
3	7	6336	6600	6864
	8	6864	7128	7392
	9	7392	7656	7920
4	10	7920	8184	8448
	11	8448	8712	8976
	12	8976	9240	9504
5	13	9504	9768	10032
	14	10032	10296	10560

Table 2.3: Time-frequency codes for first-generation MB-OFDM devices [24].

TFC #	**Length 6 TFC Code**					
1	1	2	3	1	2	3
2	1	3	2	1	3	2
3	1	1	2	2	3	3
4	1	1	3	3	2	2
5	1	2	1	2	1	2
6	1	1	1	2	2	2

Table 2.4: Relevant MB-OFDM system parameters.

Parameter	**Meaning**	**Value**
N	number of subcarriers	128
W	bandwidth of transmission	528 MHz
T_s	OFDM symbol duration	312.5 ns
T_g	OFDM symbol guard duration	70.07 ns
T_d	OFDM symbol data duration	242.43 ns
Q	bandwidth per subcarrier	4.125 MHz

3 UWB Channel Models: Description and Relevant Aspects for OFDM-based Systems

Since our investigations rely on the UWB channel model developed under IEEE 802.15, specified in [72] and discussed in more detail in [73], in this chapter we analyze the channel model in the frequency domain and extract the relevant statistical parameters that affect the performance of OFDM-based transmission. In Section 3.1 we describe the general structure of the model and the relevant parameters. The mathematical model of the channel impulse response is given in Section 3.2. Finally, in Section 3.3 the distribution of the frequency-domain channel gains and the amount of diversity available in the wireless channel as a function of the signal bandwidth are examined.

3.1 UWB Channel Model: Description

For a meaningful performance analysis of MB-OFDM, we consider the channel model developed under IEEE 802.15 for UWB systems [72, 73]. The channel impulse response is a Saleh-Valenzuela model [74] modified to fit the properties of measured UWB channels. Multipath rays arrive in clusters with exponentially distributed cluster and ray inter-

Table 3.1: IEEE 802.15 TG3a channel model parameters [72].

Parameter	**Meaning**	**CM1**	**CM2**	**CM3**	**CM4**
Λ	cluster arrival rate (1/ns)	0.0233	0.4	0.0667	0.0667
λ	ray arrival rate (1/ns)	2.5	0.5	2.1	2.1
γ_c	cluster decay factor	7.1	5.5	14.0	24.0
γ_r	ray decay factor	4.2	6.7	7.9	12
σ_c	std. dev. of cluster fading (dB)	3.3941	3.3941	3.3941	3.3941
σ_r	std. dev. of ray fading (dB)	3.3941	3.3941	3.3941	3.3941
σ_G	std. dev. of shadowing (dB)	3	3	3	3
	Line of sight ?	yes	no	no	no

arrival times. Both clusters and rays have decay factors chosen to meet a given power decay profile. The ray amplitudes are modeled as lognormal random variables, and each cluster of rays also undergoes a lognormal fading. To provide a fair system comparison, the total multipath energy is normalized to unity. Finally, the entire impulse response undergoes an "outer" lognormal shadowing. The channel impulse response is assumed time invariant during the transmission period of several packets.

Four separate channel models (CM1-CM4) are available for UWB system modeling, each with arrival rates and decay factors chosen to match a different usage scenario. The four models are tuned to fit 0–4 m Line-of-Sight (LOS)[1], 0–4 m non-LOS, 4–10 m non-LOS, and an "extreme non-LOS multipath channel", respectively. The means and standard deviations of the outer lognormal shadowing are the same for all four models. The model parameters can be found in Table 3.1.

[1]We note that in the case of a "LOS" channel, the first-arriving (line-of-sight) path still undergoes the same fading as other paths in the impulse response.

3.2 UWB Channel Model: Mathematical Details

For the interested reader, in this section we provide a mathematical description of the 802.15 channel model [72, 73]. The channel impulse response is given by

$$h(t) = G \sum_{l=0}^{L} \sum_{k=0}^{K} \alpha_{k,l} \delta(t - T_l - \tau_{k,l}) \ ,$$

where G is a log-normal shadowing term, given by

$$G \sim 10^{\frac{N(0,\sigma_G^2)}{20}} \ ,$$

where $N(0, \sigma_G^2)$ denotes a Gaussian distribution with zero mean and variance σ_G^2. The multipath gain $\alpha_{k,l}$ of the kth multipath in the lth cluster is given by

$$\alpha_{k,l} = s_{k,l} \cdot m_{k,l} \ ,$$

where $s_{k,l}$ is either +1 or -1 with $\Pr\{+1\} = \Pr\{-1\} = 1/2$, and $m_{k,l}$ is given by

$$m_{k,l} = 10^{\frac{\mu_{k,l} + \psi_l + N(0,\sigma_r^2)}{20}}$$

with ψ_l (the cluster fade value) given by

$$\psi_l \sim N(0, \sigma_c^2)$$

and $\mu_{k,l}$ (the magnitude decay due to time) is given by

$$\mu_{k,l} = \frac{-10(T_l/\gamma_c + \tau_{k,l}/\gamma_r)}{\log(10)} - \frac{(\sigma_c^2 + \sigma_r^2)\log(10)}{20}$$

with T_l (the arrival time of the first ray in cluster l) and $\tau_{k,l}$ (the arrival time of the kth ray in cluster l, relative to the first ray of cluster l) being exponentially-distributed random variables, whose probability density functions are given by

$$p(T_l|T_{l-1}) = \Lambda \exp[-\Lambda(T_l - T_{l-1})]$$

$$p(\tau_{k,l}|\tau_{k-1,l}) = \lambda \exp[-\lambda(\tau_{k,l} - \tau_{k-1,l})] \; .$$

3.3 UWB Channel and Diversity Analysis for MB-OFDM

The UWB channel model described in Section 3.2 is a stochastic time-domain model. In this section, we consider a stochastic frequency-domain description, i.e., we include transmitter IFFT and receiver FFT into the channel definition and consider realizations of the frequency domain channel response $\boldsymbol{h} = [h_1 \dots h_N]^T$, where h_i denotes the frequency-domain channel gain of subcarrier i, which is the sample of the Fourier transform of $h(t)$ at frequency $(f_\mathrm{m} + iQ)$, where f_m is the MB-OFDM carrier frequency and Q is the bandwidth per subcarrier (given in Table 2.4). In doing so, we intend to

1. extract the channel parameters relevant for the performance of OFDM-based UWB systems;
2. examine whether MB-OFDM is adequate to exploit the channel characteristics;
3. quantify the impact of the different UWB channel types on system performance; and
4. possibly enable a classification of the UWB channel model into more standard channel models used in communication theory.

Assuming a sufficiently long guard interval, so that there is little or no inter-OFDM-symbol interference, the frequency-domain OFDM signal experiences a frequency non-selective fading channel with fading along the frequency axis [26]. Therefore, the outer lognormal shadowing term is irrelevant for the fading characteristics as it affects all tones equally. Hence, the lognormal shadowing term G is omitted in the following considerations. We obtain the corresponding *normalized* frequency-domain fading coefficient of subcarrier i as

$$h_i^{\mathrm{n}} = h_i / G \ . \tag{3.1}$$

3.3.1 Marginal Distribution

The first parameter of interest is the marginal distribution of h_i^{n}, i.e., the probability density function (pdf) $p(h_i^{\mathrm{n}})$.

First, we note that the frequency-domain coefficient h_i^{n} is a zero mean random variable since the time-domain multipath components are zero mean quantities. Furthermore, we have observed that h_i^{n} is, in good approximation, circularly symmetric complex Gaussian distributed, which is explained by the fact that h_i^{n} results from the superposition of many time-domain multipath components. Since these multipath components are mutually statistically independent, the variance of h_i^{n} is independent of the subcarrier index i.

Figure 3.1 shows measurements of the pdfs $p(|h_i^{\mathrm{n}}|)$ of the magnitude frequency-domain gain $|h_i^{\mathrm{n}}|$ for the different channel models CM1-CM4, obtained from 10000 independent realizations of each channel model. As can be seen, the experimental distributions agree well with the exact Rayleigh distribution of equal variance, which is in accordance with the statements above. We note that similar conclusions regarding the

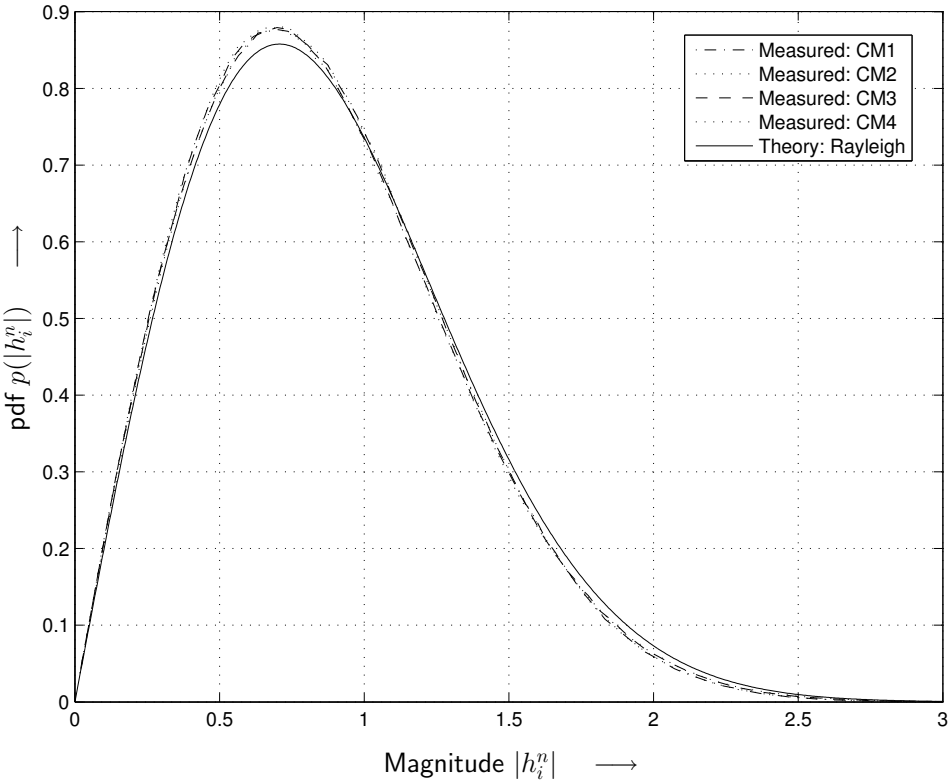

Figure 3.1: Distributions of normalized channel magnitude $|h_i^{\mathrm{n}}|$ for channel types CM1-CM4. For comparison: Rayleigh distribution with same variance.

frequency-domain gains were obtained independently in [31].[2]

Figure 3.2 shows measurements of the cumulative distribution functions (CDFs) of the magnitude frequency-domain gain $|h_i^{\mathrm{n}}|$ for the different channel models CM1-CM4, obtained from 10000 independent realizations of each channel model. The exact Rayleigh CDF of equal variance again provides an excellent match with the UWB channel CDFs.

3.3.2 Correlation

The findings in the previous section indicate that the OFDM signal effectively experiences a (classical) frequency non-selective Rayleigh fading channel (along the OFDM

[2]We note that our work was first submitted as a conference paper (presented at ICC 2005), before [31] appeared.

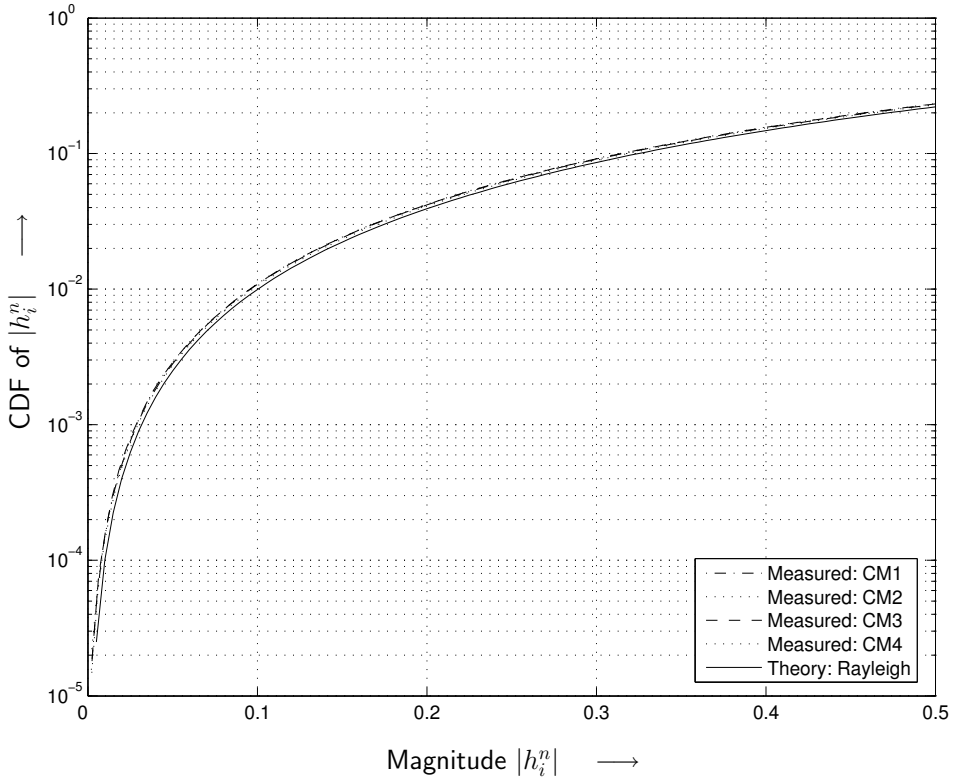

Figure 3.2: Cumulative distribution functions of normalized channel magnitude $|h_i^{\mathrm{n}}|$ for channel types CM1-CM4. For comparison: Rayleigh CDF with same variance.

subcarriers). Therefore, knowledge of the second-order channel statistics, i.e., the correlation between different fading coefficients h_i^{n} and h_j^{n}, $i \neq j$, is important for the design and assessment of diversity techniques such as coding, interleaving, and frequency hopping, which are used in the MB-OFDM system. Since coding is performed over all bands, we consider all 3 bands jointly. For the remainder of this thesis, we consider only channels CM1-CM3, where the cyclic prefix is longer than the delay spread of the channel impulse response (CIR).[3]

As an appropriate figure of merit we examine the ordered eigenvalues of the $3{\cdot}N \times 3{\cdot}N$ correlation matrix $\boldsymbol{R}_{\boldsymbol{h}^{\mathrm{n}}\boldsymbol{h}^{\mathrm{n}}}$ of $\boldsymbol{h}^{\mathrm{n}} = [h_1^{\mathrm{n}} \ldots h_{3\cdot N}^{\mathrm{n}}]^T$. Figure 3.3 shows the first 40 ordered

[3]However, we note that error-rate simulations have verified that CM4 performance is very similar to that of CM3.

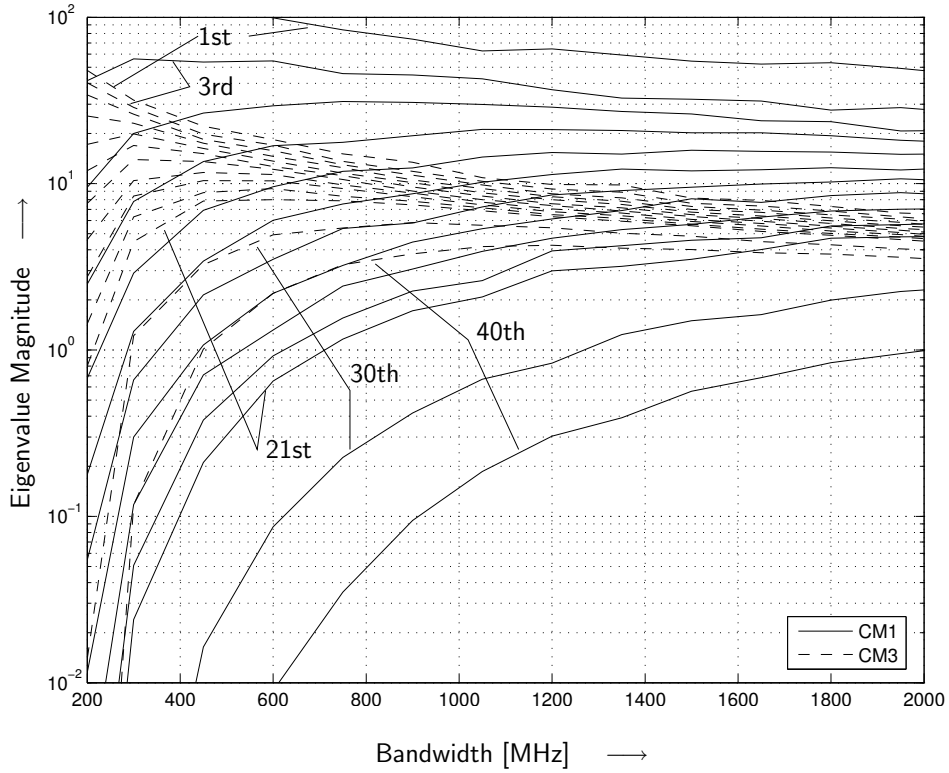

Figure 3.3: First 40 ordered eigenvalues of the correlation matrix $\boldsymbol{R}_{\boldsymbol{h}^{\mathrm{n}}\boldsymbol{h}^{\mathrm{n}}}$ (every second from 1st to 21st, and the 30th and 40th).

eigenvalues (every second from 1st to 21st, and the 30th and 40th) of the measured $\boldsymbol{R}_{\boldsymbol{h}^{\mathrm{n}}\boldsymbol{h}^{\mathrm{n}}}$, which has been obtained by averaging over 1000 channel realizations, as a function of the total employed signal bandwidth. We only show representative results for channel models CM1 (few multipath components) and CM3 (many multipath components). The respective curve for model CM2 lies in between those for CM1 and CM3.

From Figure 3.3 we infer the following conclusions:

1. By increasing the bandwidth of the OFDM signal, the diversity order of the equivalent frequency-domain channel, i.e., the number of the significant non-zero eigenvalues of $\boldsymbol{R}_{\boldsymbol{h}^{\mathrm{n}}\boldsymbol{h}^{\mathrm{n}}}$, is improved, since, generally, more time-domain multipath components are resolved. However, a 1500 MHz total bandwidth provides already ≥ 40 (CM3) and ≥ 30 (CM1) strong diversity branches. This indicates that the

528 MHz bandwidth and 3-band frequency hopping of MB-OFDM is a favorable compromise between complexity and available diversity.

2. Since the system, comprising the convolutional code (see Chapter 2) with free distance ≤ 15 (depending on the puncturing) and spreading with spreading factor 1, 2, and 4, can at best exploit diversities of order 15, 30 and 60, respectively, bandwidths of more than 500 MHz per band would only be beneficial for the lowest data-rate modes, and then only for very low error rates. Similar considerations apply to concatenated codes (e.g., Turbo and RA codes as considered in Chapter 4), which do not exceed convolutional codes with spreading in terms of free distance.

3. Though CM3 provides higher diversity order than CM1, the latter appears advantageous for high data-rate modes with code puncturing due to its larger first ordered eigenvalues.

In summary, we conclude that, given a particular realization of the lognormal shadowing term, the equivalent frequency-domain channel $\boldsymbol{h}$ is well approximated by a Rayleigh fading channel with relatively high "fading rate", which increases from CM1 to CM3.

4 Performance of MB-OFDM and Extensions

4.1 Introduction

The objective of this chapter is to study the suitability and to analyze the (potential) performance of MB-OFDM for UWB transmission. Furthermore, we propose system performance enhancements by applying capacity-approaching Turbo and RA codes and by using OFDM bit-loading. These specific techniques were chosen because of their potential for improved system performance without requiring substantial changes to other portions of the MB-OFDM system, nor requiring major increases in complexity.

As appropriate performance measures for coded communication systems, we discuss the capacity and cutoff rate limits of BICM-OFDM systems for UWB channels. In this context, since one limiting factor of performance in practical and especially in wideband BICM-OFDM systems is the availability of high-quality channel state estimates, the effect of imperfect channel state information (CSI) at the receiver is specifically addressed. Furthermore, the information-theoretic performance limits are compared with simulated BER results for MB-OFDM and the extensions introduced herein.

As discussed in Section 1.4, there are several prior works on MB-OFDM system extensions. As an extension to the standard, simplified LDPC codes are considered in

[43] in order to improve the power efficiency of the MB-OFDM system for a subset of the data rates. The authors of [45] consider the application of a clustered power allocation scheme to MB-OFDM. However, this scheme attempts to maximize throughput and therefore does not provide fixed data rates compatible with the MB-OFDM standard. In [40] the authors present a space-time-frequency coding scheme for MB-OFDM. A subband and power allocation strategy for a multiuser MB-OFDM system is given in [46], but each user in the system uses a fixed modulation (i.e., no per-user bit allocation is performed), and subcarrier power allocation in MB-OFDM is problematic due to the spectrum limitations imposed by the FCC. We note that none of these previous works provide comparisons with relevant information-theoretic limits.

The remainder of this chapter is organized as follows. Section 4.2 describes the MB-OFDM receiver and the performance enhancements we propose. In Section 4.3, we describe the MB-OFDM receiver processing. Section 4.4 presents the capacity and cutoff rate analysis and numerical results. Simulation results for the MB-OFDM system and the proposed extensions are presented and compared with the theoretical benchmark measures in Section 4.5, and conclusions are given in Section 4.6.

4.2 MB-OFDM Transmission Extensions

In this section we describe our proposed extensions to channel coding and to modulation.

4.2.1 Channel Coding: Turbo Codes

We propose the use of Turbo codes [75] in order to improve the system power efficiency and more closely approach the channel capacity. We examined generator polynomials of constraint length 3, 4 and 5 as well as various interleavers (including s-rand [76] and dithered relative prime [77] designs). Due to their excellent performance for the code

lengths considered as well as reasonable interleaver memory storage requirements, we decided to adopt the generator polynomials and interleaver design developed by the 3rd Generation Partnership Project (3GPP) [78]. For low data rates, the time/frequency spreading technique of the MB-OFDM standard is retained. We would like to maintain compatibility with the MB-OFDM channel interleaver by having each coded block fit into one channel interleaver frame, as is done with the convolutional codes used in the standard (cf. Section 2.3).[1] However, to maintain compatibility at the lowest data rates would require a Turbo code interleaver length of only 150 or 300 bits. Due to the poor distance properties and resultant performance degradation associated with short-length Turbo codes, at low data rates we consider both MB-OFDM-compliant block lengths and longer blocks of 600 input bits (the same length as used without spreading).

4.2.2 Channel Coding: RA Codes

The limited length of the MB-OFDM channel interleaver motivates the consideration of serially-concatenated codes, where the interleaver is positioned between the constituent encoders and thus has a longer length. We consider nonsystematic regular RA codes [79] due to their simplicity and good performance for the required code lengths. The time/frequency spreading mechanism described above is discarded, and low-rate RA codes ($R = 1/4$ or $1/8$) are used. The interleaver between the repeater and accumulator is randomly generated (no attempt is made to optimize its performance).

[1] Note that keeping the block lengths short also reduces the memory requirements and decoding delay at the receiver.

4.2.3 Modulation: Bit-Loading

The UWB channel (see Chapter 3) is considered time-invariant for the duration of many packet transmissions. For that reason, it is feasible to consider bit-loading algorithms to assign unequal numbers of bits to each OFDM subcarrier [20]. Channel state information is obtained at the transmitter, either by (a) exploiting channel reciprocity (if the same frequency band is used in the uplink and downlink, as in the standard), or (b) some form of feedback (which may be required even if the same frequency band is used, since reciprocity may not apply due to different interference scenarios for transmitter and receiver). We consider loading for higher data rates (without time or frequency spreading) using two different OFDM bit-loading schemes. We selected the algorithm of Piazzo [80] (which loads according to the uncoded BER) due to its low computational complexity, and the algorithm of Chow, Cioffi and Bingham (CCB) [81] because it loads according to the information-theoretic capacity criterion, as well as for its moderate computational complexity.

The data rates and OFDM symbol structure of MB-OFDM are maintained by loading each OFDM symbol with 200 bits. Each tone carries from 0 to 6 bits using QAM signal constellations with Gray or quasi-Gray labeling (note that 6 bit/symbol corresponds to 64-QAM, which is a reasonable upper limit for modulation on a wireless channel). Due to the FCC restrictions on the transmitted PSD, power loading is not used (all tones carry the same power). The target uncoded BER for the Piazzo algorithm is chosen as 10^{-5} (cf. [80] for details), but we found that performance is quite insensitive to this parameter. For the CCB algorithm, the signal-to-noise ratio (SNR) gap parameter Γ is either 6 dB (when convolutional codes are used) or 3 dB (for Turbo codes). When the algorithm is unable to determine a suitable loading an all-QPSK loading is used, cf. [81] for details.

4.2.4 Modulation: Clustered Bit-Loading

One potential feedback-based method of bit-loading is for the receiver to determine the appropriate modulation for each tone and feed the loading information back to the transmitter. To lower the feedback transmission requirements and significantly reduce the loading algorithm's computational complexity, we propose a clustered loading scheme where clusters are formed by considering groups of D adjacent tones. As we found the CCB algorithm superior to the Piazzo algorithm in terms of achievable power efficiency (see Sections 4.4.4 and 4.5.2), we modify the CCB algorithm for clustered loading, as described below.

The original CCB algorithm begins by computing an optimal loading $b(i)$ for each subcarrier i, given by [81, Eq. (1)]

$$b(i) = \log_2 \left(1 + SNR(i) \cdot 10^{-\left(\frac{\Gamma + \gamma_{margin}}{10}\right)} \right) , \tag{4.1}$$

where $SNR(i)$ is the signal-to-noise ratio of the ith tone and γ_{margin} is the system performance margin in dB (iteratively calculated by the CCB algorithm). We replace this equation with

$$b(k) = \frac{1}{D} \sum_{i=1}^{D} \log_2 \left(1 + SNR(k,i) \cdot 10^{-\left(\frac{\Gamma + \gamma_{margin}}{10}\right)} \right) , \tag{4.2}$$

where $b(k)$ is the loading for the kth cluster and $SNR(k,i)$ is the signal-to-noise ratio of the ith tone in the kth cluster. Using the modified algorithm to load $200/D$ bits on $100/D$ clusters provides the final integer-valued loadings $\hat{b}(k)$ for each cluster. Finally, all tones in cluster k are assigned $\hat{b}(k)$ bits (i.e. the loading inside each cluster is constant). This modification causes the CCB algorithm to load according to the mean capacity of all tones in a cluster.

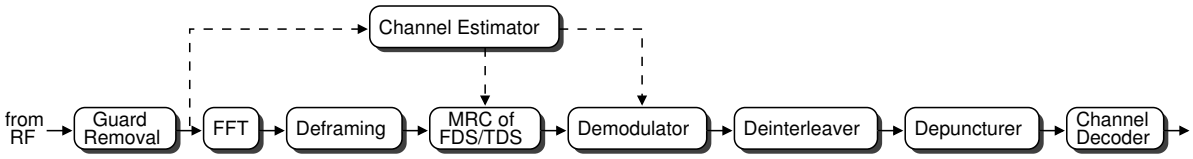

Figure 4.1: Block diagram of the MB-OFDM receiver structure.

4.3 Receiver Processing

The block diagram of the receiver considered in this chapter is depicted in Fig 4.1. We assume perfect timing and frequency synchronization. As mentioned in Section 3.3.2, we consider only channels CM1-CM3, where the cyclic prefix is longer than the delay spread of the CIR.

The frequency-domain transmitted signal for the kth MB-OFDM symbol is given by

$$\boldsymbol{X}[k] = \mathrm{diag}\left([x_1[k]\ x_2[k]\ \ldots\ x_N[k]]\right)\ , \tag{4.3}$$

where $x_i[k]$ is the transmitted symbol on frequency tone $i \in 1 \ldots N$ of the kth OFDM symbol. The frequency domain samples of the channel transfer function (assumed constant over the considered time span — see Section 3.1) are given by

$$\boldsymbol{h} = [h_1\ h_2\ \ldots\ h_N]^T\ , \tag{4.4}$$

and the additive white Gaussian noise (AWGN) samples are given by

$$\boldsymbol{n}[k] = [n_1[k]\ n_2[k]\ \ldots\ n_N[k]]^T\ . \tag{4.5}$$

Thus, after FFT we see an equivalent N dimensional frequency non-selective vector channel, expressed as [20]

$$\boldsymbol{y}[k] = \boldsymbol{X}[k]\boldsymbol{h} + \boldsymbol{n}[k]\ . \tag{4.6}$$

The channel estimation, diversity combining, demapping, and decoding are described in the following.

4.3.1 Channel Estimation

We implement a least-squares error (LSE) channel estimator for the time-domain CIR using the P pilot OFDM symbols for each frequency band transmitted in the packet header. For a more general treatment, we let P be a design parameter, but we note that $P = 2$ is specified in the standard [24]. The responses in different frequency bands can be estimated separately, since pilot symbols are transmitted for each band. The LSE estimator is chosen instead of minimum-mean-square error (MMSE) estimation because it does not require assumptions regarding the statistical structure of the channel correlation. Furthermore, it has been shown that LSE and MMSE estimation perform almost equally well for cases of practical interest [82].

The LSE estimator exploits the fact that the CIR has a maximum of $L \leq N$ taps. Starting from (4.6), the frequency-domain vector channel estimate can be represented as (cf. e.g., [82])

$$\hat{\boldsymbol{h}} = \boldsymbol{h} + \boldsymbol{e} \,, \tag{4.7}$$

where the channel estimation error vector

$$\boldsymbol{e} = \boldsymbol{F}_{N\times L}\boldsymbol{F}_{N\times L}^{H} \cdot \frac{1}{P}\sum_{k=1}^{P} \boldsymbol{X}^{H}[k]\boldsymbol{n}[k] \tag{4.8}$$

is independent of $\boldsymbol{h}$ and zero-mean Gaussian distributed with correlation matrix

$$\begin{aligned} \boldsymbol{R}_{\boldsymbol{ee}} &= \boldsymbol{F}_{N\times L}\boldsymbol{F}_{N\times L}^{H} \left(\frac{\sigma_n^2}{P^2} \sum_{k=1}^{P} \boldsymbol{X}^{H}[k]\boldsymbol{X}[k] \right) \boldsymbol{F}_{N\times L}\boldsymbol{F}_{N\times L}^{H} \\ &= \frac{\sigma_n^2}{P}\boldsymbol{F}_{N\times L}\boldsymbol{F}_{N\times L}^{H} \,. \end{aligned} \tag{4.9}$$

In (4.8) and (4.9), $\boldsymbol{F}_{N\times L}$ denotes the normalized $N \times L$ FFT matrix with elements $\mathrm{e}^{-\mathrm{j}\mu\nu 2\pi/N}/\sqrt{N}$ in row μ and column ν, and σ_n^2 is the AWGN variance. For the last step in (4.9) we assumed the use of constant modulus pilot symbols $|x_i[k]| = 1$ as in the MB-OFDM standard [24] (we note that in cases where bit-loading is applied, constant modulus symbols will still be used for the pilots in the packet header). We observe from (4.7) and (4.9) that the LSE channel estimate is impaired by correlated Gaussian noise with variance

$$\sigma_e^2 = \frac{L}{NP}\sigma_n^2 = \eta\sigma_n^2 \,. \tag{4.10}$$

In order to keep complexity low, we do not attempt to exploit the correlation, and we further assume that because of interleaving the effect of correlation is negligible. We will refer to parameter

$$\eta = \frac{L}{NP} \tag{4.11}$$

when evaluating the performance of MB-OFDM with imperfect CSI in Sections 4.4.3 and 4.5.1. In the remainder of this chapter, we assume a maximum impulse response length of $L = 32$, valid for CM1-CM3 (cf. Chapter 3).

4.3.2 Diversity Combining, Demapping, and Decoding

Maximum-ratio combining (MRC) [1] in the case of time and/or frequency spreading (see Chapter 2) and demapping in the standard BICM fashion [27] are performed based on the channel estimator output $\hat{\boldsymbol{h}}$. The resulting "soft" bit metrics are deinterleaved and depunctured.

The standard convolutionally coded schemes use a soft-input Viterbi decoder to restore the original bit stream, requiring a decoding complexity of 64 trellis states searched per information bit. Turbo-coded schemes are decoded with 10 iterations of a conventional Turbo decoder using the log-domain BCJR algorithm [83], with a complexity of

roughly 10·2·2·8 = 320 trellis states searched per information bit (i.e., 10 iterations of two 8-state component codes, and assuming that the BCJR algorithm is roughly twice as complex as the Viterbi algorithm due to the forward-backward recursion). RA decoding is performed by a turbo-like iterative decoder, using a maximum of 60 iterations and an early-exit criterion which, at relevant values of SNR, reduces the average number of decoder iterations to less than ten [84]. We note that the per-iteration decoding complexity of the RA code is less than that of the Turbo code (since only a 2-state accumulator and a repetition code are used), making the total RA decoder complexity slightly more than the convolutional code but less than the Turbo code. The increased decoder complexities of the Turbo and RA codes, compared to the convolutional code, are reasonable considering the performance gains they provide (see Section 4.5).

4.4 Capacity and Cutoff Rate Analysis

The purpose of this section is to quantify potential data rates and power efficiencies of OFDM-based UWB transmission. Of particular interest here are:

1. the channel capacity and cutoff rate,[2] which are widely accepted performance measures for coded transmission using powerful concatenated codes and convolutional codes, respectively;

2. the influence of the particular channel model (CM1-CM3); and

3. the effect of imperfect channel estimation on these measures.

Since coding and interleaving are limited to single realizations of lognormal shadowing, we focus on the notion of *outage probability*, i.e., the probability that the instan-

[2]It is important to note that the capacity and cutoff rate discussed here are *constellation-constrained*, i.e., they are calculated assuming a given input constellation with uniform input probabilities.

taneous capacity and cutoff rate for a given channel realization $\boldsymbol{h}$ fall below a certain threshold. These theoretical performance measures will be compared with simulation results for the MB-OFDM system in Section 4.5.

In Section 4.4.1, we review the instantaneous capacity and cutoff rate expressions for BICM-OFDM, and extend these expressions to include systems with bit-loading. The required conditional pdf of the channel output is given in Section 4.4.2. Sections 4.4.3 and 4.4.4 contain numerical results for systems without and with loading, respectively.

4.4.1 Capacity and Cutoff Rate Expressions

Without Bit-Loading

The instantaneous capacity in bits per complex dimension of an N tone BICM-OFDM system in a frequency-selective quasi-static channel is given in [85] (by extending the results of [27]) as

$$C(\boldsymbol{h}) = m - \frac{1}{N}\sum_{\ell=1}^{m}\sum_{i=1}^{N}\mathbb{E}_{b,y_i}\left\{\log_2\left(\frac{\sum_{x_i\in\mathcal{X}} p(y_i|\hat{h}_i,x_i)}{\sum_{x_i\in\mathcal{X}_b^\ell} p(y_i|\hat{h}_i,x_i)}\right)\right\}. \tag{4.12}$$

In (4.12), m is the number of bits per symbol, $\mathcal{X}$ is the signal constellation and $\mathcal{X}_b^\ell$ is the set of all constellation points $x \in \mathcal{X}$ whose label has the value $b \in \{0,1\}$ in position ℓ, and $p(y_i|\hat{h}_i, x_i)$ is the pdf of the channel output y_i for given input x_i and channel estimate $\hat{h}_i$. For MB-OFDM, $\mathcal{X}$ is the QPSK signal constellation and $m = 2$ is valid.

Similarly, we can express the instantaneous cutoff rate in bits per complex dimension as (cf. e.g., [27, 85])

$$R_0(\boldsymbol{h}) = m(1 - \log_2(B(\boldsymbol{h}) + 1)) \tag{4.13}$$

with the instantaneous Bhattacharya parameter ($\bar{b}$ denotes the complement of b)

$$B(\boldsymbol{h}) = \frac{1}{mN} \sum_{\ell=1}^{m} \sum_{i=1}^{N} \mathbb{E}_{b,y_i} \left\{ \sqrt{\frac{\sum\limits_{x_i \in \mathcal{X}_{\bar{b}}^{\ell}} p(y_i|\hat{h}_i, x_i)}{\sum\limits_{x_i \in \mathcal{X}_{b}^{\ell}} p(y_i|\hat{h}_i, x_i)}} \right\}. \tag{4.14}$$

With Bit-Loading

The instantaneous capacity in bits per complex dimension of an N tone BICM-OFDM system using loading can be found by extending (4.12) and (4.13) (following the methodology of [27, 85]) as

$$C(\boldsymbol{h}) = \bar{m} - \frac{1}{N} \sum_{i=1}^{N} \sum_{\ell=1}^{m_i} \mathbb{E}_{b,y_i} \left\{ \log_2 \left(\frac{\sum\limits_{x_i \in \mathcal{X}_i} p(y_i|\hat{h}_i, x_i)}{\sum\limits_{x_i \in \mathcal{X}_{i,b}^{\ell}} p(y_i|\hat{h}_i, x_i)} \right) \right\}. \tag{4.15}$$

In (4.15), $\bar{m}$ is the average number of bits/symbol ($\bar{m} = 2$ throughout this chapter), m_i and $\mathcal{X}_i$ are the number of bits per symbol and the signal constellation for the ith tone, respectively, and $\mathcal{X}_{i,b}^{\ell}$ is the set of all constellation points $x \in \mathcal{X}_i$ whose label has the value $b \in \{0, 1\}$ in position ℓ.

Similarly, we can express the instantaneous cutoff rate for bit-loading systems in bits per complex dimension as

$$R_0(\boldsymbol{h}) = \bar{m}(1 - \log_2(B(\boldsymbol{h}) + 1)) \tag{4.16}$$

with the instantaneous Bhattacharya parameter

$$B(\boldsymbol{h}) = \frac{1}{N\bar{m}} \sum_{i=1}^{N} \sum_{\ell=1}^{m_i} \mathbb{E}_{b,y_i} \left\{ \sqrt{\frac{\sum\limits_{x_i \in \mathcal{X}_{i,\bar{b}}^{\ell}} p(y_i|\hat{h}_i, x_i)}{\sum\limits_{x_i \in \mathcal{X}_{i,b}^{\ell}} p(y_i|\hat{h}_i, x_i)}} \right\}. \tag{4.17}$$

4.4.2 Conditional PDF

In order to calculate capacity and cutoff rate, we require the conditional pdf $p(y_i|\hat{h}_i, x_i)$. In the case of perfect CSI we have $\hat{h}_i = h_i$, and $p(y_i|\hat{h}_i, x_i)$ is a Gaussian pdf with mean $h_i x_i$ and variance σ_n^2.

We now obtain $p(y_i|\hat{h}_i, x_i)$ for the more realistic case of imperfect CSI assuming the application of LSE channel estimation as described in Section 4.3. According to the results of Section 3.3.1 and since channel estimation is performed for one realization G of the lognormal shadowing term, we further assume zero-mean circularly symmetric Gaussian distributed channel coefficients h_i with variance $\sigma_h^2 = G^2$ (see (3.1)). This means that $\hat{h}_i$ is also zero-mean Gaussian distributed with variance $\sigma_{\hat{h}}^2 = \sigma_h^2 + \sigma_e^2$ (see (4.7) and (4.10)). Let μ be the correlation between h_i and $\hat{h}_i$,

$$\mu = \frac{\mathbb{E}_{h_i,\hat{h}_i}\{h_i \hat{h}_i^*\}}{\sigma_h \sigma_{\hat{h}}} = \sqrt{\frac{\sigma_h^2}{\sigma_e^2 + \sigma_h^2}} = \sqrt{\frac{\gamma}{\gamma + \eta}}\,, \tag{4.18}$$

where η is defined in (4.10), and $\gamma = \sigma_h^2/\sigma_n^2$ is the SNR. Then, we can arrive via algebraic manipulations at (cf. e.g., [86])

$$p(y_i|\hat{h}_i, x_i) = \frac{1}{\pi\sigma_n^2(\eta\mu^2 + 1)} \exp\left(-\frac{|y_i - x_i\hat{h}_i\mu^2|^2}{\sigma_n^2(\eta\mu^2 + 1)}\right)\,. \tag{4.19}$$

The Gaussian density of (4.19) implies that the system with imperfect CSI can be seen as a system with perfect CSI at an equivalent SNR of

$$\gamma_e = \frac{\mathbb{E}_{\hat{h}_i}\{|\hat{h}_i|^2\}\mu^4}{\sigma_n^2(\eta\mu^2 + 1)} = \frac{\gamma}{\eta\left(1 + \frac{1}{\gamma}\right) + 1}\,. \tag{4.20}$$

We note that in the high SNR regime the loss due to estimation error reaches a constant value of $1/(\eta + 1)$.

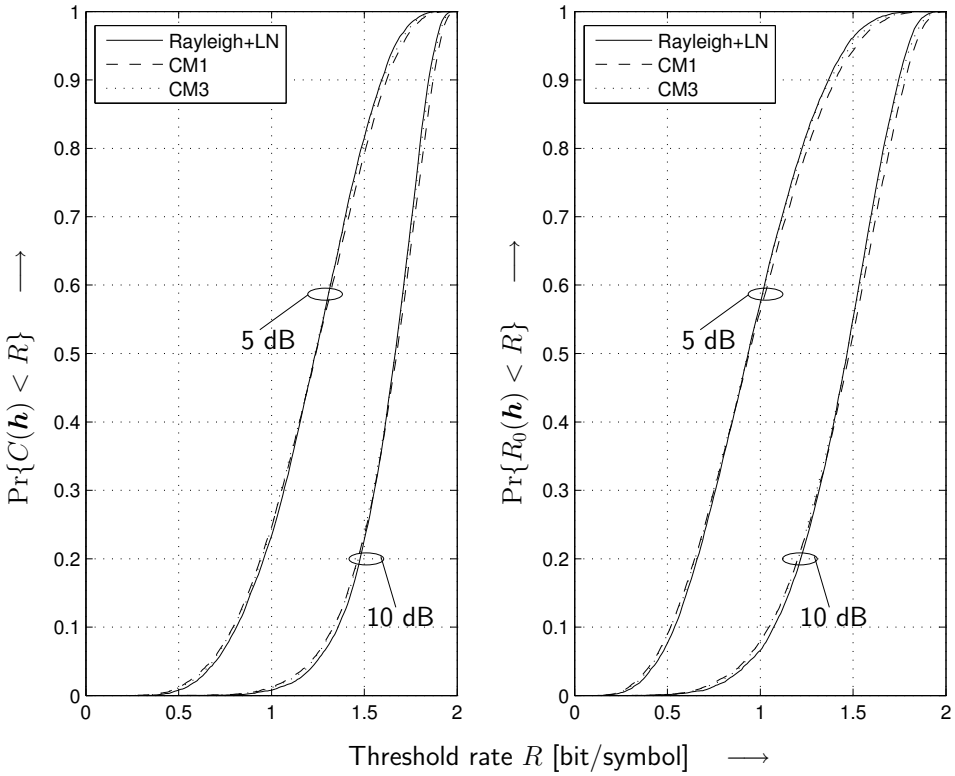

Figure 4.2: Outage probability for $10\log_{10}(\bar{E}_s/\mathcal{N}_0) = 5$ dB and 10 dB and perfect CSI. Left: Outage capacity. Right: Outage cutoff rate.

4.4.3 Numerical Results — No Loading

We evaluated expressions (4.12) and (4.13) via Monte Carlo simulation using 1000 realizations of each UWB channel model CM1-CM3. To keep the figures legible, we present representative results for CM1 and CM3 only. The performance of CM2 (not shown) is between that of CM1 and CM3 (cf. also Section 3.3.2). For comparison we also include results for independent and identically distributed (i.i.d.) Rayleigh fading on each tone and an outer lognormal shadowing term identical to that of the UWB models (labeled as "Rayleigh + LN").

Perfect CSI

First, we consider the case of perfect CSI. Figure 4.2 shows the outage capacity $\Pr\{C(\boldsymbol{h}) < R\}$ (left) and cutoff rate $\Pr\{R_0(\boldsymbol{h}) < R\}$ (right) as a function of the threshold rate R for $10\log_{10}(\bar{E}_s/\mathcal{N}_0) = 5$ dB and 10 dB, respectively, where $\bar{E}_s$ is the average received energy per symbol and $\mathcal{N}_0$ denotes the two-sided power spectral density of the complex noise.

It can be seen that both capacity and cutoff rate for the UWB channel models are similar to the respective parameters of an i.i.d. Rayleigh fading channel with additional lognormal shadowing. In fact, the curves for CM3, which provides the highest diversity (see Section 3.3.2), are essentially identical to those for the idealized i.i.d. model. The high diversity provided by the UWB channel also results in relatively steep outage curves, which means that transmission reliability can be considerably improved by deliberately introducing coding redundancy. This effect is slightly more pronounced for the capacity measure relevant for more powerful coding. On the other hand, the effect of shadowing, which cannot be averaged out by coding, causes a flattening towards low outage probabilities ≤ 0.1. In the high outage probability range we note that CM1 is slightly superior to CM3, which is due to the large dominant eigenvalues of CM1 identified in Section 3.3.2.

In Figure 4.3 we consider the 10% outage[3] capacity and cutoff rate as a function of the SNR $10\log_{10}(\bar{E}_s/\mathcal{N}_0)$. Again we note the close similarity between the UWB channel models and the i.i.d. Rayleigh fading channel with lognormal shadowing. A comparison of the capacity with the corresponding cutoff rate curves indicates that decent gains of 2.5 dB to 3 dB in power efficiency can be anticipated by the application of more powerful capacity approaching codes such as Turbo or RA codes (see also the simulation results in

[3]We note that 10% outage is a typically chosen value for UWB systems and the considered channel model [18].

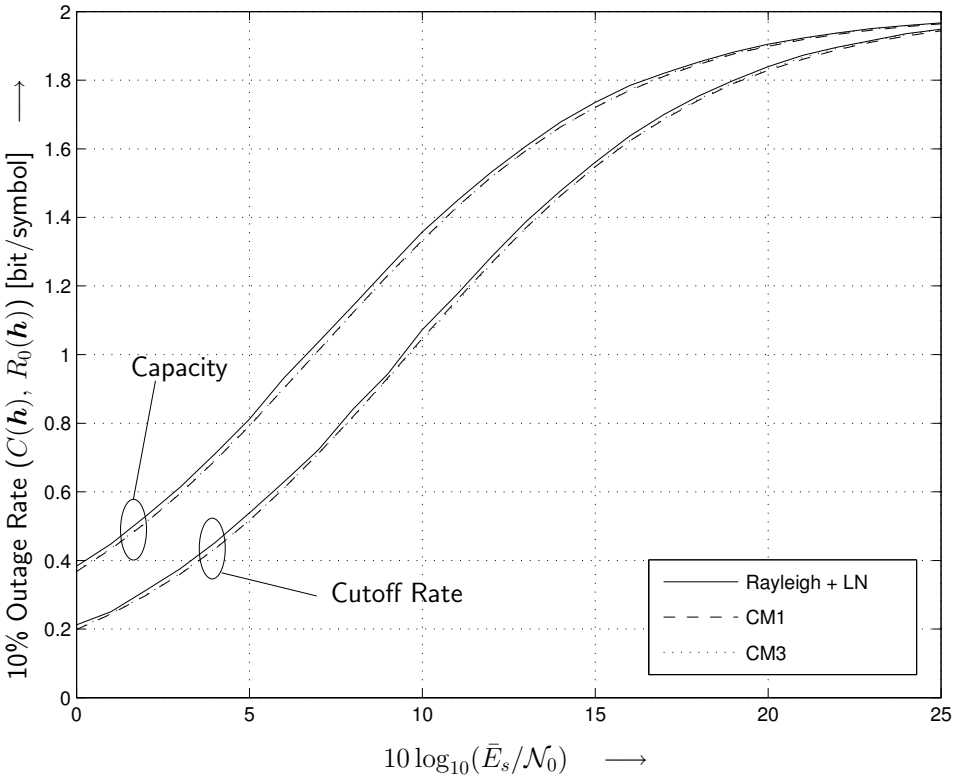

Figure 4.3: 10% outage capacity and cutoff rate for perfect CSI.

Section 4.5.1) instead of the convolutional codes used in the standard [24] which usually perform in the vicinity of the cutoff rate.

Imperfect CSI

Figure 4.4 shows the SNR loss due to LSE channel estimation according to (4.20) with various values of η. For reference, the MB-OFDM system uses $P = 2$, $N = 128$, and so choosing $L = 32$ leads to $\eta = 0.125$.

We can see from Figure 4.4 that the performance penalty $10\log_{10}(\gamma/\gamma_e)$ due to imperfect CSI is about 0.5 dB in the range of interest for MB-OFDM. The actual loss in $\bar{E}_s/\mathcal{N}_0$ is slightly different, since γ in Figure 4.4 is for a fixed lognormal shadowing and the actual $\bar{E}_s/\mathcal{N}_0$ loss must be obtained by averaging over the lognormal pdf. However,

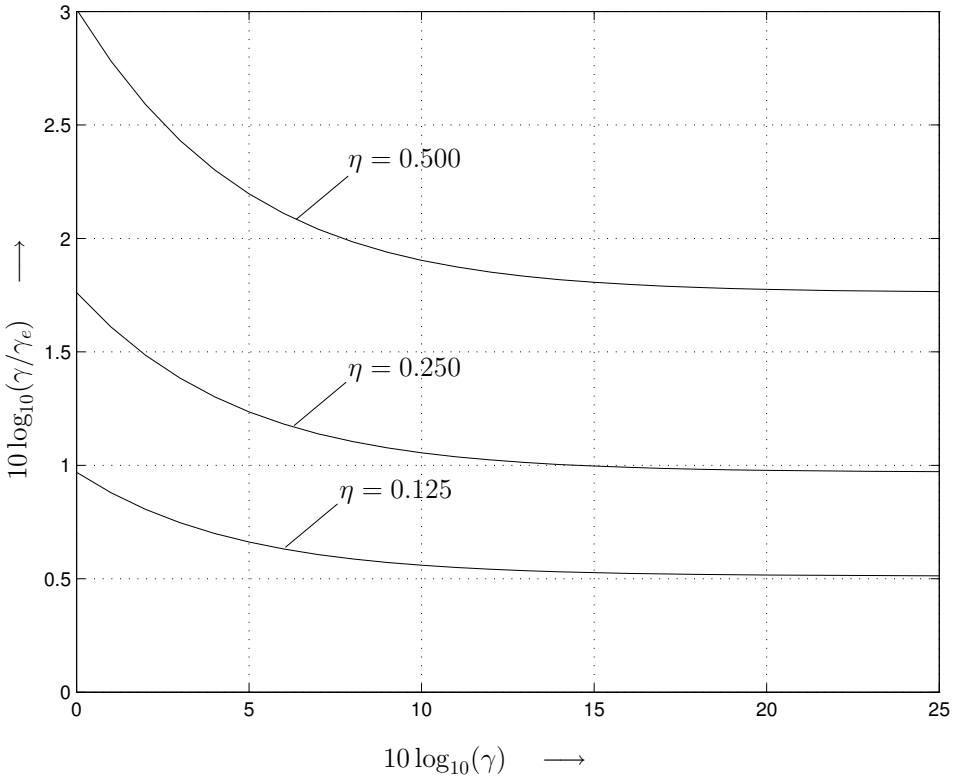

Figure 4.4: Loss in SNR due to LSE channel estimation with different η according to (4.20).

we can see from Figure 4.4 that the SNR loss is relatively constant for relevant values of γ, which (since the lognormal shadowing has a 0 dB mean), results in an $\bar{E}_s/\mathcal{N}_0$ loss of approximately $10\log_{10}(\gamma/\gamma_e)$. Reducing the channel estimation overhead to $P = 1$ ($\eta = 0.25$) could be an interesting alternative for short packets, as the additional loss is only about 0.5 dB (in terms of required energy per information bit $\bar{E}_b$ the loss is even smaller). Further reduction of pilot tones is not advisable as the gains in throughput are outweighed by the losses in power efficiency.

4.4.4 Numerical Results with Bit-Loading

In this section, we examine the capacity and cutoff rate of systems employing the Piazzo and CCB loading algorithms. We evaluated expressions (4.15) and (4.16) via Monte

Carlo simulation as discussed in Section 4.4.3.

No Clustering

Figure 4.5 (lines) shows the 10% outage capacity and cutoff rates for the CM1 channel using the Piazzo and CCB loading algorithms. (The markers in this figure will be discussed in Section 4.5.2). It should be noted that $\bar{E}_s$ is not adjusted to account for tones carrying 0 bits, because we assume operation at FCC transmit power limits, precluding the re-allocation of power from unused tones to other subcarriers (which would put the transmitted PSD beyond the allowed limits). We also do not adjust for the overhead associated with the feedback of loading information from the receiver to the transmitter. For high rates, both the CCB and the Piazzo loading algorithms provide a gain of several dB in capacity and in cutoff rate compared to the unloaded case, and this gain grows with increasing rate and $\bar{E}_s/\mathcal{N}_0$. The Piazzo algorithm is sub-optimal because it considers only the relative SNR between tones, and loads according to BER using a power minimization criterion. This loading strategy is not guaranteed to produce an increased channel capacity (or cutoff rate). On the other hand, the CCB algorithm requires knowledge of the actual SNR values of each tone and loads according to their approximate capacities, resulting in an increased channel capacity for all SNR values and an improved performance compared to Piazzo loading.

Clustering

We next consider the application of clustered loading using the modified CCB algorithm as described in Section 4.2. Figure 4.6 shows the 10% outage capacity (solid lines) and cutoff rate (dashed lines) for various values of cluster size D, for channels CM1 and CM3. Also included for comparison are the non-clustered loading ($D = 1$) and unloaded (all-QPSK) curves. As the cluster size D increases the attainable rates decrease because the

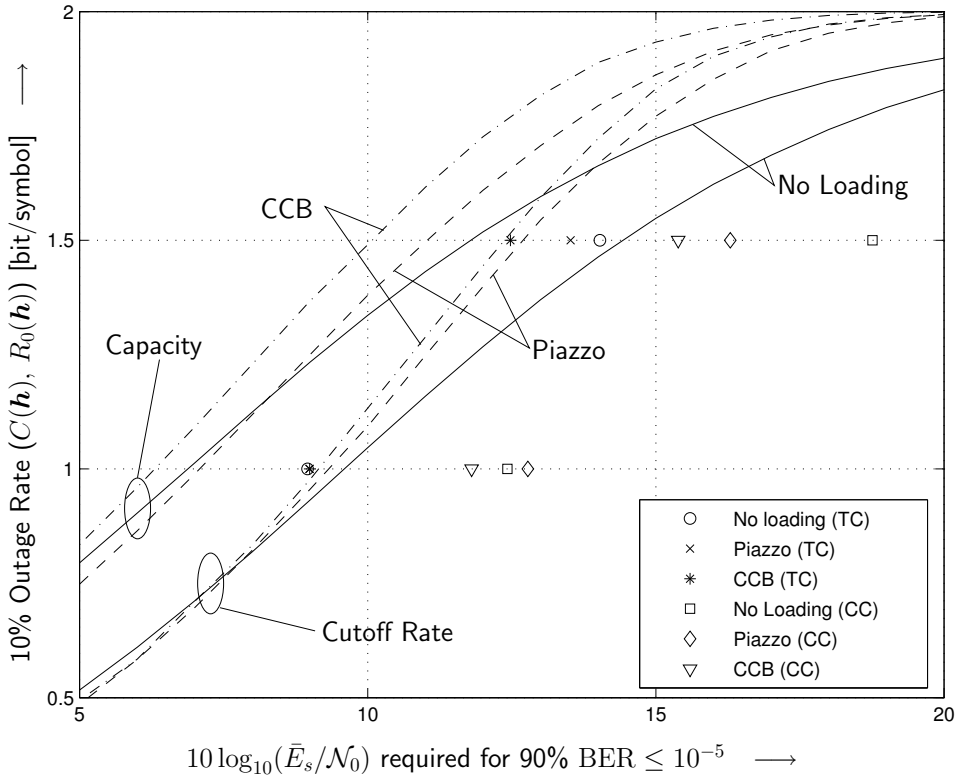

Figure 4.5: 10% outage capacity and cutoff rate with and without loading for CM1 (lines). $10\log_{10}(\bar{E}_s/\mathcal{N}_0)$ required to achieve BER $\leq 10^{-5}$ for the 90% best channel realizations using convolutional codes (CC) and Turbo codes (TC), with and without loading (markers).

modulation scheme chosen for each cluster is not optimal for all tones in the cluster. This loss is slightly more pronounced for the cutoff rate than for the capacity, which indicates that when using clustered loading we should expect more performance degradation with convolutional codes than with Turbo codes (see also Section 4.5.2). The performance degradation with increasing cluster size is higher for CM3 than for CM1, which can be predicted from the correlation matrix results of Section 3.3.2. Specifically, we note from Figure 3.3 that the frequency responses of adjacent subcarriers are more correlated (fewer significant eigenvalues) in CM1 and less correlated (more significant eigenvalues) in CM3. The less correlated the tones of a cluster are, the higher the average mismatch between the optimal modulation for each tone (i.e., that chosen by the non-clustered

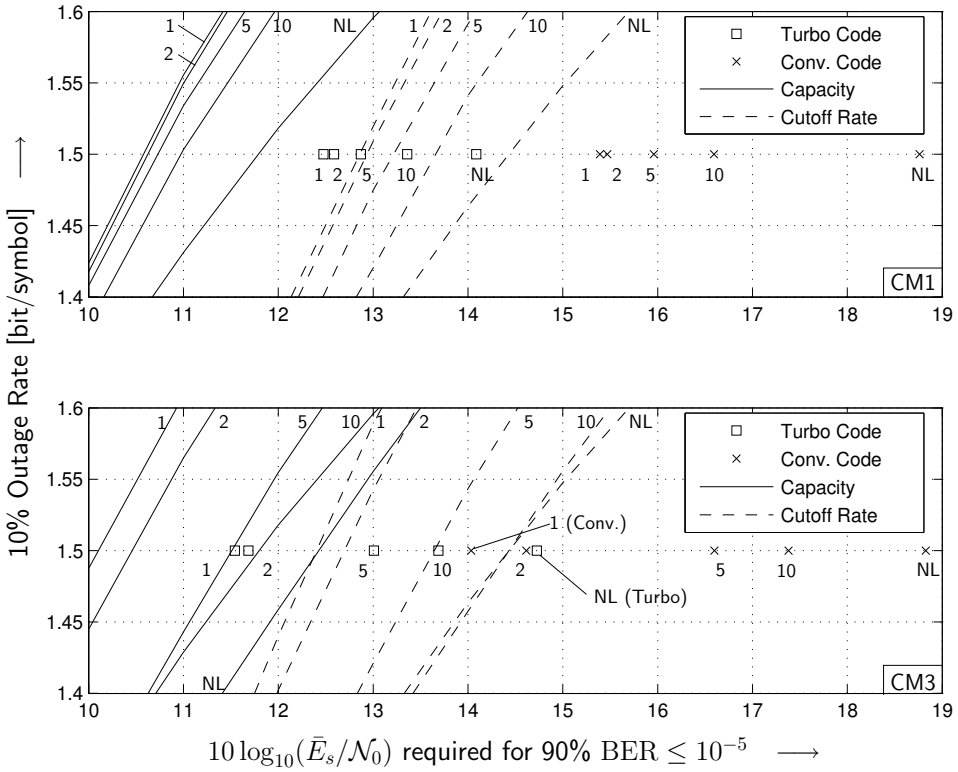

Figure 4.6: Lines: 10% outage capacity (solid) and cutoff rate (dashed) for clustered CCB loading (cluster sizes $D \in \{1, 2, 5, 10\}$) and for non-loaded QPSK ("NL"). Markers: $10\log_{10}(\bar{E}_s/\mathcal{N}_0)$ required to achieve BER $\leq 10^{-5}$ for the 90% best channel realizations using Turbo codes (□ markers) and convolutional codes (× markers). Channels CM1 (top) and CM3 (bottom).

loading algorithm) and the fixed modulation chosen for the cluster. The higher average mismatch on CM3 results in lower performance when clustered loading is applied.

4.5 Simulation Results

In Section 4.5.1, we study Turbo, RA, and convolutional coding without bit-loading. We examine channel CM1 for four different transmission modes with data rates of 80, 160, 320, and 480 Mbps corresponding to 0.25, 0.50, 1.00, and 1.50 bit/symbol, respectively (cf. Table 2.1). In the simulations, detection is performed with perfect CSI as well as

with LSE channel estimation using $\eta = 0.125$. We then turn to the performance of systems with loading in Section 4.5.2. Based on the results of the information-theoretic analysis of Section 4.4.4, we restrict our attention to rates ≥ 1.00 bit/symbol, where we expect loading algorithms to yield performance gains. We concentrate on Turbo and convolutional codes for this section. The simulation results presented in these two sections are the worst-case $10\log_{10}(\bar{E}_s/\mathcal{N}_0)$ values required to achieve BER$\leq 10^{-5}$ for the best 90% of channel realizations over a set of 100 channels (i.e., they are simulation results corresponding to 10% outage).

In Section 4.5.3, we briefly summarize the power efficiency gains and attendant range improvements expected from the application of the system extensions we have proposed.

4.5.1 No Loading

Figure 4.7 (markers) shows SNR points when using convolutional codes (as in MB-OFDM), together with the corresponding 10% outage cutoff rate curves. We observe that the simulated SNR points are approximately 3 dB to 4 dB from the cutoff-rate curves, which is reasonable for the channel model and coding schemes under consideration. These results (a) justify the relevance of the information-theoretic measure and (b) confirm the coding approach used in MB-OFDM. More specifically, the diversity provided by the UWB channel is effectively exploited by the chosen convolutional coding and interleaving scheme. Furthermore, the system with LSE channel estimation performs within 0.5–0.7 dB of the perfect CSI case as was expected from the cutoff-rate analysis (see also the discussion in Section 4.4.3 on the relationship between the $10\log_{10}(\gamma/\gamma_e)$ loss and the $10\log_{10}(\bar{E}_s/\mathcal{N}_0)$ loss).

We next consider the Turbo and RA coding schemes. Figure 4.8 (markers) shows the simulation results for Turbo and RA codes on channel CM1 with perfect CSI, as

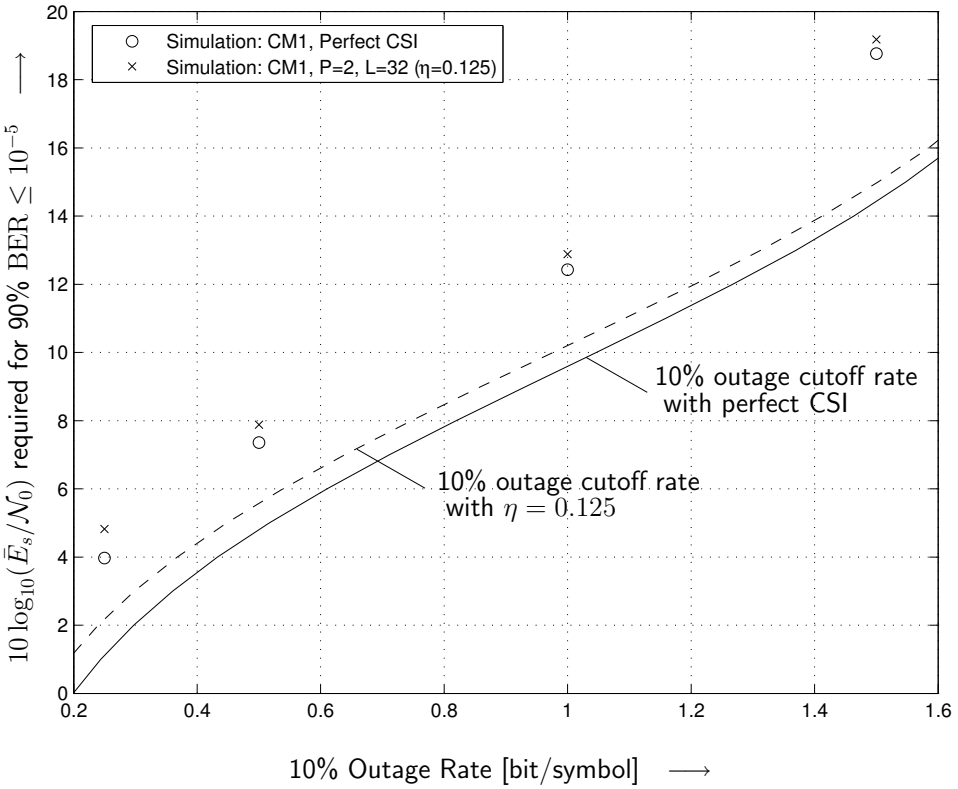

Figure 4.7: $10\log_{10}(\bar{E}_s/\mathcal{N}_0)$ required to achieve BER $\leq 10^{-5}$ for the 90% best channel realizations using convolutional codes (markers). For comparison: 10% outage cutoff rate (lines). Channel model CM1 and LSE channel estimation.

well as the convolutional code results for comparison. We also show the corresponding 10% outage capacity and cutoff rate curves. Turbo codes give a performance gain of up to 5 dB over convolutional codes, and perform within 2.5 dB of the channel capacity, depending on the rate. At rates of 0.25 and 0.50 bit/symbol, Turbo code interleaver sizes compatible with the channel interleaver design of the MB-OFDM standard (the "std" points) incur a performance penalty of 1–2 dB compared with the longer block length ("K=600") points. RA codes have a performance roughly 1 dB worse than the long block-length Turbo codes, but the RA codes are both (a) compatible with the MB-OFDM channel interleaver, and (b) less complex to decode. They are thus a good candidate for low-rate MB-OFDM transmission.

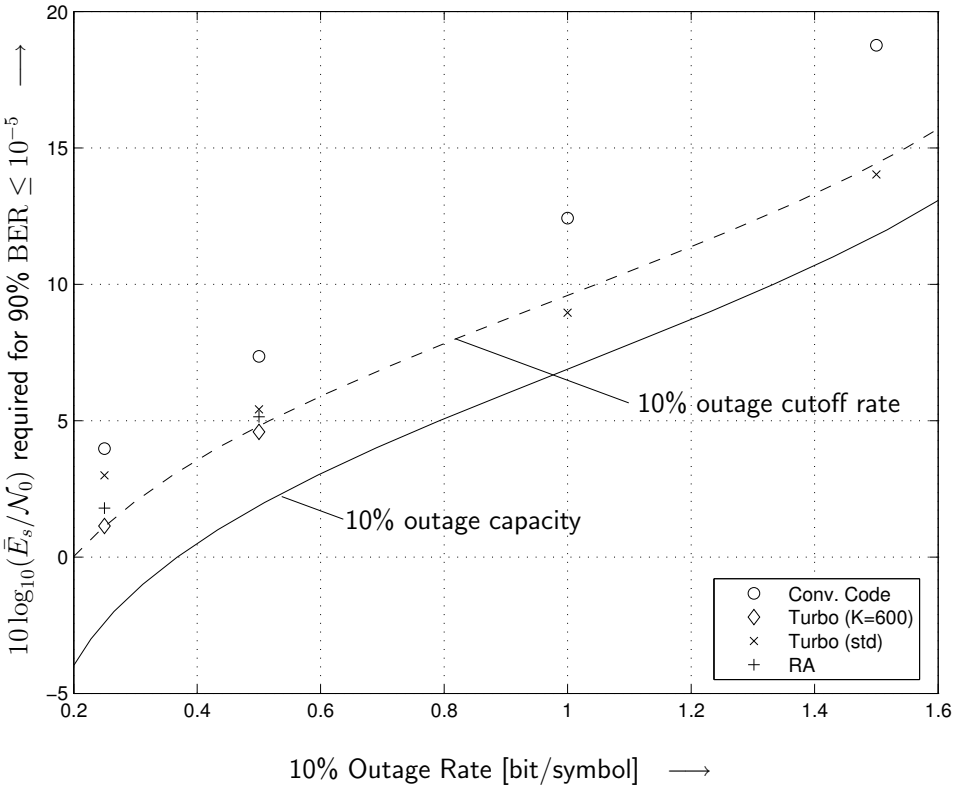

Figure 4.8: $10\log_{10}(\bar{E}_s/\mathcal{N}_0)$ required to achieve BER $\leq 10^{-5}$ for the 90% best channel realizations using Turbo Codes, RA codes, and convolutional codes (markers). For comparison: 10% outage capacity and cutoff rate (lines). Channel model CM1 and perfect CSI.

4.5.2 With Loading

Figure 4.5 (markers) shows the simulation results for Turbo codes and for convolutional codes, using both the CCB and Piazzo loading algorithms on channel CM1 with perfect CSI. At 1.00 bit/symbol and using convolutional codes, we see a performance gain of less than 1 dB using CCB loading, and a slight performance degradation using Piazzo loading. Performance using Turbo codes at 1.00 bit/symbol is relatively constant regardless of loading. However, at 1.50 bit/symbol we see gains of approximately 1.5 dB for Turbo codes and almost 4 dB for convolutional codes when CCB loading is used. The gains using the Piazzo algorithm are approximately 1 dB less, as predicted by the

capacity analysis of Section 4.4.4. Finally, we note that at 1.50 bit/symbol the system employing CCB loading and Turbo codes is approximately 6 dB better than the unloaded convolutionally coded system, and performs within approximately 2.5 dB of the channel capacity.

In Figure 4.6 (markers) we consider the performance of clustered loading with Turbo codes and with convolutional codes for 1.50 bit/symbol on the CM1 and CM3 channels with perfect CSI. As predicted by information-theoretic analysis, clustered loading incurs a performance penalty with increasing cluster size D. We note that Turbo codes suffer a smaller performance degradation (relative to $D=1$) than convolutional codes, because the more powerful Turbo code is better suited to handle the mismatched modulation (as discussed in Section 4.4.4). The performance degradation is larger for CM3 due to that channel model's lower correlation between adjacent subcarrier frequency responses and resultant larger loading mismatch. However, even $D=10$ loading provides performance gains for both channels and code types. Cluster size $D=2$ is a good tradeoff point for both Turbo and convolutional codes, allowing for feedback reduction by a factor of 2 with losses of approximately 0.1 dB for CM1 and 0.4 dB for CM3. Cluster sizes as large as $D=5$ could be used with Turbo codes, depending on the required power efficiency and expected channel conditions.

4.5.3 Range Improvements from Turbo Codes and Loading

Table 4.1 lists the gains in required $10\log_{10}(\bar{E}_s/\mathcal{N}_0)$ and percentage range increases on channel CM1 for various combinations of the extensions we have proposed. We assume a path loss exponent of $d = 2$, as in [28]. We can see that bit loading alone provides up to 47% increase in range, Turbo codes without loading provide a 71% increase, and the combination of Turbo codes and loading allows for a 106% increase in range. Further-

Table 4.1: Power efficiency gains and range increases available using some of the extensions considered, compared to the MB-OFDM standard. Channel CM1, rate 1.50 bit/symbol (480 Mbps), path loss exponent $d=2$. $10\log_{10}(\bar{E}_s/\mathcal{N}_0)$ values are those required to achieve BER $\leq 10^{-5}$ for the 90% best channel realizations. (CC: convolutional code, TC: Turbo code, CL: clustered loading).

System	$10\log_{10}(\bar{E}_s/\mathcal{N}_0)$	Gain (dB)	% range increase
CC, no loading (Standard)	18.76	–	–
CC, CCB loading	15.38	3.38	47 %
CC, $D=2$ CL	15.47	3.29	46 %
TC, no loading	14.09	4.67	71 %
TC, CCB loading	12.48	6.28	106 %
TC, $D=2$ CL	12.58	6.18	103 %

more, the use of clustered loading with $D=2$ only reduces these range improvements by 1% to 3% over the non-clustered case, while providing reduced-rate feedback and lower computational complexity.

4.6 Conclusions

In this chapter, the application of MB-OFDM for UWB communication has been analyzed. We have found that the information-theoretic limits of the UWB channel are similar to those of a perfectly interleaved Rayleigh fading channel with shadowing. The BICM-OFDM scheme employed in MB-OFDM performs close to the outage cutoff-rate measure and is thus well suited to exploit the available diversity. The application of stronger coding, such as Turbo codes or RA codes, improves power efficiency by up to 4.7 dB, depending on the data rate. Bit-loading algorithms applied to standard MB-OFDM systems provide gains of about 3.4 dB, while loading in conjunction with Turbo codes provides gains of up to 6.3 dB for high data rates. A simple clustering scheme allows for reduced-rate feedback of loading information, with minimal losses of 0.1–0.2 dB

in power efficiency, depending on the channel conditions and required feedback reduction. Finally, a simple LSE channel estimator has been shown to enable performance within 0.5–0.7 dB of the perfect CSI case for the MB-OFDM system.

5 Error Rate Analysis for MB-OFDM Systems

5.1 Introduction

In Chapter 4, we presented MB-OFDM performance results obtained via time-consuming system simulations. In this chapter, we focus on the development of analysis techniques to approximate the error rate of MB-OFDM systems *without* having to resort to simulations.

The difficulty of MB-OFDM error rate analysis lies in the combination of BICM-OFDM and the quasi-static, frequency-selective channel model. There are well-known techniques for bounding the performance of convolutionally-encoded transmission over many types of fading channels, e.g. [1, 27]. However, such classical BER analysis techniques are not applicable to MB-OFDM for several reasons. Firstly, the short-length channel-coded packet-based transmissions are non-ideally interleaved, which results in non-zero correlation between adjacent coded bits. Secondly, and more importantly, the quasi-static nature of the channel limits the number of distinct channel gains to the (relatively small) number of OFDM tones. This small number of distinct channel gains must not be approximated by the full fading distribution for a valid performance analysis, as would be the case in a fast-fading channel.

Motivated by the considerations mentioned above, we have developed two analytical methods to evaluate MB-OFDM performance. The first method approximates the BER on a *per-realization* basis. This method is most suitable for obtaining the outage BER, i.e., the minimum expected BER performance after excluding some percentage of the worst-performing channel realizations [87, Section III.C-2], but can also be used to obtain the average BER performance. For quasi-static channels with correlated Rayleigh-distributed subcarrier channel gains, we present an alternative method to directly and efficiently obtain the average BER performance.

Because of the potential for interference in MB-OFDM systems (inherent in the spectral underlay techniques used in UWB), we also model narrowband interference as a sum of tone interferers, and incorporate the effects of this interference into both analysis methods. Furthermore, we study erasure marking and decoding [88, 89] as a mitigation technique for tone-interference-impaired coded MB-OFDM.

As the techniques developed in this chapter are applicable to a more general class of BICM-OFDM systems, including IEEE 802.11a/g [21] and IEEE 802.16 [22, 90] in addition to MB-OFDM, we adopt a generic OFDM signal model in this chapter, and focus our attention on MB-OFDM in the numerical results in Section 5.4.

There are several prior related works in this area. In [91], Malkamäki and Leib consider the performance of convolutional codes with non-ideal interleaving over *block* fading channels without interference. They make use of the generalized transfer function (GTF) [92] method in order to obtain the pairwise error probability (PEP). If their technique is applied to systems with a fading block length of one (equivalent to the quasi-static channel), their approach is similar in some ways to Method I presented in Section 5.3.3. The major difference is that Method I does not require the GTF of the code, which may become difficult to obtain as the number of distinct channel gains (the number of blocks in the case of a block-fading channel) grows [93]. Instead, we apply

the novel concept of error vectors, introduced in Section 5.3.1.

The PEP for uncoded and coded (across subcarrier) MB-OFDM is given in [30]. However, the authors apply a non-standard UWB channel model, consider only simple codes such as repetition coding, and do not consider interference.

The remainder of this chapter is organized as follows. Section 5.2 introduces the OFDM transmitter and receiver models as well as the models for the channel and for the interfering signals. Each model is formulated quite generally, although we also mention the specific parameters for the MB-OFDM system, which will be the focus of the numerical results presented. In Section 5.3, we develop the proposed analysis methods, which allow for per-channel-realization as well as average error rate approximations with and without sum-of-tones interference. Analysis and simulation results for several practically relevant scenarios of interest for MB-OFDM are given and discussed in Section 5.4. Finally, Section 5.5 concludes this chapter.

5.2 System Model

In this section, we introduce generic models for the OFDM transmitter, channel, interference, and OFDM receiver. We again note that we will focus on MB-OFDM in the numerical results of Section 5.4.

5.2.1 Transmitter

Throughout this chapter we consider a generic N-subcarrier OFDM system with M-ary QAM (M-QAM) carrying $R_m = \log_2(M)$ bits per subcarrier. Figure 5.1 shows the relevant portions of the OFDM transmitter. The system employs a punctured convolutional code of rate R_c. We assume that the transmitter selects $R_c R_m N$ random message bits for transmission, denoted by $\boldsymbol{b} = [b_1 \; b_2 \ldots b_{R_c R_m N}]^T$. The vectors $\boldsymbol{c}$ and $\boldsymbol{c}^\pi$ of length

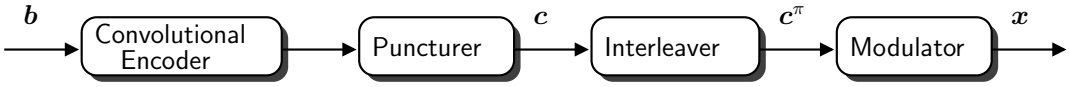

Figure 5.1: Relevant portions of the OFDM transmitter.

$L_c = R_m N$ represent the bits after encoding/puncturing and after interleaving, respectively. The bits $\boldsymbol{c}^\pi$ are then modulated using M-QAM on each subcarrier, and the resulting N modulated symbols are denoted by $\boldsymbol{x} = [x_1\ x_2\ \ldots\ x_N]^T$.

As discussed in Chapter 2, MB-OFDM specifies QPSK modulation (equivalent to 4-QAM [1]) with Gray labeling. In Section 5.4, we will also consider Gray-labeled 16-QAM as a potential extension for increased data rates. After modulation, modulated symbols are optionally repeated in two consecutive OFDM symbols and/or two subcarriers within the same OFDM symbol (cf. Section 2.5). We can equivalently consider this repetition as a lower-rate convolutional code with repeated generator polynomials.

5.2.2 Channel Model

We will assume that the OFDM system is designed such that the cyclic prefix is longer than the CIR. Thus, we can equivalently consider the channel in the frequency domain, and denote the subcarrier gains by $\boldsymbol{h} = [h_1\ h_2\ \ldots\ h_N]^T$. We also include the frequency-domain interference signal $\boldsymbol{p}$ (see Section 5.2.3). The transmitted symbols $\boldsymbol{x}$ pass through the fading channel $\boldsymbol{H} = \mathrm{diag}(\boldsymbol{h})$, and the length-$N$ vector of received symbols $\boldsymbol{r}$ (after the FFT) is given by

$$\boldsymbol{r} = \boldsymbol{H}\boldsymbol{x} + \boldsymbol{p} + \boldsymbol{n}\ , \tag{5.1}$$

where $\boldsymbol{n}$ is a vector of independent complex AWGN variables with variance $\mathcal{N}_0$. We denote the energy per modulated symbol by $E_s = R_c R_m E_b$, where E_b is the energy per information bit.

When presenting numerical results, we will adopt the 802.15.3a UWB channel model

presented in Chapter 3. As discussed in that chapter, the elements of $\boldsymbol{h}^n$ are well-approximated as zero-mean complex Gaussian random variables. This allows us to apply analysis assuming correlated Rayleigh fading coefficients (see Section 5.3.4) to the UWB channel without lognormal shadowing, and then average over the lognormal shadowing distribution in order to obtain the final system performance over the UWB channel. We note that this is only relevant for the method in Section 5.3.4 — for the realization-based method (see Section 5.3.3) the distribution of $\boldsymbol{h}$ is not important.

5.2.3 Interference Model

We model narrowband interference as the sum of N_i tone interferers

$$i(t) = \sum_{k=1}^{N_i} i_k(t) \ , \tag{5.2}$$

where the equivalent complex baseband representation of the kth tone interferer with amplitude α_k, frequency f_k, and initial phase ϕ_k is given by

$$i_k(t) = \alpha_k e^{j(2\pi f_k t + \phi_k)} \ . \tag{5.3}$$

Assuming that the interference $i(t)$ falls completely in the passband of the receiver filter before sampling, we form the discrete-time equivalent interference by sampling $i(t)$ with the OFDM system sampling period T, and obtain (for one OFDM symbol) the N sample vector

$$\boldsymbol{i} = [i(0) \quad i(T) \quad i(2T) \quad \ldots \quad i((N-1)T)]^T \ . \tag{5.4}$$

Therefore, the frequency-domain equivalent $\boldsymbol{p}$ of the interfering signal, considered in (5.1), is given by

$$\boldsymbol{p} = \mathrm{DFT}(\boldsymbol{i}) \ . \tag{5.5}$$

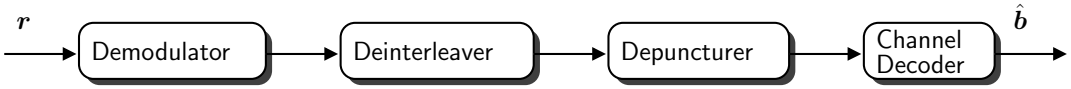

Figure 5.2: Relevant portions of the OFDM receiver.

We note that, due to the finite-length DFT window, each single-tone interferer is convolved by a sinc function in the frequency domain. If f_k is equal to one of the subcarrier frequencies, only one subcarrier is impaired by the interferer $i_k(t)$ (since the interferer will be zero at the other subcarrier frequencies). On the other hand, if f_k happens to lie between two subcarriers, the tone interferer will affect several adjacent subcarriers.

5.2.4 Receiver

The relevant portions of the OFDM receiver are shown in Figure 5.2. We assume perfect timing and frequency synchronization. The receiver employs a soft-output detector followed by a deinterleaver and a depuncturer. After possible erasure marking based on knowledge of $f_k, 1 \leq k \leq N_i$ (see Section 5.4.4 for details), standard Viterbi decoding results in an estimate $\hat{\boldsymbol{b}} = [\hat{b}_1\ \hat{b}_2\ \ldots\ \hat{b}_{R_c R_m N}]^T$ of the originally transmitted information bits. This receiver structure is compliant with the MB-OFDM standard [24].

5.3 Performance Analysis

In this section, we present two methods for approximating the performance of coded multicarrier systems operating over frequency-selective, quasi-static fading channels and impaired by sum-of-tones interference. The first method (Section 5.3.3) is based on approximating the performance of the system for individual channel realizations. The main strength of this method is that it can be used to obtain the outage BER performance (the standard performance measure considered in MB-OFDM systems [18, 24, 28]). While

the first method can also be used to obtain the average BER over an ensemble of channel realizations, the second method (Section 5.3.4), which is based on knowledge of the correlation matrix of the frequency-domain channel gains, can be used to directly obtain the average performance without the need to consider a large ensemble of channels. Both methods are based on considering the set of error vectors, introduced in Section 5.3.1, and the PEP of an error vector, given in Section 5.3.2.

One major problem in the analysis of M-QAM schemes with $M > 4$ is that the probability of error for a given bit depends on the whole transmitted symbol (i.e. it also depends on the other bits in the symbol). For this reason, for the combination of convolutional coding and M-QAM it is not sufficient to adopt the classical approach of considering deviations from the all-zero codeword only. In theory, one must average over all possible choices for $\boldsymbol{c}$. Since this is computationally intractable, we simply assume the transmitted information bits $\boldsymbol{b}$ (and thus $\boldsymbol{x}$) are chosen randomly. For $M = 4$ (where the joint linearity of code and modulator is maintained) this is exactly equivalent to considering an all-zero codeword. In the case of $M > 4$, we have verified for various example scenarios that, for the two analysis methods proposed below, a random choice of $\boldsymbol{b}$ well-approximates the true system performance.

5.3.1 Error Vectors

Consider a convolutional encoder initialized to the all-zero state, where the reference (correct) codeword is the all-zero codeword. We construct all L input sequences which cause an immediate deviation from the all-zero state (i.e., those whose first input bit is 1) and subsequently return the encoder to the all-zero state with an output Hamming weight of at most $w_{\max}$. Let $\mathcal{E}$ be the set of all vectors $\boldsymbol{e}_\ell$ ($1 \leq \ell \leq L$) representing the

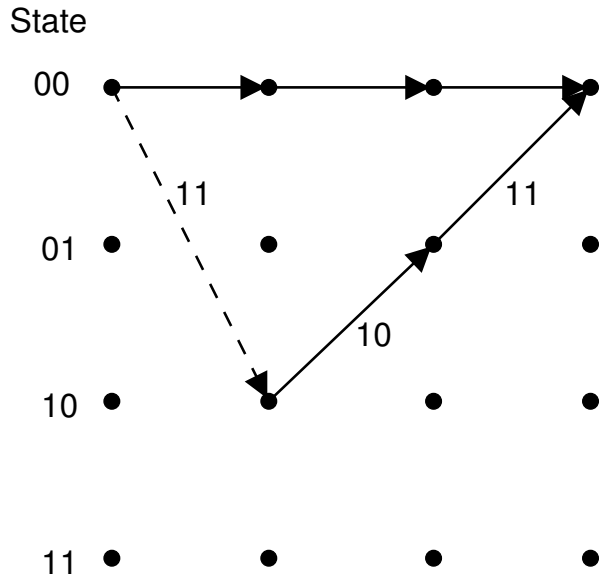

Figure 5.3: Example error vector for the $R_c = 1/2$ $(7,5)_8$ code. Dashed line: "1" input bit, solid line: "0" input bit. $\boldsymbol{e} = [1,1,1,0,1,1]$. Length $l = 6$, input weight $a = 1$.

output sequences (after puncturing) associated with these input sequences, i.e.,

$$\mathcal{E} = \{\boldsymbol{e}_1, \boldsymbol{e}_2, \ldots, \boldsymbol{e}_L\} \ . \tag{5.6}$$

Let l_ℓ be the length of $\boldsymbol{e}_\ell$ (the number of output bits after puncturing), and let a_ℓ be the Hamming weight of the input associated with $\boldsymbol{e}_\ell$. Note that the choice of $\omega_{\max}$ governs the value of L (i.e. once the maximum allowed Hamming weight is set, the number of error events L is known). We term $\boldsymbol{e}_\ell$ an "error vector" and $\mathcal{E}$ the set of error vectors.

In Figure 5.3, we show an example error vector for the $R_c = 1/2$ $(7,5)_8$ convolutional code. Input bits of 1 are indicated by dashed lines on the trellis, while 0 input bits are shown by solid lines. The error vector for this particular deviation is $\boldsymbol{e} = [1,1,1,0,1,1]$, and has length $l = 6$ and input Hamming weight $a = 1$.

The set $\mathcal{E}$ contains all the low-weight error events, which are the most likely deviations in the trellis. As with standard union-bound techniques for convolutional codes [1], the low-weight terms will dominate the error probability. Therefore, it is sufficient to

choose a small $w_{\max}$ — for example, the punctured MB-OFDM code of rate $R_c = 1/2$ (cf. Chapter 2) has a free distance of 9, and choosing $w_{\max} = 14$ (resulting in a set of $L = 242$ error vectors of maximum length $l = 60$) provides results which are not appreciably different from those obtained using larger $w_{\max}$ values.

We obtained $\mathcal{E}$ by modifying an algorithm for calculating the convolutional code distance spectrum [94] in order to store the code output sequences (i.e. the error vectors $\boldsymbol{e}_\ell$) in addition to the distance spectrum information.

5.3.2 PEP for an Error Vector

We now consider error events starting in a given position i of the codeword ($1 \leq i \leq L_c$). For a specific error vector $\boldsymbol{e}_\ell$ ($1 \leq \ell \leq L$), form the full error codeword

$$\boldsymbol{q}_{i,\ell} = [\underbrace{0 \;\; 0 \;\; \ldots \;\; 0}_{i-1} \;\; \underbrace{\boldsymbol{e}_\ell}_{l_\ell} \;\; \underbrace{0 \;\; 0 \;\; \ldots \;\; 0}_{L_c - l_\ell - i + 1}]^T \tag{5.7}$$

of length L_c by padding $\boldsymbol{e}_\ell$ with zeros on both sides as indicated above. Given the error codeword $\boldsymbol{q}_{i,\ell}$ and given that codeword $\boldsymbol{c}$ is transmitted, the competing codeword is given by

$$\boldsymbol{v}_{i,\ell} = \boldsymbol{c} \oplus \boldsymbol{q}_{i,\ell} \quad . \tag{5.8}$$

The decoder employs a standard Euclidean distance metric (i.e. the interference signal is assumed to be unknown for calculation of the metric). Letting $\boldsymbol{z}_{i,\ell}$ be the vector of M-QAM symbols associated with $\boldsymbol{v}^{\pi}_{i,\ell}$ (the interleaved version of $\boldsymbol{v}_{i,\ell}$), and recalling that $\boldsymbol{x}$ is the modulated symbol vector corresponding to the original codeword $\boldsymbol{c}$, the PEP for the ℓth error vector starting in the ith position, i.e. the probability that $\boldsymbol{v}_{i,\ell}$ is detected

given that $\boldsymbol{c}$ was transmitted, is given by

$$\mathrm{PEP}_{i,\ell}(\boldsymbol{H},\boldsymbol{p}) = \Pr\left\{||\boldsymbol{r}-\boldsymbol{H}\boldsymbol{x}||^2 > ||\boldsymbol{r}-\boldsymbol{H}\boldsymbol{z}_{i,\ell}||^2 \;\middle|\; \boldsymbol{H},\boldsymbol{p}\right\} . \tag{5.9}$$

In Sections 5.3.3 and 5.3.4, we will obtain various forms for this general expression.

5.3.3 Per-realization Performance Analysis ("Method I")

In this section, we obtain an approximation of the BER for a particular channel realization $\boldsymbol{H} = \mathrm{diag}(\boldsymbol{h})$ and interference $\boldsymbol{p}$, which we denote as $P(\boldsymbol{H},\boldsymbol{p})$. For simplicity, we refer to this method as "Method I" in the remainder of this chapter. As noted above and discussed in more detail in Section 5.3.3, the main strength of this method is the ability to obtain the outage BER of coded OFDM systems.

Pairwise Error Probability (PEP)

The PEP for an error vector $\boldsymbol{e}_\ell$ $(1 \le \ell \le L)$ with the error event starting in a position i $(1 \le i \le L_c)$ is given by (5.9). For a given $\boldsymbol{H}$ and $\boldsymbol{p}$, and after some straightforward manipulations, we obtain the expression

$$\mathrm{PEP}_{i,\ell}(\boldsymbol{H},\boldsymbol{p}) = Q\left(\frac{\frac{1}{2}||\boldsymbol{H}(\boldsymbol{x}-\boldsymbol{z}_{i,\ell})||^2 + \mathrm{Re}\left\{\boldsymbol{p}^H\boldsymbol{H}(\boldsymbol{x}-\boldsymbol{z}_{i,\ell})\right\}}{\sqrt{\frac{1}{2}\mathcal{N}_0||\boldsymbol{H}(\boldsymbol{x}-\boldsymbol{z}_{i,\ell})||^2}}\right) . \tag{5.10}$$

It is insightful to examine (5.10) for two special cases:

- $\mathcal{N}_0 \to 0$ (the low-noise region): In this case, there are two possible outcomes. If the numerator in (5.10) is positive, we have the Q-function of a large positive value and thus PEP $\to 0$. However, if the interference $\boldsymbol{p}$ causes the numerator to become negative, we have the Q-function of a large negative value and thus

PEP $\to 1$. That is, we either (depending on $\boldsymbol{p}$) will surely make an error, or will surely *not* make an error.

- $\boldsymbol{p} = \mathbf{0}_{N\times 1}$ (no interference): Here we can simplify (5.10) to obtain

$$\mathrm{PEP}_{i,\ell}(\boldsymbol{H}, \boldsymbol{p}) = Q\left(\sqrt{\frac{||\boldsymbol{H}(\boldsymbol{x} - \boldsymbol{z}_{i,\ell})||^2}{2\mathcal{N}_0}}\right) . \tag{5.11}$$

Per-realization BER

The corresponding bit error rate for the ℓth error vector, starting in the ith position, is given by

$$P_{i,\ell}(\boldsymbol{H}, \boldsymbol{p}) = a_\ell \cdot \mathrm{PEP}_{i,\ell}(\boldsymbol{H}, \boldsymbol{p}) . \tag{5.12}$$

Summing over all L error vectors, we obtain an approximation of the BER for the ith starting position as

$$P_i(\boldsymbol{H}, \boldsymbol{p}) = \sum_{\ell=1}^{L} P_{i,\ell}(\boldsymbol{H}, \boldsymbol{p}) . \tag{5.13}$$

We note that (5.13) can be seen as a standard truncated union bound for convolutional codes (i.e. it is a sum over all error events of Hamming weight less than $\omega_{\max}$). We also note that we can tighten this bound by limiting P_i to a maximum value of $1/2$ before averaging over starting positions [91]. Finally, since all starting positions are equally likely, the BER $P(\boldsymbol{H}, \boldsymbol{p})$ can be written as

$$P(\boldsymbol{H}, \boldsymbol{p}) = \frac{1}{L_c} \sum_{i=1}^{L_c} \min\left[\frac{1}{2}, \sum_{\ell=1}^{L} P_{i,\ell}(\boldsymbol{H}, \boldsymbol{p})\right] . \tag{5.14}$$

Table 5.1 contains pseudocode to calculate $P(\boldsymbol{H}, \boldsymbol{p})$ according to (5.14).

Table 5.1: Pseudocode for Method I.

Method I	Final BER is P (for given $\boldsymbol{H}$, $\boldsymbol{p}$).
1	P := 0
2	for i := 1 to L_c do
3	P_i := 0
4	for ℓ := 1 to L do
5	form $\boldsymbol{q}_{i,\ell}$ as per (5.7)
6	form $\boldsymbol{v}_{i,\ell}$ as per (5.8)
7	form $\boldsymbol{v}^{\pi}_{i,\ell}$ and $\boldsymbol{z}_{i,\ell}$ from $\boldsymbol{v}_{i,\ell}$
8	calculate $\mathrm{PEP}_{i,\ell}$ as per (5.10)
9	calculate $P_{i,\ell}$ as per (5.12)
10	P_i := P_i + $P_{i,\ell}$
11	endfor
12	P := P + min($\frac{1}{2}$,P_i)
13	endfor
14	P := P / L_c

Average and Outage BER

The average BER for a given interference can be obtained by averaging (5.14) over a (large) number N_c of channel realizations, where the ith channel realization is denoted by $\boldsymbol{H}_i$ ($1 \leq i \leq N_c$), as

$$P(\boldsymbol{p}) = \frac{1}{N_c} \sum_{i=1}^{N_c} P(\boldsymbol{H}_i, \boldsymbol{p}) \; . \tag{5.15}$$

As mentioned previously, Method I also readily lends itself to the consideration of the outage BER, a common measure of performance for packet-based systems operating in quasi-static channels [87]. The outage BER[1] provides a measure of the minimum performance that can be expected of the system given a specified $X\%$ outage rate, and is often employed in UWB system performance studies [18, 24, 28]. We evaluate (5.14) for a set of N_c channel realizations $\mathcal{H} = \{\boldsymbol{H}_i, 1 \leq i \leq N_c\}$. The worst-performing $X\%$ of realizations are considered in outage, and those channel realizations are denoted by

[1]An alternative measure of outage is the *outage probability*, i.e. the probability that the BER exceeds some nominal value BER_0 in an OFDM block. The outage probability can also be obtained given the per-realization BER in (5.14).

$\mathcal{H}_{\text{out}}$. Denoting the remaining $(100 - X)\%$ of channel realizations by $\mathcal{H}_{\text{in}}$, the outage BER is given by

$$P_{\text{out}}(\boldsymbol{p}) = \max_{\boldsymbol{H}_i \in \mathcal{H}_{\text{in}}} P(\boldsymbol{H}_i, \boldsymbol{p}) \; . \tag{5.16}$$

In Section 5.4, we will focus on results for fixed values of signal-to-interference ratio (SIR), interferer amplitude α_k, and interferer frequency f_k. However, in order to remove the effect of the interferer initial phase, we will average (5.15) and (5.16) over 32 uniformly-distributed values of $\phi_k \in [0, 2\pi)$.

5.3.4 Average Performance Analysis ("Method II")

In this section, we propose a method, based on knowledge of the frequency-domain channel correlation matrix, which can be used directly in order to obtain the average BER performance of coded multicarrier systems. The advantage of this method is that it allows for simple and direct evaluation of the average BER, without the need to evaluate the BER of many different channel realizations as in Method I, cf. (5.15). For simplicity, we refer to this method as "Method II" in the remainder of this chapter.

For this method we will explicitly assume that the elements of $\boldsymbol{h}$ are Rayleigh-distributed and have known correlation matrix $\boldsymbol{\Sigma_{hh}}$ (in practice, $\boldsymbol{\Sigma_{hh}}$ can be obtained from actual channel measurements, or can be numerically estimated by measuring the correlation over many realizations of a given channel model). As noted in Chapter 3, the channel models for OFDM-based UWB communication satisfy this assumption.

Average PEP

Noting that only the $\vartheta_{i,\ell}$ non-zero terms of $(\boldsymbol{x} - \boldsymbol{z}_{i,\ell})$ in (5.9) contribute to the PEP (and suppressing the dependence of ϑ on i and ℓ for notational clarity), we let $\boldsymbol{x}'$, $\boldsymbol{z}'_{i,\ell}$, $\boldsymbol{H}' = \text{diag}(\boldsymbol{h}')$, $\boldsymbol{p}'$, and $\boldsymbol{n}'$ represent the transmitted symbols, received symbols,

channel gains, interferences, and AWGN noises corresponding to the ϑ non-zero entries of $(\boldsymbol{x} - \boldsymbol{z}_{i,\ell})$, respectively, and form $\boldsymbol{\Sigma}_{\boldsymbol{h'h'}}$ by extracting the elements from $\boldsymbol{\Sigma}_{\boldsymbol{hh}}$ which correspond to $\boldsymbol{h}'$. Letting

$$\boldsymbol{D} = \text{diag}(\boldsymbol{x}' - \boldsymbol{z}'_{i,\ell}) \tag{5.17}$$

be the diagonal matrix of non-zero entries and

$$\begin{aligned} \boldsymbol{g} &= \boldsymbol{H}'(\boldsymbol{x}' - \boldsymbol{z}'_{i,\ell}) \\ &= \boldsymbol{D}\boldsymbol{h}' \ , \end{aligned} \tag{5.18}$$

we have

$$\mathbb{E}(\boldsymbol{g}) = \boldsymbol{0}_{\vartheta \times 1} \ , \tag{5.19}$$

$$\mathbb{E}(\boldsymbol{g}\boldsymbol{g}^H) = \boldsymbol{R}_{\boldsymbol{gg}} = \boldsymbol{D}\boldsymbol{\Sigma}_{\boldsymbol{h'h'}}\boldsymbol{D}^H \ , \tag{5.20}$$

i.e. the distribution of $\boldsymbol{g}$ is zero-mean complex Gaussian with covariance matrix $\boldsymbol{R}_{\boldsymbol{gg}}$.

We would like to obtain the average $\overline{\text{PEP}}_{i,\ell}$ for the ℓth error vector, starting in the ith position. Rewriting (5.9) including only the contributing terms, we obtain

$$\overline{\text{PEP}}_{i,\ell} = \Pr\left\{||\boldsymbol{r}' - \boldsymbol{H}'\boldsymbol{z}'_{i,\ell}||^2 - ||\boldsymbol{r}' - \boldsymbol{H}'\boldsymbol{x}'||^2 < 0\right\} \ , \tag{5.21}$$

$$= \Pr\left\{\boldsymbol{g}\boldsymbol{g}^H - \boldsymbol{g}(\boldsymbol{p}' + \boldsymbol{n}')^H - (\boldsymbol{p}' + \boldsymbol{n}')\boldsymbol{g}^H < 0\right\} \ ,$$

$$= \Pr\left\{\Delta_{i,\ell}(\boldsymbol{D}) < 0\right\} \ , \tag{5.22}$$

where $\Delta_{i,\ell}(\boldsymbol{D}) = \boldsymbol{y}^H\boldsymbol{A}\boldsymbol{y}$ and

$$\boldsymbol{y} = \begin{bmatrix} \boldsymbol{g} \\ \boldsymbol{p}' + \boldsymbol{n}' \end{bmatrix} \ , \qquad \boldsymbol{A} = \begin{bmatrix} \boldsymbol{I}_\vartheta & -\boldsymbol{I}_\vartheta \\ -\boldsymbol{I}_\vartheta & \boldsymbol{0}_\vartheta \end{bmatrix} \ .$$

We adopt the Laplace transform approach [95] to determine $\Pr\{\Delta_{i,\ell}(\boldsymbol{D}) < 0\}$, and consider two typical narrowband channel situations:

Case 1 — α_k constant (non-faded interferers): In this case, we note $\boldsymbol{y}$ has mean $\boldsymbol{\mu_{yy}}$ and covariance matrix $\boldsymbol{R_{yy}}$, which are given by

$$\boldsymbol{\mu_{yy}} = \mathbb{E}(\boldsymbol{y}) = \begin{bmatrix} \mathbf{0}_{\vartheta\times 1} \\ \boldsymbol{p}' \end{bmatrix} , \qquad \boldsymbol{R_{yy}} = \begin{bmatrix} \boldsymbol{R_{gg}} & \mathbf{0}_{\vartheta} \\ \mathbf{0}_{\vartheta} & \mathcal{N}_0 \boldsymbol{I}_{\vartheta} \end{bmatrix} .$$

The Laplace transform of $\Delta_{i,\ell}(\boldsymbol{D})$ is given by [96]

$$\Phi_{i,\ell}(s) = \frac{\exp[-s\boldsymbol{\mu}_{\boldsymbol{yy}}^H(\boldsymbol{A}^{-1} + s\boldsymbol{R_{yy}})^{-1}\boldsymbol{\mu_{yy}}]}{\det(\boldsymbol{I}_{2\vartheta} + s\boldsymbol{R_{yy}}\boldsymbol{A})} . \tag{5.23}$$

Case 2 — α_k independent Rayleigh faded interferers: In this case, $\mathbb{E}(\boldsymbol{y}) = \mathbf{0}_{2\vartheta\times 1}$, and we have

$$\boldsymbol{R_{yy}} = \begin{bmatrix} \boldsymbol{R_{gg}} & \mathbf{0}_{\vartheta} \\ \mathbf{0}_{\vartheta} & \boldsymbol{R_{p'p'}} + \mathcal{N}_0 \boldsymbol{I}_{\vartheta} \end{bmatrix} , \tag{5.24}$$

where $\boldsymbol{R_{p'p'}} = \mathbb{E}\left(\boldsymbol{p}'\boldsymbol{p}'^H\right)$, and the Laplace transform of $\Delta_{i,\ell}(\boldsymbol{D})$ is given by

$$\Phi_{i,\ell}(s) = \frac{1}{\det(\boldsymbol{I}_{2\vartheta} + s\boldsymbol{R_{yy}}\boldsymbol{A})} . \tag{5.25}$$

In either case, the average PEP for the ℓth error vector starting in the ith position is given by [95]

$$\overline{\mathrm{PEP}}_{i,\ell} = \Pr\{\Delta_{i,\ell}(\boldsymbol{D}) < 0\} = \frac{1}{2\pi j}\int_{c-j\infty}^{c+j\infty} \Phi_{i,\ell}(s)\frac{\mathrm{d}s}{s} , \tag{5.26}$$

where c is in the convergence region of $\Phi_{i,\ell}(s)$. We note that, for the case of independent Rayleigh faded interferers, (5.26) may be solved in closed form through the residues of

$\Phi_{i,\ell}(s)/s$ [95]. A more general technique suitable for both cases, which we have used to obtain the results in Section 5.4, is to evaluate (5.26) via numerical integration using a Gauss-Chebyshev quadrature rule [95]

$$\overline{\mathrm{PEP}}_{i,\ell} \approx \frac{1}{K} \sum_{\nu=1}^{K/2} \left(\mathrm{Re}\left\{ \Phi_{i,\ell}(cs_\nu) \right\} + \xi_\nu \mathrm{Im}\left\{ \Phi_{i,\ell}(cs_\nu) \right\} \right) \ , \tag{5.27}$$

where $s_\nu = 1 + j\xi_\nu$, $\xi_\nu = \tan([2\nu - 1]\pi/[2K])$, and K is a sufficiently large integer. We have found a good choice is $K = 200$ for the computations in Section 5.4. The real-valued parameter c should be chosen to minimize $\Phi_{i,\ell}(c)/c$, and can very quickly be determined using standard numerical techniques [97].

Average PEP without Interference

An alternative form for the average PEP can be obtained for the special case of $\boldsymbol{p} = \mathbf{0}_{N\times 1}$. Using the approach of [98], we adopt an alternate form for the Q function [98, Eq. (5)]

$$Q(x) = \frac{1}{\pi} \int_0^{\pi/2} \exp\left[-\frac{x^2}{2\sin^2\theta} \right] d\theta \tag{5.28}$$

From (5.11), and following [98, Eq. (7)], we can write the average PEP for the ℓth error vector starting in the ith position as

$$\overline{\mathrm{PEP}}_{i,\ell} = \frac{1}{\pi} \int_0^{\pi/2} \left[\det\left(\frac{E_s \boldsymbol{R}_{\boldsymbol{gg}}}{\mathcal{N}_0 \sin^2\theta} + \boldsymbol{I}_\vartheta \right) \right]^{-1} d\theta \ . \tag{5.29}$$

It can be shown that the Laplace transform approach with $\boldsymbol{p} = \mathbf{0}_{N\times 1}$ leads to an equivalent expression.

Average BER

Given the average PEP according to either (5.26) or (5.29), the corresponding bit error rate for the ℓth error vector, starting in the ith position, is given by

$$\bar{P}_{i,\ell} = a_\ell \cdot \overline{\mathrm{PEP}}_{i,\ell} \; . \tag{5.30}$$

Summing over all L error vectors, the BER for the ith starting position can be written as

$$\bar{P}_i = \sum_{\ell=1}^{L} \bar{P}_{i,\ell} \; . \tag{5.31}$$

Finally, since all starting positions are equally likely to be used, the average BER $\bar{P}$ can be written as

$$\bar{P} = \frac{1}{L_c} \sum_{i=1}^{L_c} \bar{P}_i = \frac{1}{L_c} \sum_{i=1}^{L_c} \sum_{\ell=1}^{L} \bar{P}_{i,\ell} \; . \tag{5.32}$$

Table 5.2 contains pseudocode to calculate $\bar{P}$ according to (5.32). Note that, since $\bar{P}_{i,\ell}$ in (5.32) is already averaged over $\boldsymbol{H}$, we cannot upper-bound it by 1/2 as we did in (5.14) for Method I. This implies that the result for Method II may be somewhat looser than that for Method I (see also Section 5.4.1).

5.4 Numerical Results

In this section, we present numerical results for MB-OFDM operating in the CM1 UWB channel (cf. Chapter 3). We assume the use of TFC 1 (cf. Section 2.8), and thus can consider MB-OFDM as an equivalent 384-subcarrier system. As mentioned in Section 5.2.2, for Method II we include the effect of "outer" lognormal shadowing by numerically integrating the results of (5.32) over the appropriate lognormal distribution (cf. Chapter 3).

Table 5.2: Pseudocode for Method II.

Method II	Final BER is P.
1	$\bar{P}$:= 0
2	for i := 1 to L_c do
3	for ℓ := 1 to L do
4	form $\boldsymbol{q}_{i,\ell}$ as per (5.7)
5	form $\boldsymbol{v}_{i,\ell}$ as per (5.8)
6	form $\boldsymbol{v}^{\pi}_{i,\ell}$ and $\boldsymbol{z}_{i,\ell}$ from $\boldsymbol{v}_{i,\ell}$
7	form $\boldsymbol{x'}_{i,\ell}$, $\boldsymbol{z'}_{i,\ell}$, $\boldsymbol{h'}$, $\boldsymbol{p'}$ and $\boldsymbol{\Sigma}_{\boldsymbol{h'h'}}$
8	compute $\boldsymbol{D} := \mathrm{diag}(\boldsymbol{x'} - \boldsymbol{z'}_{i,\ell})$
9	compute $\boldsymbol{g} = \boldsymbol{D}\boldsymbol{h'}$ and $\boldsymbol{R}_{\boldsymbol{gg}} := \boldsymbol{D}\boldsymbol{\Sigma}_{\boldsymbol{h'h'}}\boldsymbol{D}^H$
10	form $\boldsymbol{\mu}_{\boldsymbol{yy}}$ and/or $\boldsymbol{R}_{\boldsymbol{p'p'}}$ (as required)
11	form $\boldsymbol{R}_{\boldsymbol{yy}}$ and $\boldsymbol{A}$
12	form $\Phi_{i,\ell}(s)$ as per either (5.23) or (5.25)
13	calculate $\overline{\mathrm{PEP}}_{i,\ell}$ as per (5.26)
14	calculate $\bar{P}_{i,\ell}$ as per (5.30)
15	$\bar{P}$:= $\bar{P}$ + $\bar{P}_{i,\ell}$
16	endfor
17	endfor
18	$\bar{P}$:= $\bar{P}$ / L_c

5.4.1 No Interference

In Figure 5.4, we present the 10% outage BER as a function of $\bar{E}_b/\mathcal{N}_0$ obtained using Method I (lines), as well as simulation results (markers) for different code rates and modulation schemes using a set of 100 UWB CM1 channel realizations with lognormal shadowing, where $\bar{E}_b$ denotes the mean received energy per information bit over the ensemble of channels. We can see that Method I is able to accurately predict the outage BER for 4-QAM and 16-QAM modulation schemes and a variety of different code rates, with a maximum error of less than 0.5 dB. It is also important to note that obtaining the Method I result requires significantly less computation than is required to obtain the simulation results for all 100 UWB channel realizations. For example, it took about 15 minutes to obtain one of the analytical curves of Figure 5.4 (using a short MATLAB program), while it took approximately 48 hours to obtain the corresponding simulation

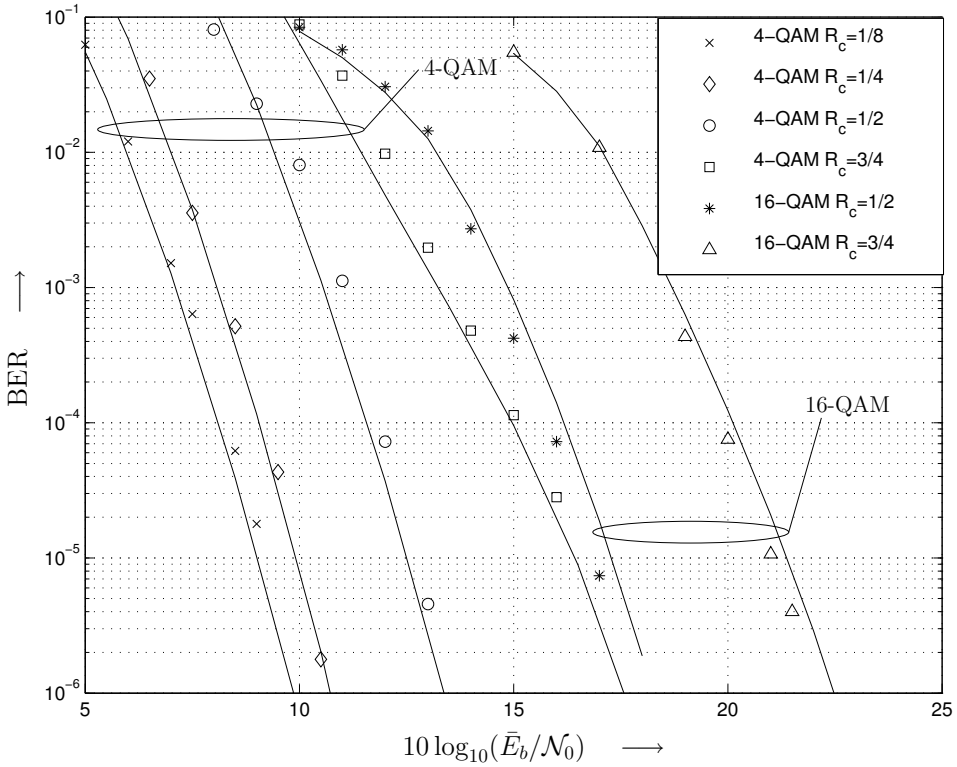

Figure 5.4: 10% outage BER vs. $\bar{E}_b/\mathcal{N}_0$ from Method I (lines) and simulation results (markers) for different code rates and modulation schemes. UWB CM1 channel. Code rates 1/4 and 1/8 include repetition. No interference ($\boldsymbol{p} = \mathbf{0}_{N\times 1}$).

results using a hand-optimized C++ MB-OFDM simulator on the same computer (with two Intel Xeon 3.6 GHz processors).

Figure 5.5 illustrates the average BER as a function of $\bar{E}_b/\mathcal{N}_0$ for 4-QAM and 16-QAM with code rates $R_c = 1/2$ and 3/4 using two approaches: Method I with an average over 10,000 channel realizations (dashed lines), and the direct average from Method II (solid lines). As expected, the two methods are in close agreement at low BER. The deviation between the two results at higher BER is due to (a) the loosening effect of the averaging of Method II over the lognormal distribution, and (b) the fact that Method I is somewhat tighter due to the upper-bounding by 1/2 in (5.14).

A Caution to System Designers: We should note that 100 channel realizations (stan-

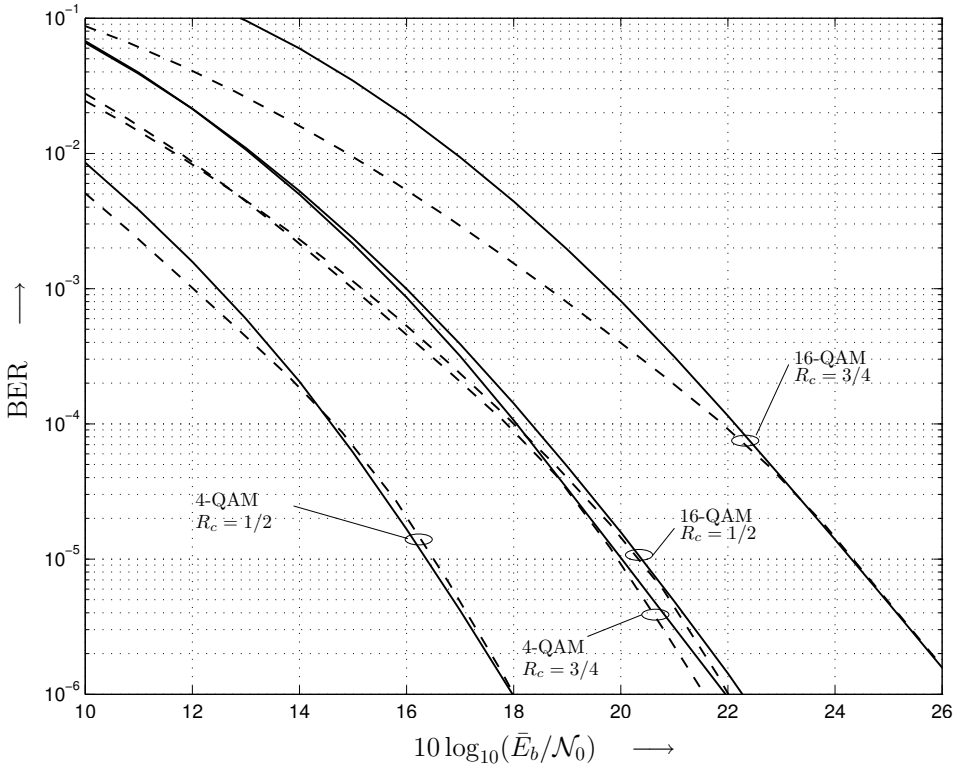

Figure 5.5: Average BER versus $\bar{E}_b/\mathcal{N}_0$ for 4-QAM and 16-QAM with code rates $R_c = 1/2$ and $3/4$. Solid lines: Direct average from Method II. Dashed lines: Method I with an average over 10,000 channel realizations. UWB CM1 channel. No interference ($\boldsymbol{p} = \mathbf{0}_{N\times 1}$).

dard for MB-OFDM performance analysis [18, 24, 28]) may not be sufficient to accurately capture the true system performance. Figure 5.6 (solid lines) shows the average BER with respect to $\bar{E}_b/\mathcal{N}_0$ for four different sets of 100 UWB CM1 channel realizations, obtained via Method I. For comparison, the average performance obtained via Method II is also shown (bold solid line). We can see that the average system performance obtained using sets of only 100 channel realizations depends greatly on the specific realizations which are chosen. Similarly, Figure 5.6 illustrates the 10% outage BER with respect to $\bar{E}_b/\mathcal{N}_0$ for four different sets of 100 UWB CM1 channel realizations, obtained via Method I (dashed lines). For comparison the 10% outage BER obtained using a set of 1000 realizations is also shown (bold dashed line). We see that the outage BER curves,

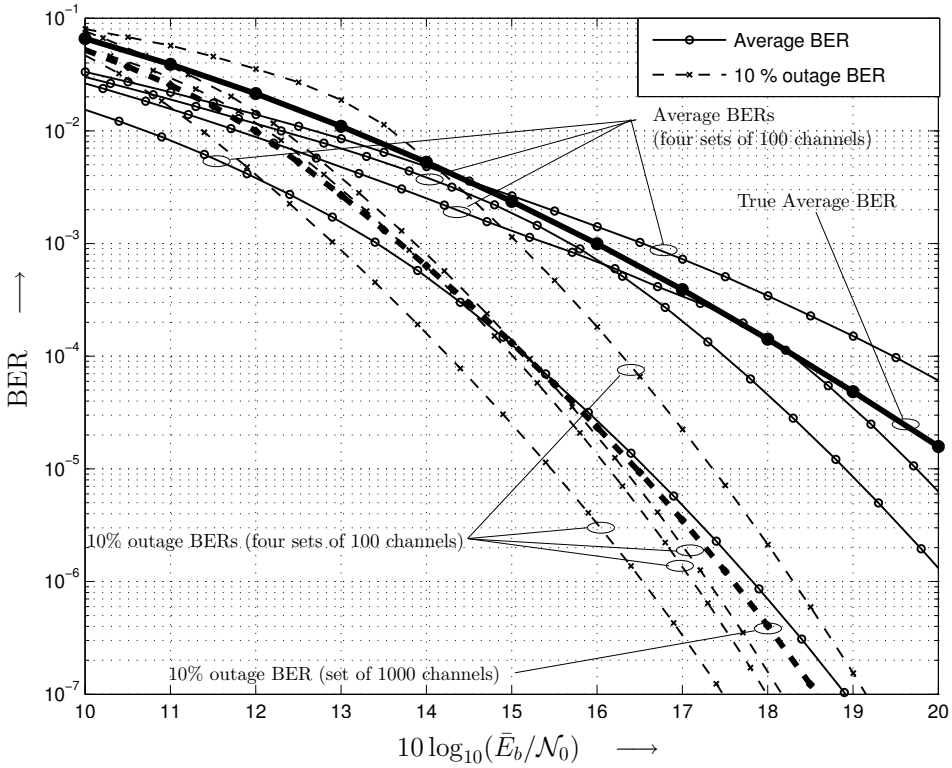

Figure 5.6: Average BER (solid lines) and 10% outage BER (dashed lines) versus $\bar{E}_b/\mathcal{N}_0$ for four different sets of 100 channels using Method I. For comparison: average BER from Method II (bold solid line), and 10% outage BER for a set of 1000 channels (bold dashed line). UWB CM1 channel, $R_c = 1/2$, 16-QAM. No interference ($\boldsymbol{p} = \mathbf{0}_{N\times 1}$).

while less variable than the average BER curves, are still quite dependent on the selected channel realization set.

Based on the results above, it seems that performance evaluation for systems operating in quasi-static channels using only small numbers of channel realizations may be prone to inaccurate results. This is one of the main strengths of the two methods presented in Section 5.3: the performance can easily be evaluated over any number of channel realizations (Method I), or the average performance can be directly obtained (Method II), without resorting to lengthy simulations.

5.4.2 Non-Faded Tone Interference

In this section, we present results for non-faded tone interference, specifically focusing on the MB-OFDM system operating at 320 Mbps ($R_c = 1/2$ after puncturing) with 4-QAM modulation over the CM1 channel. We concentrate on the case of $N_i = 1$ interferer, in order to examine the effect of the interferer frequency f_1 and the signal-to-interference ratio[2]

$$\text{SIR} = \frac{\mathbb{E}\left(||\boldsymbol{H}\boldsymbol{x}||^2\right)}{\mathbb{E}\left(||\boldsymbol{p}||^2\right)} \, . \tag{5.33}$$

Without loss of generality we place f_1 between the 52$^{\text{nd}}$ and 53$^{\text{rd}}$ MB-OFDM subcarriers.

In Figure 5.7, we consider $\bar{E}_b/\mathcal{N}_0 = 17$ dB, SIR = 19 dB, and focus on the effect of varying f_1. We show the average BER for five different sets of 100 channel realizations (dashed lines), obtained via Method I. The markers ($*$) indicate simulation results which correspond to, and are in good agreement with, the Method I results for the set of 100 channels indicated by a bold dashed line. Figure 5.7 indicates that the best-case performance is obtained when f_1 lies exactly between two OFDM subcarriers (interferer position 52.5), and the performance degrades as f_1 approaches a subcarrier frequency. We also note that, as seen in Figure 5.6 for the no-interference case, the performance obtained using Method I can be quite variable when considering small sets of channel realizations.

Figure 5.8 shows the BER versus $\bar{E}_b/\mathcal{N}_0$ for one non-faded interferer at positions 52.0 (solid lines) and 52.5 (dashed lines) with SIR $= \{28, 23, 21, 19, 17, 15\}$ dB, obtained using Method II. For comparison, the no-interference (SIR $= \infty$) performance from Method II (bold solid line) is also shown. This figure clearly illustrates the performance degradation

[2]Note that the SIR according to this definition is an average over all the subcarriers, so the SIR for a specific subcarrier may be much higher/lower than the average. For example, in the 384-subcarrier MB-OFDM system with one interferer directly on a subcarrier, the SIR of the affected subcarrier will be ≈ 26 dB lower than the average SIR (since the interference on all other subcarriers is zero).

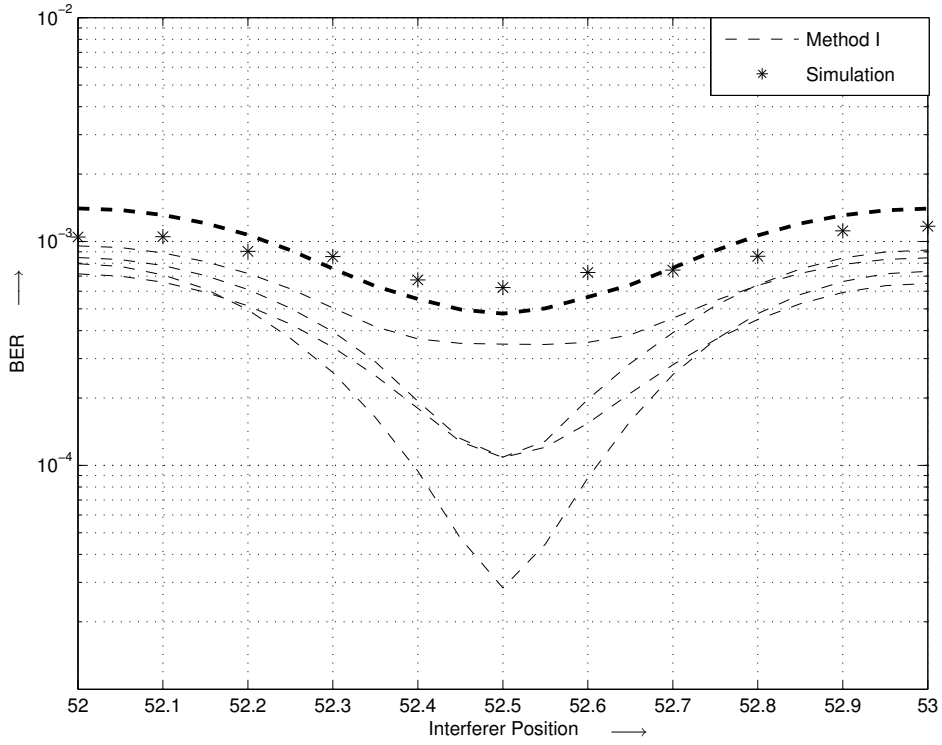

Figure 5.7: Average BER versus interferer position for $\bar{E}_b/\mathcal{N}_0 = 17$ dB and SIR = 19 dB with one non-faded interferer. Results shown: Method I with different sets of 100 channel realizations averaged over 32 phases $\phi_1 \in [0, 2\pi)$ (dashed lines); simulation results for 100 channel realizations corresponding to bold dashed line (markers). UWB CM1 channel, $R_c = 1/2$, 4-QAM.

associated with decreasing SIR. As seen in Figure 5.7, the best-case performance is obtained when f_1 lies exactly between two OFDM subcarriers, while the performance degrades as f_1 approaches a subcarrier frequency.

5.4.3 Rayleigh-faded Tone Interference

We now consider the effect of $N_i = 1$ Rayleigh-faded interferer, in order to compare the relative effects of interference with those of the non-faded interferer in Section 5.4.2. Figure 5.9 shows the BER versus $\bar{E}_b/\mathcal{N}_0$ obtained using Method II for the same interferer positions and SIR values as in Figure 5.8. By comparing Figures 5.8 and 5.9, we can

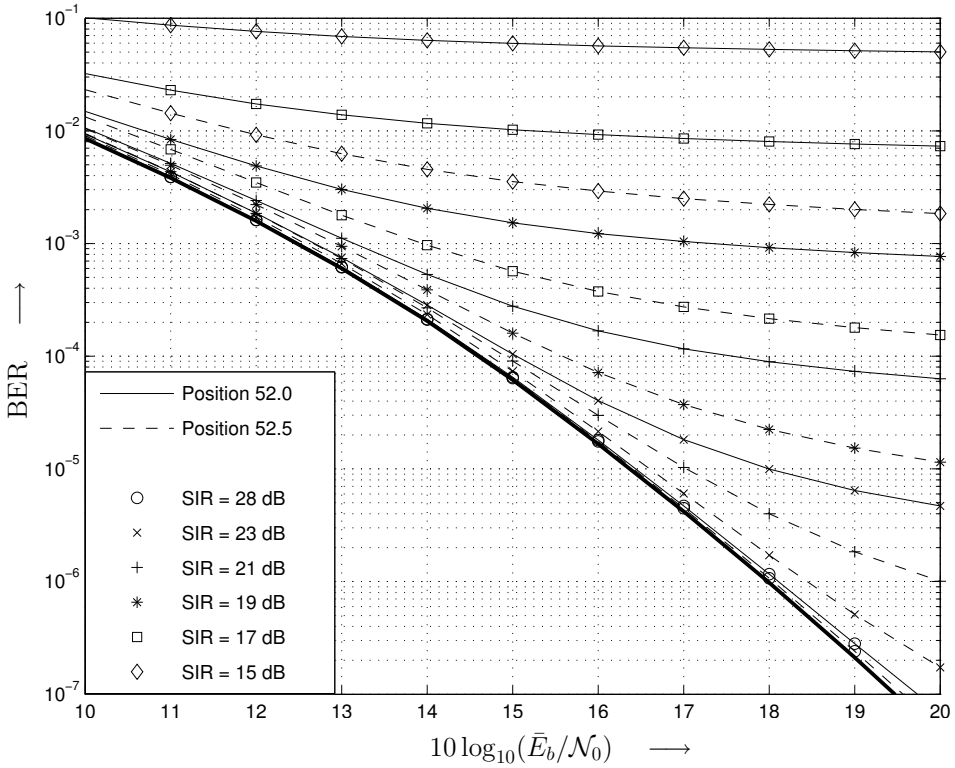

Figure 5.8: Average BER versus $\bar{E}_b/\mathcal{N}_0$ for various SIR with one non-faded interferer, obtained using Method II. Interferer positions 52.0 (solid lines) and 52.5 (dashed lines). For comparison: SIR $= \infty$ ($\boldsymbol{p} = \mathbf{0}_{N\times 1}$) from Method II (bold solid line). UWB CM1 channel, $R_c = 1/2$, 4-QAM.

clearly see that Rayleigh-faded tone interferers have a larger effect on the BER performance than non-faded tone interferers. For example, at $\bar{E}_b/\mathcal{N}_0 = 17$ dB, SIR = 21 dB and interferer position 52.5, the BER with one non-faded interferer is approximately 10^{-5}, while the BER with one Rayleigh interferer is approximately 2.3×10^{-4}. Even for relatively high SIR = 28 dB, one Rayleigh tone interferer at position 52.0 causes a much larger effect than the non-faded tone interferer at the same SIR.

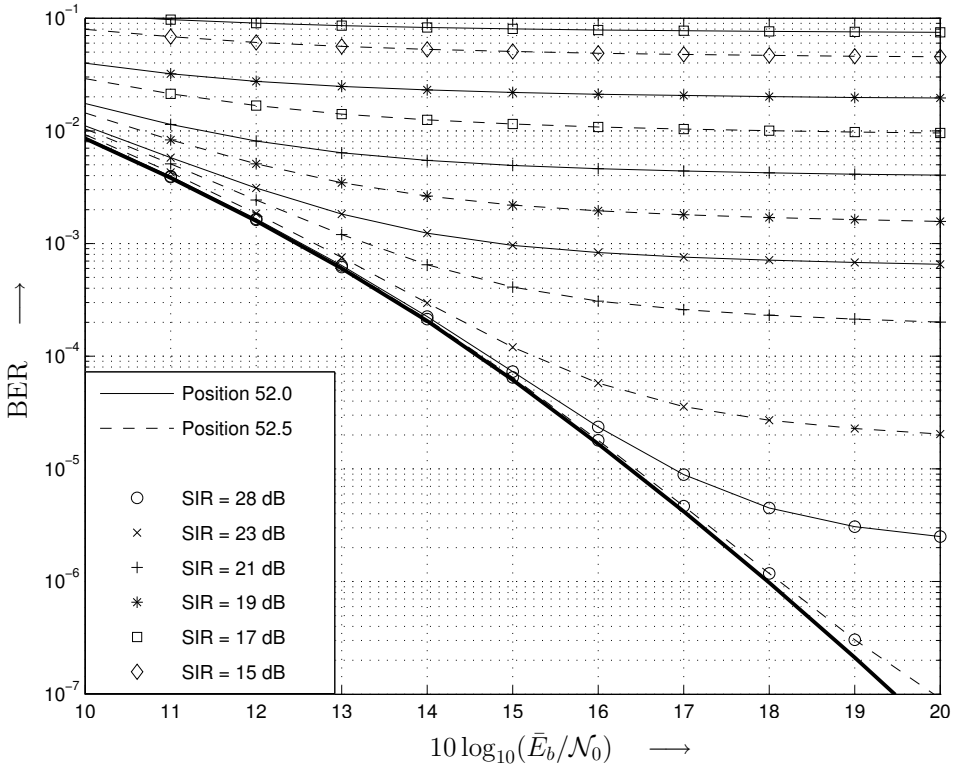

Figure 5.9: Average BER versus $\bar{E}_b/\mathcal{N}_0$ for various SIR with one Rayleigh-faded interferer, obtained using Method II. Interferer positions 52.0 (solid lines) and 52.5 (dashed lines). For comparison: SIR $= \infty$ ($\boldsymbol{p} = \mathbf{0}_{N\times 1}$) from Method II (bold solid line). UWB CM1 channel, $R_c = 1/2$, 4-QAM.

5.4.4 Interference Mitigation by Erasure Marking and Decoding

In OFDM systems where interference impacts a small number of subcarriers, one simple and practical method of interference mitigation is to erase the information bits carried on the most-affected subcarriers (proposed in e.g. [88], as well as more advanced joint marking and decoding in [89]). In order to study the potential performance of such an erasure technique, we consider the use of a genie which erases the subcarriers with largest interference powers. In the framework of analysis of Section 5.3, subcarrier erasures can be considered as additional puncturing and easily incorporated into both

analysis methods.

Figure 5.10 illustrates the average BER versus $\bar{E}_b/\mathcal{N}_0$ for 0, 1, and 2 subcarrier erasures, obtained using Method II. One non-faded interferer is placed at positions 52.25 (dashed lines) and 52.5 (solid lines), with SIR of 15 and 19 dB. As can be seen from this figure, the use of a small number of subcarrier erasures rapidly decreases the effect of the tone interference and allows the interference-impaired system performance to approach the no-interference performance (bold solid line). Focusing on the case of position 52.5 (solid lines), we can see that using only one erasure has a small effect on the resultant BER. This is due to the windowing effect of the DFT at the OFDM receiver (see Section 5.2.3), which results in interfering signal power being symmetrically distributed amongst a number of subcarriers. However, once the two largest equal-interference-power subcarriers are erased, performance improves dramatically. On the other hand, when the tone interferer is at position 52.25, a large portion of the interference power is in one subcarrier, so even one erasure can provide a substantial performance improvement. We should also note that if the interferer happens to be exactly at the subcarrier frequency, one subcarrier erasure will suffice to totally remove the effect of the interference.

We conclude by returning once again to the consideration of outage BER obtained via Method I. In Figure 5.11, we consider one non-faded interferer at position 52.5, and show the number of subcarrier erasures required to maintain the 10% outage BER $< 10^{-5}$ for varying SIR and different values of $\bar{E}_b/\mathcal{N}_0$. As expected, decreasing the SIR results in a higher required number of erasures to maintain the target BER. Unfortunately, a large number of erasures compromise the code's error correcting capability. As can be seen from Figure 5.11, eventually too many erasures weaken the code sufficiently that, even with the effects of interference mostly removed, the code is not able to maintain the required target BER. Figure 5.11 also shows that providing an increased SNR margin allows the MB-OFDM system to compensate for a larger amount of interference.

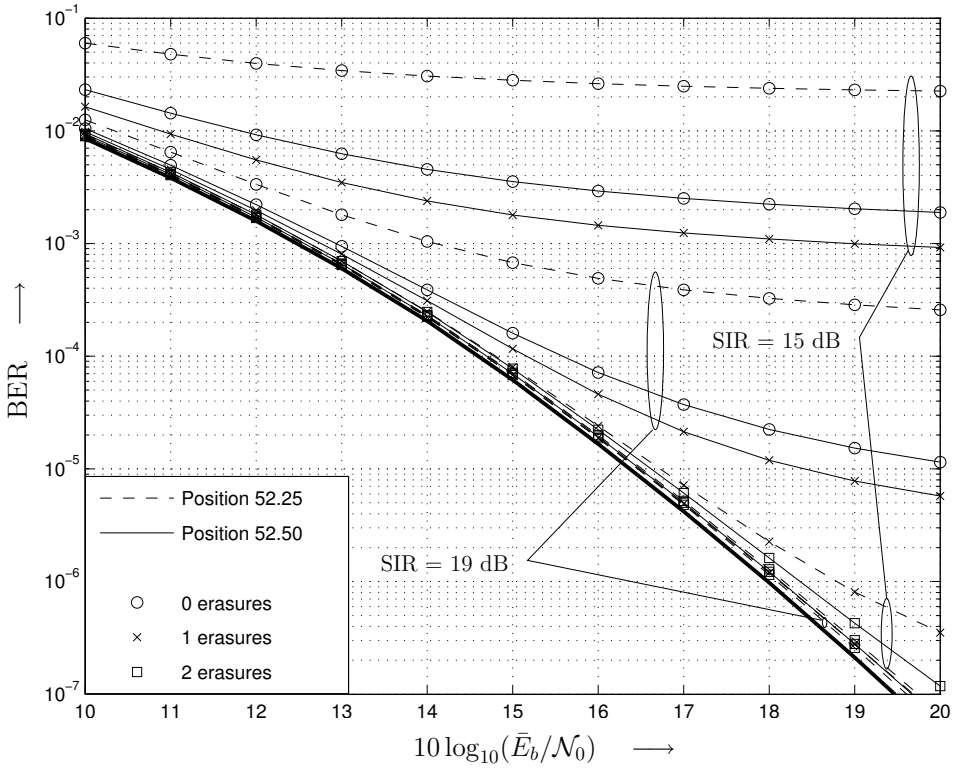

Figure 5.10: Average BER versus $\bar{E}_b/\mathcal{N}_0$ for $\{0, 1, 2\}$ subcarrier erasures. One non-faded interferer, positions 52.25 (dashed lines) and 52.5 (solid lines) and SIR = $\{15, 19\}$ dB, obtained using Method II. For comparison: SIR = ∞ ($\boldsymbol{p} = \mathbf{0}_{N\times 1}$) from Method II (bold solid line). UWB CM1 channel, $R_c = 1/2$, 4-QAM.

5.5 Conclusions

In this chapter, we have presented two methods for analyzing tone-interference-impaired MB-OFDM systems without resorting to simulations. The realization-based method ("Method I") presented in Section 5.3.3 estimates the system performance for each realization of the channel, and is suitable for evaluating the outage performance of systems. The method presented in Section 5.3.4 ("Method II"), based on knowledge of the correlation matrix of the Rayleigh-distributed frequency-domain channel gains, allows for direct calculation of the average system performance over the ensemble of quasi-static fading channel realizations.

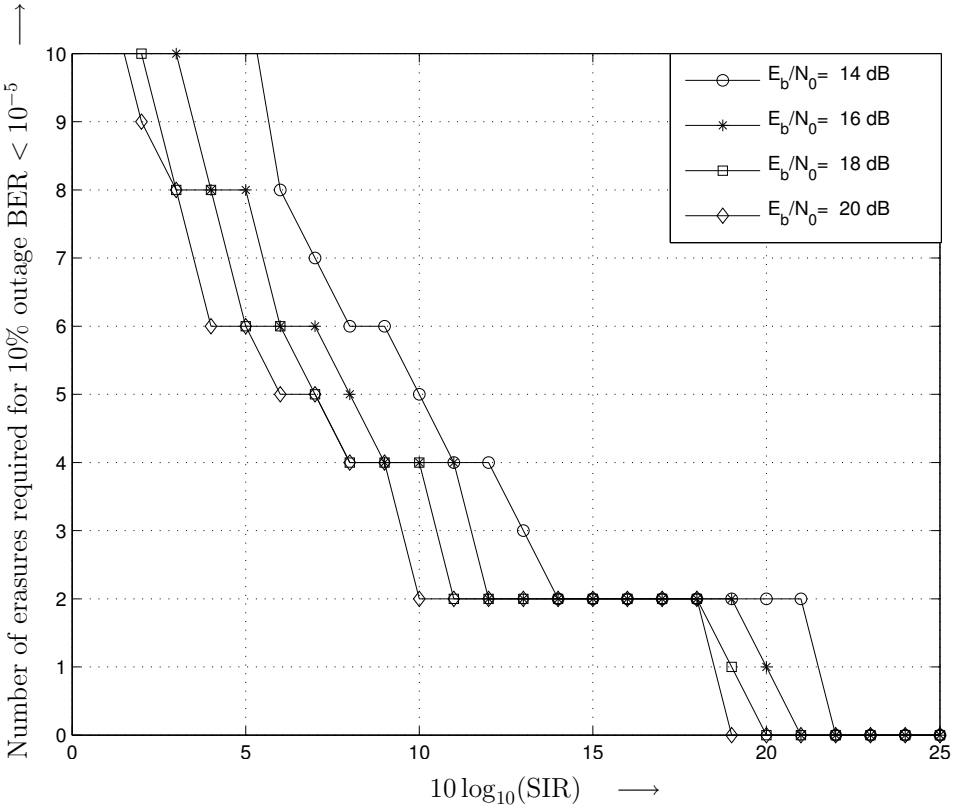

Figure 5.11: Required number of subcarrier erasures to maintain 10% outage BER $< 10^{-5}$ for various SIR and $\bar{E}_b/\mathcal{N}_0$. One non-faded interferer, position 52.5, average over 32 phases $\phi_1 \in [0, 2\pi)$, obtained using Method I with 1000 UWB CM1 channel realizations, $R_c = 1/2$, 4-QAM.

These two novel methods allow for analytical evaluation of the performance of general BICM-OFDM systems, whose performance evaluation was previously only possible via intensive numerical simulations. The results in Section 5.4 demonstrate that the proposed methods of analysis provide an accurate measure of the system performance and allow for much greater flexibility than simulation-based approaches.

We have also shown that the MB-OFDM system (and OFDM systems in general) may be significantly impacted by the effect of tone interference, but that this performance degradation can be mitigated to a large extent by the use of erasure marking and decoding at the receiver, provided that the receiver can obtain knowledge of which subcarriers are impaired by the interferers.

6 Impact of WiMAX Interference on MB-OFDM: Analysis and Mitigation

6.1 Introduction

Because UWB systems operate as spectral underlays [2, 15], they will unavoidably be impacted by the transmissions of incumbent systems. In this chapter, we consider degradation of MB-OFDM performance in the presence of interference from the WiMAX IEEE 802.16 system for wireless metropolitan area networks (WMANs), operating in the licensed 3.5 GHz band [22]. The WiMAX standard consists of both single-carrier (SC) and OFDM-based modulation schemes for use below 11 GHz. We address both modulation techniques herein.

When WiMAX is deployed in the 3.5 GHz band, it will be a source of interference for MB-OFDM systems also using this band. For this reason, there has recently been great interest in coexistence techniques between WiMAX and UWB systems [99, 100]. Recent work also examines the effects of single-carrier linearly-modulated narrowband interference signals on system design in MB-OFDM [62]. The authors of [101] consider the effect of narrowband OFDM interference on time-hopping (TH) and DS-UWB

systems. They have shown that some narrowband OFDM signals can be modeled as Gaussian interference upon the considered UWB systems. However, they do not consider OFDM-based UWB systems (such as MB-OFDM) as victim receivers. It is not immediately clear that such a Gaussian assumption holds for all forms of WiMAX interference to MB-OFDM systems, especially due to the wide range of allowable WiMAX operating bandwidths and the various modulation types. An accurate Gaussian approximation would be beneficial for both simple performance evaluation techniques and the design of interference mitigation strategies, and thus the question of the validity of this approximation motivates our work herein.

We first investigate the effect of a WiMAX system operating in the 3.5 GHz band and causing interference to an MB-OFDM system. In particular, we provide an exact analysis of the effect of the WiMAX system on the uncoded BER of the MB-OFDM system, based on Laplace transform techniques (Section 6.3). We then compare the exact analysis with a Gaussian approximation for the WiMAX interference signal (Section 6.4).

Motivated by the approximately Gaussian nature of the WiMAX interference, we propose a simple two-stage interference mitigation technique for *coded* MB-OFDM transmissions according to the ECMA-368 standard, consisting of interference spectrum estimation during silent periods followed by appropriate bit metric weighting during Viterbi decoding (Section 6.5). We compare parametric and non-parametric spectrum estimation techniques for coded MB-OFDM transmissions and WiMAX interference for various scenarios of interest (Section 6.6). The proposed two-stage interference mitigation technique is shown to be highly effective at mitigating the impact of WiMAX interference.

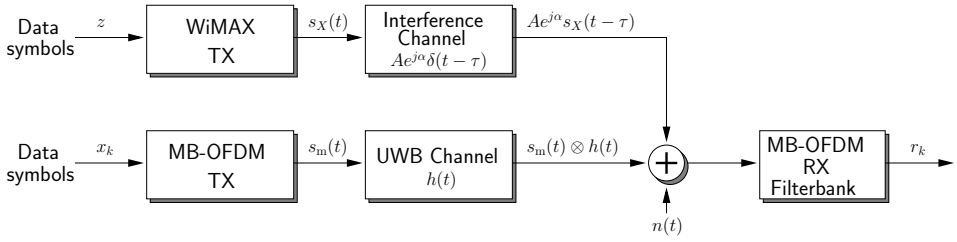

Figure 6.1: System model. $X \in \{\mathrm{n}, \mathrm{s}\}$ for WiMAX-OFDM and WiMAX-SC, respectively.

6.2 System Model

In this section, we describe the signal models for the MB-OFDM transmitter and receiver, and for the WiMAX interferer, based on the OFDM filterbank model [102], which is amenable to the analysis which is to follow. A block diagram of the system under consideration is given in Figure 6.1.

6.2.1 MB-OFDM Signal Model

The MB-OFDM transmitted signal is given by

$$s_{\mathrm{m}}(t) = \sum_{q=-\infty}^{\infty} \sum_{k=0}^{N-1} x_{k,q} \phi_k(t - qT_s) e^{j2\pi f_{\mathrm{m}} t} \,, \tag{6.1}$$

where N and T_s are the number of subcarriers and the MB-OFDM symbol duration (as given in Table 2.4), respectively, and f_{m} is the MB-OFDM carrier frequency.[1] The transmitted QPSK symbols are denoted by $x_{k,q}$, where k and q represent the subcarrier index and the MB-OFDM symbol index, respectively. The basis function for subcarrier

[1]We note that, due to the MB-OFDM frequency hopping (cf. Section 2.8), f_{m} is a function of the MB-OFDM symbol index q. However, in the sequel, we will consider the cases of (a) the presence of an in-band WiMAX interferer, and (b) the absence of such an interferer, separately, so we ignore the dependency of f_{m} on q for the time being.

k is given by

$$\phi_k(t) = \begin{cases} \frac{1}{\sqrt{T_d}} e^{j2\pi Qk(t-T_g)} & \text{if } \ t \in [0, T_s] \\ 0 & \text{else} \end{cases} , \tag{6.2}$$

where T_g, $T_d = T_s - T_g$, $Q = W/N$, and W are the durations of the guard interval and the data-carrying part of the OFDM symbol, the bandwidth per subcarrier, and the bandwidth of transmission, respectively, cf. Table 2.4.

While the MB-OFDM standard incorporates convolutional coding for error correction (cf. Section 2.1), we first focus on uncoded modulation in order to simplify the analysis. Ignoring the coding also allows us to focus on the contribution of the interference to the BER degradation, and to more clearly study possible approximations for the interference signal. We will consider interference mitigation schemes for MB-OFDM with coding according to the ECMA-368 standard in Section 6.5.

Next, we introduce the WiMAX OFDM and SC signal models.

6.2.2 WiMAX-OFDM Signal Model

The WiMAX-OFDM transmitted signal is given by

$$s_{\mathrm{n}}(t) = \sum_{\ell=-\infty}^{\infty} \sum_{d=0}^{N_{\mathrm{n}}-1} z_{d,\ell} \theta_d(t - \ell T_{\mathrm{n},s}) e^{j2\pi f_{\mathrm{n}} t} , \tag{6.3}$$

where N_{n} and $T_{\mathrm{n},s}$ are the number of subcarriers and the WiMAX-OFDM symbol duration, respectively (as given in Table 6.1), f_{n} is the WiMAX-OFDM carrier frequency, and the modulated symbols are denoted by $z_{d,\ell}$. The WiMAX standard specifies Binary Phase Shift Keying (BPSK), QPSK, 16–QAM, and 64–QAM modulation schemes [22]. We consider BPSK and QPSK in this work. The analysis for QAM schemes follows exactly the same procedure (only with more complicated expressions), and similar results will be observed. All parameters are given in Table 6.1. The basis function for

Table 6.1: Relevant WiMAX system parameters.

Parameter	**Meaning**	**Value**
WiMAX-OFDM [22]		
N_{n}	number of subcarriers	256
W_{n}	bandwidth of transmission	$\{2, 4, 6, 8, 20\}$ MHz (actual) $\{1.75, 3.5, 5.25, 7, 17.5\}$ MHz (nominal)
$T_{\mathrm{n},s}$	OFDM symbol duration	$1.25\ N_{\mathrm{n}}/W_{\mathrm{n}}$
$T_{\mathrm{n},g}$	OFDM symbol guard duration	$0.25\ N_{\mathrm{n}}/W_{\mathrm{n}}$
$T_{\mathrm{n},d}$	OFDM symbol data duration	$T_{\mathrm{n},s} - T_{\mathrm{n},g} = N_{\mathrm{n}}/W_{\mathrm{n}}$
Q_{n}	bandwidth per subcarrier	$W_{\mathrm{n}}/N_{\mathrm{n}}$
WiMAX-SC [22]		
T_p	symbol duration	$\{847.74, 411.45, 202.86, 100.71,$ $50.177, 25.044\}$ ns for bandwidths of $\{1.5625, 3.125,$ $6.25, 12.5, 25, 50\}$ MHz

subcarrier d is given by

$$\theta_d(t) = \begin{cases} \frac{1}{\sqrt{T_{\mathrm{n},d}}} e^{j2\pi Q_{\mathrm{n}} d(t-T_{\mathrm{n},g})} & \text{if} \quad t \in [0, T_{\mathrm{n},s}] \\ 0 & \text{else} \end{cases} , \tag{6.4}$$

where $T_{\mathrm{n},g}$, $T_{\mathrm{n},d} = T_{\mathrm{n},s} - T_{\mathrm{n},g}$, and Q_{n} denote the durations of the guard interval and the data-carrying part of the WiMAX-OFDM symbol, and the bandwidth per subcarrier, respectively, as given in Table 6.1.

6.2.3 WiMAX-SC Signal Model

The WiMAX-SC transmitted signal is given by

$$s_{\mathrm{s}}(t) = \sum_{\ell=-\infty}^{\infty} z_\ell p(t - \ell T_p) e^{j2\pi f_{\mathrm{s}} t} , \tag{6.5}$$

where the modulated symbols are denoted by z_ℓ, f_{s} and T_p are the WiMAX-SC carrier frequency and symbol period, respectively, and $p(t)$ denotes the square-root raised cosine

pulse shaping filter with roll-off factor 0.25 (cf. [22]). The WiMAX-SC standard specifies BPSK, QPSK, 16–QAM, 64–QAM, and 256–QAM modulation schemes [22]. Again, we consider only BPSK and QPSK in this work, but note that similar analysis can be performed for the QAM schemes and similar results will be observed.

6.2.4 Channel Models and Receiver Processing

The MB-OFDM signal passes through a channel with impulse response $h(t)$ (cf. Chapter 3). Due to the relatively small WiMAX bandwidth, and for simplicity, we consider a single-tap WiMAX channel with amplitude A and phase offset α uniformly distributed on $[0, 2\pi)$. A slowly time-varying multipath channel can be incorporated by replacing $\theta_d(t)$ and $p(t)$ with $\theta_d(t) \otimes g(t)$ and $p(t) \otimes g(t)$, respectively, where $g(t)$ is the short-term channel impulse response.

The received signal, after down-conversion to baseband and assuming that the interference signal lies in the band of interest, is given by

$$r(t) = [s_{\mathrm{m}}(t) \otimes h(t)] e^{-j2\pi f_{\mathrm{m}} t} + i(t) + n(t) \ , \tag{6.6}$$

where $n(t)$ is the complex AWGN, and

$$i(t) = A e^{j\alpha} s_X(t - \tau) e^{-j2\pi f_{\mathrm{m}} t} \ , \tag{6.7}$$

where $X \in \{\mathrm{n}, \mathrm{s}\}$ depending on whether OFDM or SC WiMAX interference is considered, τ denotes the timing offset of the WiMAX signal, which is uniformly distributed on $[0, T_X]$. For future reference, we define

$$\Delta = f_X - f_{\mathrm{m}} \tag{6.8}$$

as the separation between the carrier frequencies of the two systems.

The baseband processing consists of a filterbank matched to $\phi_k(t)$ over $[T_g, T_s]$, which, for subcarrier k, is given by

$$\psi_k(t) = \begin{cases} \phi_k^*(T_s - t) & \text{if } \ t \in [0, T_s - T_g] \\ 0 & \text{else} \end{cases} \ . \tag{6.9}$$

Without loss of generality, we consider the MB-OFDM symbol index $q = 0$, and the statistic for subcarrier k is given by

$$\begin{aligned} r_k &= (r(t) \otimes \psi_k(t))\,|_{t=T_s} \\ &= \int_{-\infty}^{\infty} r(t)\psi_k(T_s - t)\mathrm{d}t \\ &= \tilde{y}_k + \tilde{i}_k + \tilde{n}_k \ , \end{aligned} \tag{6.10}$$

where $\tilde{y}_k$, $\tilde{i}_k$, and $\tilde{n}_k$ denote the received signal, interference, and noise terms, respectively. We note that, since the basis functions $\phi_k(t)$ are orthogonal,

$$\begin{aligned} \tilde{y}_k &= \int_{T_g}^{T_s} \sum_{k'=0}^{N-1} x_{k'}\phi_{k'}(t)\phi_k^*(t)\mathrm{d}t \\ &= G_k x_k \ , \end{aligned} \tag{6.11}$$

where we have dropped the MB-OFDM symbol index $q = 0$, and $G_k = g_k e^{j\eta_k}$ denotes the frequency-domain channel gain of subcarrier k, which is the sample of the Fourier transform of $h(t)$ at frequency $(f_{\mathrm{m}} + kQ)$.

We now turn to consider the interference term, which, from (6.9) and (6.10), is given

by

$$\tilde{i}_k = \int_{T_g}^{T_s} i(t)\phi_k^*(t)\mathrm{d}t \ . \tag{6.12}$$

1) WiMAX-OFDM: The interference term can be expressed as

$$\tilde{i}_k = Ae^{j\alpha} \sum_{\ell=-\infty}^{\infty} \sum_{d=0}^{N_\mathrm{n}-1} z_{d,\ell}\beta_{k,\ell,d} \ , \tag{6.13}$$

where

$$\beta_{k,\ell,d} = \int_{T_g}^{T_s} \theta_d(t - \ell T_{\mathrm{n},s} - \tau)\phi_k^*(t)e^{j2\pi\Delta t}\mathrm{d}t \ . \tag{6.14}$$

By noting that $\theta_d(t - \ell T_{\mathrm{n},s} - \tau)$ is a complex exponential on $[\ell T_{\mathrm{n},s} + \tau, T_{\mathrm{n},s} + \ell T_{\mathrm{n},s} + \tau]$ and zero otherwise, $\beta_{k,\ell,d}$ can be expressed in closed form as

$$\beta_{k,\ell,d} = \frac{e^{j2\pi(QT_g k - Q_\mathrm{n} T_{\mathrm{n},g} d)}}{j2\pi(Q_\mathrm{n} d - Qk + \Delta)\sqrt{T_d T_{\mathrm{n},d}}} \left(e^{j2\pi(Q_\mathrm{n} d - Qk + \Delta)U} - e^{j2\pi(Q_\mathrm{n} d - Qk + \Delta)L}\right) \ , \tag{6.15}$$

where

$$L = \max(T_g, \ell T_{\mathrm{n},s} + \tau) \ ,$$

and

$$U = \min(T_s, T_{\mathrm{n},s} + \ell T_{\mathrm{n},s} + \tau) \ .$$

2) WiMAX-SC: In this case, the interference term can be expressed as

$$\tilde{i}_k = Ae^{j\alpha} \sum_{\ell=-\infty}^{\infty} z_\ell \beta_{k,\ell} \ , \tag{6.16}$$

where

$$\beta_{k,\ell} = \int_{T_g}^{T_s} p(t - \ell T_p - \tau)\phi_k^*(t)e^{j2\pi\Delta t}\mathrm{d}t \ . \tag{6.17}$$

We note that (6.17) can be solved by numerical integration, or can be written in terms of the exponential integral, as shown in Appendix A.

6.3 Performance Analysis

In this section, we provide an analysis of the uncoded BER for MB-OFDM in the presence of WiMAX interference. We begin by considering the exact analysis (Section 6.3.1), followed by a Gaussian approximation (Section 6.3.2). In Sections 6.3.3 and 6.3.4, we present the overall BER expressions including the effects of frequency hopping for the cases of non-fading and fading channels, respectively.

6.3.1 Exact BER Analysis with In-Band Interferer

Since MB-OFDM employs QPSK modulation, which can also be considered equivalently as two independent BPSK modulations. As such, and noting that both $\tilde{i}_k$ and $\tilde{n}_k$ are rotationally symmetric, we can simplify our analysis by considering $x_{k,\ell}$ as BPSK symbols in the real plane and noting that the QPSK performance will be identical.

We can form the decision variable for subcarrier k as

$$\begin{aligned} \mathrm{Re}\{e^{-j\eta_k} r_k\} &= \mathrm{Re}\{e^{-j\eta_k}\tilde{y}_k\} + \mathrm{Re}\{e^{-j\eta_k}\tilde{i}_k\} + \mathrm{Re}\{e^{-j\eta_k}\tilde{n}_k\} \\ &= y_k + i_k + n_k \ . \end{aligned} \tag{6.18}$$

Since we have assumed BPSK transmission

$$\begin{aligned} y_k &= \mathrm{Re}\{e^{-j\eta_k}\tilde{y}_k\} \\ &= g_k x_k \ , \end{aligned}$$

where

$$g_k = \mathrm{Re}\{e^{-j\eta_k} G_k\} \ , \tag{6.19}$$

while

$$n_k = \mathrm{Re}\{e^{-j\eta_k} \tilde{n}_k\} \tag{6.20}$$

is AWGN, and $i_k = \mathrm{Re}\{e^{-j\eta_k} \tilde{i}_k\}$ is given by

$$i_k = A\mathrm{Re}\left\{ e^{j(\alpha-\eta_k)} \sum_{\ell=-\infty}^{\infty} \sum_{d=0}^{N_\mathrm{n}-1} z_{d,\ell} \beta_{k,\ell,d} \right\} \qquad (\mathrm{WiMAX-OFDM}) \ , \tag{6.21}$$

or

$$i_k = A\mathrm{Re}\left\{ e^{j(\alpha-\eta_k)} \sum_{\ell=-\infty}^{\infty} z_{\ell} \beta_{k,\ell} \right\} \qquad (\mathrm{WiMAX-SC}) \ . \tag{6.22}$$

For future reference, we define the SNR as

$$\mathrm{SNR} = \frac{\mathbb{E}\{y_k^2\}}{\mathbb{E}\{2n_k^2\}} = \frac{\mathbb{E}\{g_k^2\}}{2\sigma_n^2} \ , \tag{6.23}$$

where $\sigma_n^2 = \mathbb{E}\{n_k^2\}$ is the variance of n_k (which is independent of k).

For subcarrier k, the SIR_k is defined as

$$\mathrm{SIR}_k = \frac{\mathbb{E}\{y_k^2\}}{\mathbb{E}\{2i_k^2\}} = \frac{\mathbb{E}\{g_k^2\}}{2\mathbb{E}\{A^2\}\sigma_{i,k}^2} \ , \tag{6.24}$$

where we have separated $\mathbb{E}\{A^2\}$ from $\sigma_{i,k}^2$ in order to account for possible random A, cf. Section 6.3.4, and $\sigma_{i,k}^2$ is given by

$$\begin{aligned} \sigma_{i,k}^2 &= \frac{1}{2} \sum_{\ell=-\infty}^{\infty} \sum_{d=0}^{N_\mathrm{n}-1} \mathbb{E}\left\{ |z_{d,\ell}|^2 \right\} |\beta_{k,\ell,d}|^2 \\ &= \frac{1}{2} \sum_{\ell=-\infty}^{\infty} \sum_{d=0}^{N_\mathrm{n}-1} |\beta_{k,\ell,d}|^2 \qquad (\mathrm{WiMAX-OFDM}) \ , \end{aligned} \tag{6.25}$$

or

$$\begin{aligned}\sigma_{i,k}^2 &= \frac{1}{2}\sum_{\ell=-\infty}^{\infty}\mathbb{E}\left\{|z_\ell|^2\right\}|\beta_{k,\ell}|^2 \\ &= \frac{1}{2}\sum_{\ell=-\infty}^{\infty}|\beta_{k,\ell}|^2 \qquad (\text{WiMAX}-\text{SC})\,, \end{aligned} \tag{6.26}$$

where $\mathbb{E}\left\{|z_{d,\ell}|^2\right\}=1$ and $\mathbb{E}\left\{|z_\ell|^2\right\}=1$ since the transmitted symbols have unit energy.

Given that the MB-OFDM system hops over three bands, but that the interference power in two of these bands is zero, the overall average SIR is given by

$$\text{SIR} = \frac{\mathbb{E}\{g_k^2\}}{2\cdot\mathbb{E}\{A^2\}\cdot\left(\frac{1}{3N}\sum_{k=0}^{N-1}\sigma_{i,k}^2\right)}\,. \tag{6.27}$$

The symbols x_k are equiprobable ±1 and i_k and n_k are zero mean and symmetric. Using properties of the Laplace transform [95], the probability of error for subcarrier k is given by

$$\begin{aligned}P_{e,k} &= \Pr\{(i_k+n_k)<-g_k\} \\ &= \int_{-\infty}^{-g_k} p_{i_k+n_k}(x)\mathrm{d}x \\ &= \frac{1}{2\pi j}\int_{c-j\infty}^{c+j\infty}\Phi_{i_k+n_k}(s)e^{-g_k s}\frac{\mathrm{d}s}{s}\,, \end{aligned} \tag{6.28}$$

where $p_{i_k+n_k}(x)$ and $\Phi_{i_k+n_k}(s)=\mathbb{E}\{e^{-s(i_k+n_k)}\}$ denote the pdf of (i_k+n_k) and its Laplace transform, respectively, and c is in the convergence region of $\Phi_{i_k+n_k}(s)e^{-g_k s}/s$. Due to

the independence of i_k and n_k,

$$\Phi_{i_k+n_k}(s) = \Phi_{i_k}(s)\Phi_{n_k}(s) \ , \tag{6.29}$$

and since n_k is Gaussian, its Laplace transform is [103]

$$\Phi_{n_k}(s) = \exp\left(\frac{s^2\sigma_n^2}{2}\right) \ . \tag{6.30}$$

We are left with the determination of $\Phi_{i_k}(s)$. We begin by considering the conditional Laplace transform $\Phi_{i_k|\tau,\alpha}(s) = \mathbb{E}\left\{e^{-si_k}|\tau,\alpha\right\}$, and treat the SC and OFDM cases separately.

1) WiMAX-OFDM: Since $z_{d,\ell}$ are independent, $\Phi_{i_k|\tau,\alpha}(s)$ is given by

$$\Phi_{i_k|\tau,\alpha}(s) = \prod_{\ell=-\infty}^{\infty}\prod_{d=0}^{N_{\rm n}-1}\mathbb{E}\left\{\exp\left(-s\mathrm{Re}\{Ae^{j(\alpha-\eta_k)}z_{d,\ell}\beta_{k,\ell,d}\}\right)\right\} \ .$$

Depending on whether the WiMAX-OFDM symbols $z_{d,\ell}$ are chosen from the BPSK or the QPSK constellation, we arrive at

$$\Phi_{i_k|\tau,\alpha}(s) = \prod_{\ell=-\infty}^{\infty}\prod_{d=0}^{N_{\rm n}-1}\cosh(s\mathrm{Re}\{Ae^{j(\alpha-\eta_k)}\beta_{k,\ell,d}\}) \qquad \text{(BPSK)} \ , \tag{6.31}$$

or

$$\Phi_{i_k|\tau,\alpha}(s) = \prod_{\ell=-\infty}^{\infty}\prod_{d=0}^{N_{\rm n}-1}\cosh(s\mathrm{Re}\{Ae^{j(\alpha-\eta_k)}\beta_{k,\ell,d}\})\cosh(s\mathrm{Im}\{Ae^{j(\alpha-\eta_k)}\beta_{k,\ell,d}\}) \qquad \text{(QPSK)} \ . \tag{6.32}$$

2) WiMAX-SC: Since the z_ℓ are independent, $\Phi_{i_k|\tau,\alpha}(s)$ is given by

$$\Phi_{i_k|\tau,\alpha}(s) = \prod_{\ell=-\infty}^{\infty}\mathbb{E}\left\{\exp\left(-s\mathrm{Re}\{Ae^{j(\alpha-\eta_k)}z_\ell\beta_{k,\ell}\}\right)\right\} \ .$$

Considering again the two choices of BPSK and QPSK for the symbols z_ℓ of the WiMAX-SC system, we arrive at

$$\Phi_{i_k|\tau,\alpha}(s) = \prod_{\ell=-\infty}^{\infty} \cosh(s\mathrm{Re}\{Ae^{j(\alpha-\eta_k)}\beta_{k,\ell}\}) \qquad \text{(BPSK)} \ , \tag{6.33}$$

or

$$\Phi_{i_k|\tau,\alpha}(s) = \prod_{\ell=-\infty}^{\infty} \cosh(s\mathrm{Re}\{Ae^{j(\alpha-\eta_k)}\beta_{k,\ell}\}) \cosh(s\mathrm{Im}\{Ae^{j(\alpha-\eta_k)}\beta_{k,\ell}\}) \qquad \text{(QPSK)} \ . \tag{6.34}$$

With the conditional Laplace transforms $\Phi_{i_k|\tau,\alpha}(s)$ given by (6.31)–(6.34), we can obtain the overall Laplace transform $\Phi_{i_k}(s)$. We let $\alpha' = \alpha - \eta_k$, and note that it is uniformly distributed on $[0, 2\pi)$, so that $\Phi_{i_k|\tau,\alpha'}(s) = \Phi_{i_k|\tau,\alpha}(s)$. By integrating over the distributions of α' and τ, we obtain $\Phi_{i_k}(s)$ as

$$\Phi_{i_k}(s) = \frac{1}{2\pi T_X} \int_0^{T_X} \int_0^{2\pi} \Phi_{i_k|\tau,\alpha'}(s) \mathrm{d}\alpha' \mathrm{d}\tau \ . \tag{6.35}$$

Given (6.29) – (6.35), we can now determine the probability of error for subcarrier k, given by (6.28). Unfortunately, (6.28) does not have a closed-form solution and we must resort to numerical evaluation. As in Chapter 5, this can be done efficiently via the Gauss-Chebyshev quadrature rule [95]

$$P_{e,k} \approx \frac{1}{K} \sum_{\nu=1}^{K/2} \left(\mathrm{Re}\left\{ \Phi_{i_k+n_k}(cs_\nu) e^{-g_k c s_\nu} \right\} + \xi_\nu \mathrm{Im}\left\{ \Phi_{i_k+n_k}(cs_\nu) e^{-g_k c s_\nu} \right\} \right) \ , \tag{6.36}$$

where $s_\nu = 1 + j\xi_\nu$, $\xi_\nu = \tan([2\nu - 1]\pi/[2K])$, and K is a sufficiently large integer. We have found a good choice is $K = 200$ for the computations in Section 6.4. In general, the real-valued parameter c should be chosen to minimize $\Phi_{i_k+n_k}(c)e^{-g_k c}/c$.

We have found that a simpler yet suitable choice of c is the value which minimizes $(\Phi_{i_k+n_k}(c)e^{-g_k c}/c)|_{\tau=0,\alpha=0}$, which can very quickly be determined using standard numerical techniques [97].

6.3.2 Approximate BER with In-Band Interferer

In this section we present an approximation of the BER calculated in Section 6.3.1. We make the assumption that the interference signal at subcarrier k with power $A^2\sigma_{i,k}^2$ can be modeled as an additional zero-mean Gaussian noise signal with variance $A^2\sigma_{i,k}^2$, where $\sigma_{i,k}^2$ is defined in (6.25) or (6.26). In this case, the effective noise power is given by

$$\sigma_{e,k}^2 = \sigma_n^2 + A^2\sigma_{i,k}^2 \ , \tag{6.37}$$

and the BER for subcarrier k is given by

$$P_{a,k} = Q\left(\sqrt{\frac{g_k^2}{\sigma_{e,k}^2}}\right) \ . \tag{6.38}$$

6.3.3 Overall BER Analysis for Non-Faded Channels

In this section we consider the overall BER when $A = 1$ and $g_k = 1, \quad \forall \quad k$, i.e., we consider the case of non-faded channels for both the WiMAX and MB-OFDM signals. This case is of interest because it allows us to focus attention on the effect of the interference signal on the BER, while ignoring the contribution of fading.

When the WiMAX interferer is in the band of interest to the MB-OFDM system, the BER is given by (6.36) (exact) or (6.38) (approximate). On the other hand, when the MB-OFDM system hops to a different band, the interferer is not present and the

BER is given by

$$P_{n,k} = Q\left(\sqrt{\frac{g_k^2}{\sigma_n^2}}\right) . \tag{6.39}$$

For first generation devices, MB-OFDM hops over three bands with equal average usage, and the WiMAX system of interest is found in the first band. Noting that $P_n = P_{n,k}$ is independent of k since $g_k = 1 \; \forall \; k$, the overall BER is given by

$$P = \frac{1}{3}\left(\frac{1}{N}\sum_{k=0}^{N-1} P_{Y,k}\right) + \frac{2}{3}P_n \; , \tag{6.40}$$

where $Y \in \{e, a\}$ depending on whether the exact or approximate BER expression is used for the band containing interference.

6.3.4 Overall BER Analysis for Faded Channels

In the general case, A and g_k are distributed according to probability density functions $p_A(A)$ and $p_{g_k}(g_k)$, respectively. In order to obtain the overall average BER in the presence of fading, we average (6.28), (6.38), and (6.39) over these densities.

We first consider (6.28), and take first the expectation over g_k

$$\begin{aligned} \mathbb{E}_{g_k}\{P_{e,k}\} &= \frac{1}{2\pi j}\int_{c-j\infty}^{c+j\infty} \Phi_{i_k+n_k}(s)\mathbb{E}_{g_k}\{e^{-g_k s}\}\frac{\mathrm{d}s}{s} \\ &= \frac{1}{2\pi j}\int_{c-j\infty}^{c+j\infty} \Phi_{i_k+n_k}(s)\Phi_{g_k}(s)\frac{\mathrm{d}s}{s} \; , \end{aligned} \tag{6.41}$$

where $\Phi_{g_k}(s)$ is the Laplace transform of the pdf of g_k. We note that (6.41) can again be evaluated using the Gauss-Chebyshev quadrature rule [95], cf. (6.36). The average

exact BER in the presence of in-band interference is then given by

$$\bar{P}_{e,k} = \int_0^{\infty} \frac{1}{2\pi j} \int_{c-j\infty}^{c+j\infty} \Phi_{i_k+n_k}(s)\Phi_{g_k}(s)\frac{\mathrm{d}s}{s} \; p_A(A)\mathrm{d}A \; . \tag{6.42}$$

We turn to the consideration of (6.38). We first take $\mathbb{E}_{g_k}\{P_{a,k}\}$, which, by using the alternative form of the Q-function given by (5.28), can be written as [104]

$$\begin{aligned} \mathbb{E}_{g_k}\{P_{a,k}\} &= \int_0^{\infty} Q\left(\sqrt{\frac{\gamma_k}{\sigma_{e,k}^2}}\right) p_{\gamma_k}(\gamma_k)\mathrm{d}\gamma_k \\ &= \frac{1}{\pi}\int_0^{\pi/2} M_{\gamma_k}\left(\frac{-1}{2(\sigma_n^2 + A^2\sigma_{i,k}^2)\sin^2\lambda}\right)\mathrm{d}\lambda \; , \end{aligned} \tag{6.43}$$

where $\gamma_k = g_k^2$, $p_{\gamma_k}(\gamma_k)$ is the pdf of γ_k, and $M_{\gamma_k}(s) = \mathbb{E}\left\{e^{s\gamma_k}\right\}$ is the moment generating function of γ_k [104]. We can then express the average approximate BER in the presence of in-band interference as

$$\bar{P}_{a,k} = \frac{1}{\pi}\int_0^{\infty}\int_0^{\pi/2} M_{\gamma_k}\left(\frac{-1}{2(\sigma_n^2 + A^2\sigma_{i,k}^2)\sin^2\lambda}\right)\mathrm{d}\lambda \; p_A(A)\mathrm{d}A \; . \tag{6.44}$$

Using similar techniques as with (6.43), we can express the average BER without interference as [104]

$$\bar{P}_{n,k} = \frac{1}{\pi}\int_0^{\pi/2} M_{\gamma_k}\left(\frac{-1}{2\sigma_n^2\sin^2\lambda}\right)\mathrm{d}\lambda \; . \tag{6.45}$$

Finally, the overall average BER is given by

$$\bar{P} = \frac{1}{3}\left(\frac{1}{N}\sum_{k=0}^{N-1}\bar{P}_{Y,k}\right) + \frac{2}{3}\left(\frac{1}{N}\sum_{k=0}^{N-1}\bar{P}_{n,k}\right) \; , \tag{6.46}$$

with $Y \in \{e, a\}$ depending on whether (6.42) or (6.44) is used. Note that if $p_{g_k}(g_k)$ is

independent of k, then the second term in (6.46) can be simplified as was done in (6.40). We note that the integrals with semi-infinite limits in (6.42) and (6.44) converge quite rapidly and can be truncated by using a finite upper limit without loss of accuracy.

6.4 Results for Uncoded MB-OFDM

In this section, we (a) investigate the effect of WiMAX interference on MB-OFDM systems, and (b) study the applicability of the Gaussian approximation for WiMAX interference. The latter is especially important for the design of interference mitigation schemes, and for simplified performance analysis.

6.4.1 WiMAX-OFDM Interference

Figure 6.2 shows the BER versus $10\log_{10}(\text{SIR})$ from exact analysis (lines) and the Gaussian approximation (markers) for BPSK/QPSK WiMAX-OFDM interference of varying bandwidth and for different SNR. The results for BPSK and QPSK are virtually identical, so we have only included the BPSK results in this figure. In order to isolate the effects of the interference signal, we have chosen to fix $A = 1$ and $g_k = 1 \ \forall \ k$, i.e., we consider the case of non-faded channels for both the WiMAX and MB-OFDM signals.

We can see that the Gaussian approximation is an excellent match with the exact analysis for WiMAX-OFDM interference, for all considered values of SNR, SIR, and WiMAX bandwidths. This can be justified intuitively, since all subcarriers of the WiMAX-OFDM signal contribute to each time-domain sample of the interference signal, and thus there is a natural averaging / Central Limit Theorem effect. We note that in [101], the authors found that a Gaussian approximation was not appropriate for BPSK-modulated narrowband OFDM in some ranges of interest. However, this trend is not evidenced here, likely because WiMAX-OFDM employs $N_{\text{n}} = 256$ subcarriers

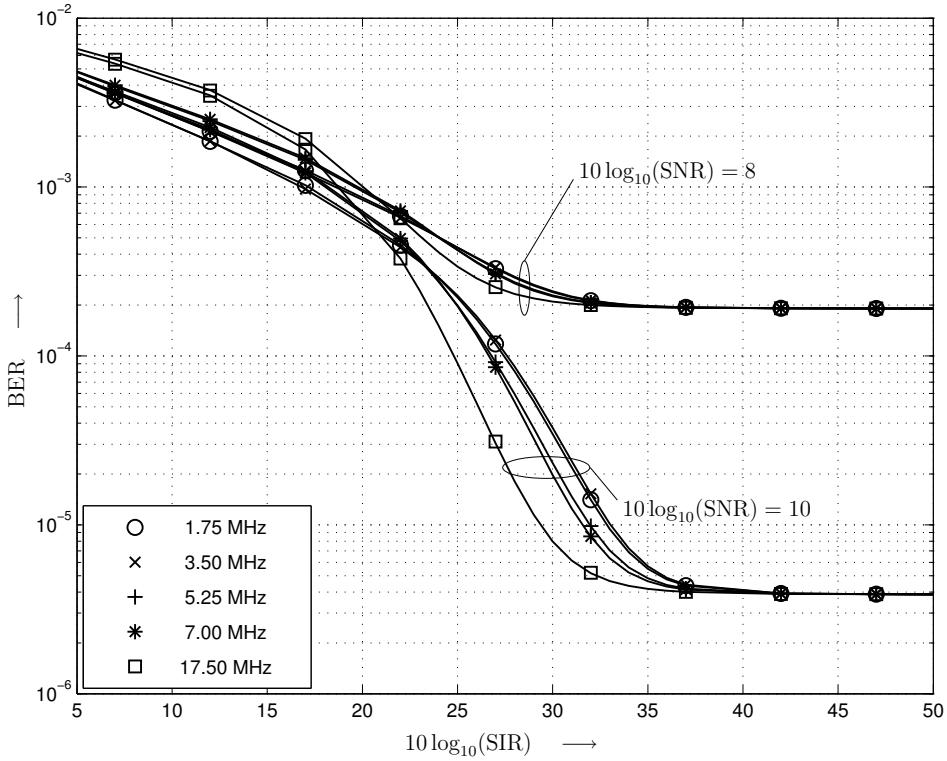

Figure 6.2: BER versus $10\log_{10}(\text{SIR})$ from exact analysis (lines) and Gaussian approximation (markers) for $10\log_{10}(\text{SNR}) \in \{8, 10\}$ and WiMAX-OFDM bandwidths of {1.75, 3.5, 5.25, 7, 17.5} MHz. BPSK WiMAX-OFDM, carrier frequency $f_{\text{n}} = 3500$ MHz. $A = 1$ and $g_k = 1 \ \forall \ k$.

versus the relatively smaller $N_{\text{n}} = 64$ of [101], which increases the averaging effect and hence the Gaussianity of the interference. We also note that, for a fixed $10\log_{10}(\text{SIR})$, the BER tends to decrease as the interferer bandwidth increases. This is because the per-subcarrier interference power decreases as the bandwidth increases (since the average interference power is constant), and thus (since the BER decays exponentially with increasing SIR_k) the values of $P_{e,k}$ also decrease with increasing interference bandwidth.

To confirm the results of the analysis, Figure 6.3 shows the BER versus $10\log_{10}(\text{SIR})$ for both the exact analysis (lines) and simulation results (markers), with non-faded channels for both the QPSK WiMAX and MB-OFDM signals. We note an excellent agreement between analysis and simulation for all considered parameters.

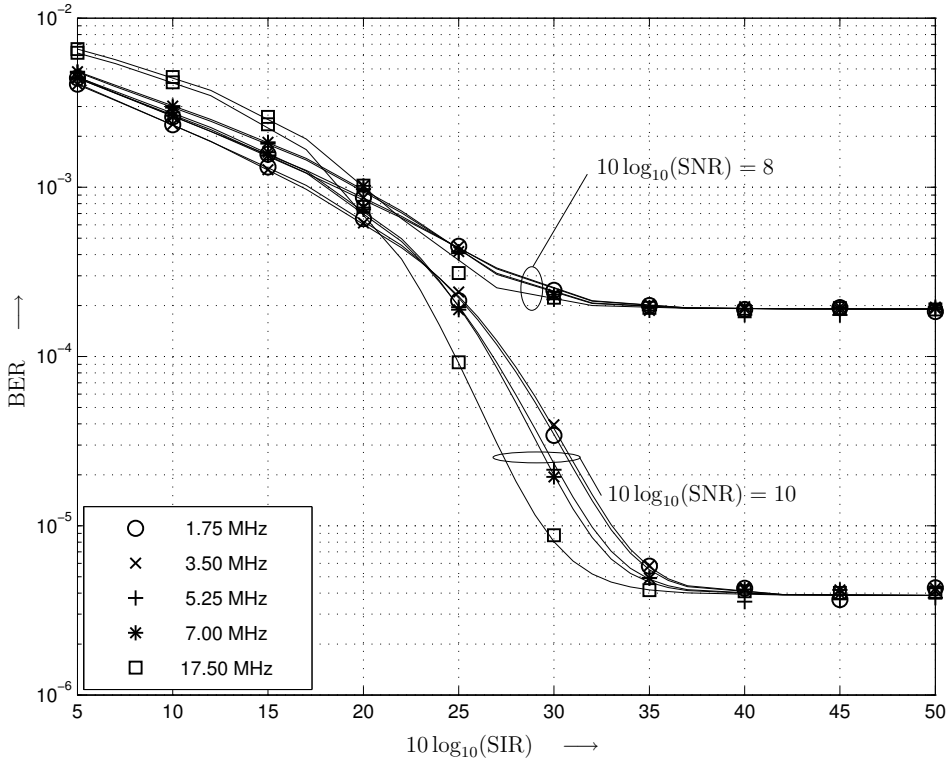

Figure 6.3: BER versus $10\log_{10}(\text{SIR})$ from exact analysis (lines) and simulation (markers) for $10\log_{10}(\text{SNR}) \in \{8, 10\}$ and WiMAX-OFDM bandwidths of {1.75, 3.5, 5.25, 7, 17.5} MHz. QPSK WiMAX-OFDM, carrier frequency $f_{\text{n}} = 3500$ MHz. $A = 1$ and $g_k = 1 \ \forall \ k$.

Finally, we consider Rayleigh distributed amplitudes g_k (a good approximation for UWB channels, as discussed in Chapter 3), with $A = 1$ (corresponding to a WiMAX transmitter in close proximity to the MB-OFDM receiver). Figure 6.4 shows the BER versus $10\log_{10}(\text{SIR})$ from both the exact analysis (lines) and the Gaussian approximation (markers). The Gaussian approximation is still an excellent match with the exact analysis. Fading in the MB-OFDM channel causes fluctuations in the instantaneous signal-to-interference ratio, which in turn decreases the distinction between different WiMAX-OFDM bandwidths at moderate to high SIR. The same fluctuations also increase the average SIR required in order to approach the interference-free error rate.

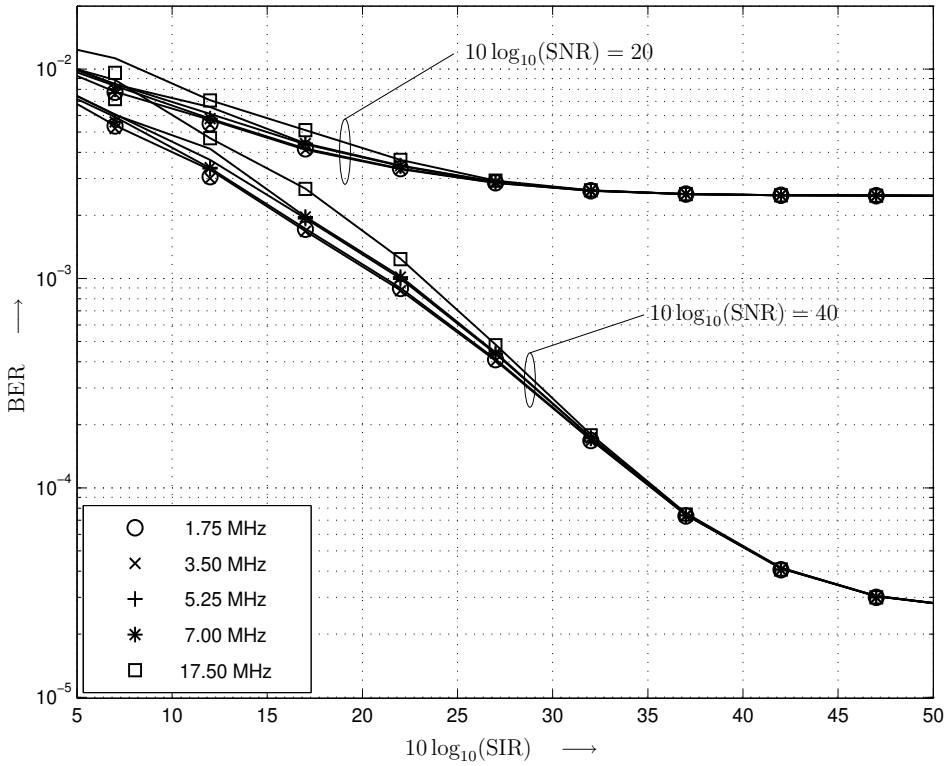

Figure 6.4: BER versus $10\log_{10}(\text{SIR})$ from exact analysis (lines) and Gaussian approximation (markers) for $10\log_{10}(\text{SNR}) \in \{20, 40\}$ and WiMAX-OFDM bandwidths of $\{1.75, 3.5, 5.25, 7, 17.5\}$ MHz. QPSK WiMAX-OFDM, carrier frequency $f_{\text{n}} = 3500$ MHz. $A = 1$, g_k Rayleigh.

6.4.2 WiMAX-SC Interference

In this section, we present numerical results illustrating the performance analysis methods applied to WiMAX-SC interference. We concentrate on the case of $A = 1$ and $g_k = 1 \; \forall \, k$, i.e., the case of non-fading channels for both the MB-OFDM and WiMAX-SC transmissions. The results below have also been confirmed via simulations, which we have omitted for clarity.

We first consider WiMAX-SC with BPSK modulation. In Figure 6.5 we plot the BER versus $10\log_{10}(\text{SIR})$ for different WiMAX-SC bandwidths, for $10\log_{10}(\text{SNR}) = 10$. We show both the exact analysis (lines) and the Gaussian approximation (markers). The Gaussian approximation is very accurate for small and large SIR, with some deviation

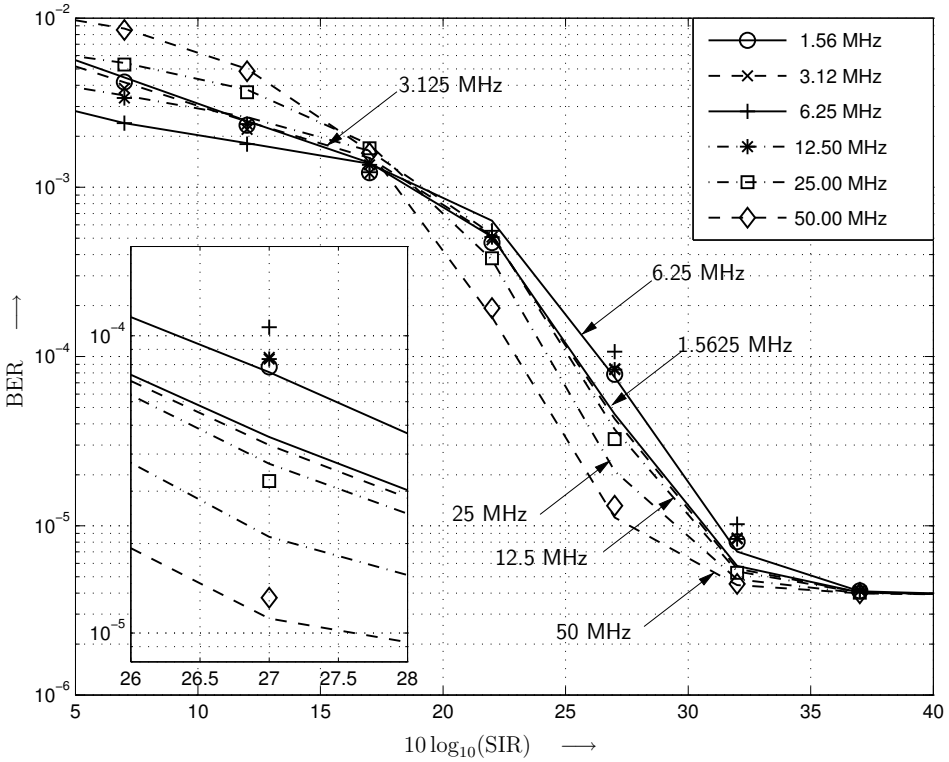

Figure 6.5: BER versus $10\log_{10}(\text{SIR})$ for $10\log_{10}(\text{SNR}) = 10$ and various WiMAX-SC bandwidths, with exact analysis (lines) and Gaussian approximation (markers). Inset: Zoomed version of same figure, showing difference between Gaussian approximation and exact BER. BPSK WiMAX-SC modulation.

at intermediate values of SIR. We can also see that the Gaussian approximation is worst for small WiMAX-SC bandwidths, and improves as the bandwidth increases. This is due to the shorter symbol time of the wide bandwidth WiMAX-SC signal, leading to a more pronounced averaging effect of the interference during one MB-OFDM symbol duration.

In Figure 6.6 we consider QPSK WiMAX modulation, and plot the BER versus $10\log_{10}(\text{SIR})$ for different WiMAX bandwidths. We can see that the Gaussian approximation is improved in comparison with Figure 6.5, due to the increased randomness of the four-phase QPSK signal. We expect the accuracy of the Gaussian approximation to continue to improve for higher-order QAM modulations.

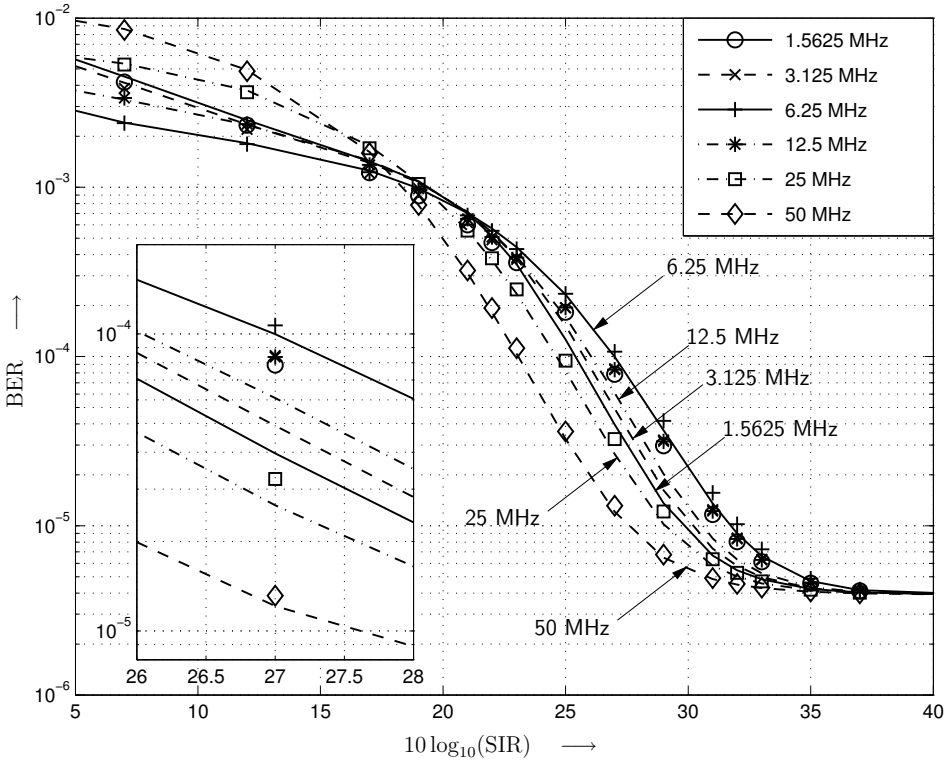

Figure 6.6: BER versus $10\log_{10}(\text{SIR})$ for $10\log_{10}(\text{SNR}) = 10$ and various WiMAX-SC bandwidths, with exact analysis (lines) and Gaussian approximation (markers). Inset: Zoomed version of same figure, showing difference between Gaussian approximation and exact BER. QPSK WiMAX-SC modulation.

6.5 Interference Mitigation for Coded MB-OFDM

It is natural to seek means to mitigate the impact of WiMAX interference on MB-OFDM systems. The results of the previous section have shown that the MB-OFDM per-subcarrier interference-plus-noise distribution in the presence of WiMAX interference behaves in an approximately Gaussian manner. Given the near-Gaussian nature of these per-subcarrier interference statistics, one natural and near-optimum technique for interference mitigation is to (1) estimate the per-subcarrier interference-plus-noise power, and (2) use this information to weigh the branch metrics fed to the Viterbi decoder, in order to suppress the interference effects. This particular technique requires

only modest increases in receiver complexity, and does not require any modifications to the MB-OFDM transmitter or signal structure. We describe each stage of the process below.

6.5.1 Interference Estimation

The MB-OFDM system will listen to the channel for interference estimation purposes, either (a) during the silent period between packet transmissions, or by (b) listening to one sub-band while operating on another sub-band. Furthermore, we assume that no other UWB devices transmit in the considered sub-band during the silent time, so that the receiver will detect only the interference-plus-noise that exists in the channel. We let P be the number of MB-OFDM symbol durations that are used to observe each sub-band.

We consider two methods for spectral estimation, described below. Both approaches adopt a time-domain estimation followed by a Fourier transform to obtain the final per-subcarrier noise variance estimates. Time-domain estimation allows us to exploit the limited degrees of freedom in the interference signal. We denote the resultant interference-plus-noise variance estimate for subcarrier k by $\hat{S}(\omega_k)$, where $\omega_k = 2\pi k/N$.

Parametric Approach

We first adopt a parametric approach by fitting the time-domain silent period observations to an autoregressive (AR) model. The fitting method is that of maximum entropy, also known as the Burg method [105]. For a given AR model order M, the Burg spectral estimate is given by

$$\hat{S}_{\text{Burg}}(\omega) = \frac{P_M}{\left|1 + \sum_{i=1}^{M} a_{M,i} e^{-ji\omega}\right|^2}, \tag{6.47}$$

where P_M and $a_{M,i}$ are the parameters of the AR model, obtained with the Levinson-Durbin algorithm [105, Sec. 9.5, pp. 414–420]. The parametric approach is generally able to use small estimation periods P. However, the performance of the method is dependent on a proper choice of model order M — smaller model orders yield less complex estimators, but may not yield suitable estimates in the presence of multiple interferers or other complicated interference scenarios.

Non-parametric Approach

We also consider a non-parametric approach to spectral estimation. We adopt the multi-taper method (MTM) [105], advocated for use in radio-scene analysis for cognitive radio [67]. In the MTM, a set of orthogonal windows (or tapers) $w_i(n)$ are applied to the observed data and the resultant estimates are averaged. In this work we adopt tapers based on the Slepian (or discrete prolate spheroidal) sequences [105, Chap. 8], which have maximal energy concentration for finite bandwidth and sample size. We use P tapers for a window of P MB-OFDM observation symbols, for a total of $N = (128 + 37)P$ samples taken at rate $T = 1/(528 \times 10^6)$ s. The MTM spectral estimate of the discrete-time observed signal $b(nT)$ is given by

$$\hat{S}_{\mathrm{MTM}}(\omega) = \frac{1}{P} \sum_{i=0}^{P-1} \left| \sum_{n=0}^{N-1} w_i(n) b(nT) e^{-j\omega nT} \right|^2 . \tag{6.48}$$

6.5.2 Interference Mitigation

The estimators given above predict the interference seen at the input to the MB-OFDM receiver FFT. However, we will mitigate the interference during decoding, after the FFT, and thus must account for the effect of the rectangular time-domain window of length

T_d. The spectrum after windowing is given by

$$\hat{S}_W(\omega) = \hat{S}_X(\omega) \otimes \left[\frac{\sin(\omega T_d)}{\omega}\right]^2 , \tag{6.49}$$

with $X \in \{\text{Burg}, \text{MTM}\}$.

As discussed in Chapter 4, MB-OFDM decoding consists of soft de-mapping, followed by de-interleaving and Viterbi decoding. Given that the interference-plus-noise per subcarrier is approximately Gaussian, we maintain the standard Euclidean distance metric, and scale the branch metrics for all bits from subcarrier k by $1/\hat{S}_W(\omega_k)$. The effect of the correlation between adjacent subcarriers is negligible due to the de-interleaving process, and can be neglected.

Note that, in the presence of purely Gaussian noise, the strategy described above is optimal. We do not simply discard information from subcarriers, but rather reduce the influence of bits which have been impacted by WiMAX interference. We note that erasure decoding (as proposed in e.g. [106] and investigated in Chapter 5) can be seen as a special case of this technique when $\hat{S}_W(\omega_k) \to \infty$ for some k.

6.6 Results for Coded MB-OFDM

In this section we present results for coded MB-OFDM systems employing the interference estimation and mitigation technique discussed in Section 6.5. We focus on the case of WiMAX-OFDM interference in order to illustrate the potential performance gains of this technique. Because we want to isolate the effects of the interference mitigation, we focus on non-fading WiMAX channels, and note that similar behaviors will be observed with fading channels. We also assume the WiMAX system is continually transmitting, i.e., we do not consider arrival/departure of WiMAX systems during the transmission

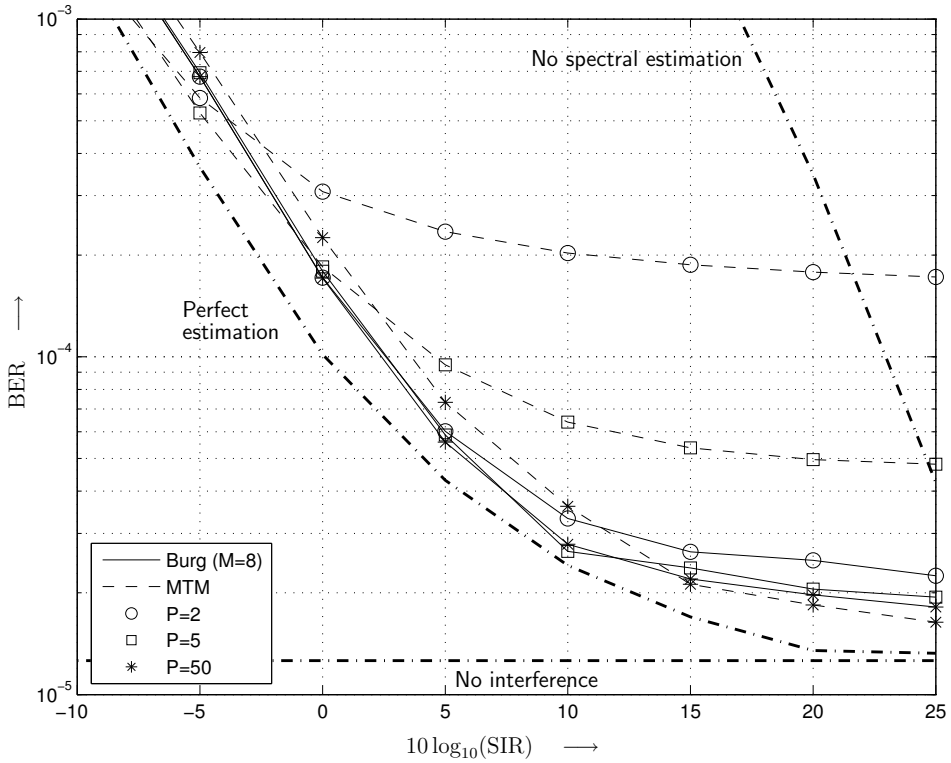

Figure 6.7: BER versus $10\log_{10}(\text{SIR})$ for $10\log_{10}(\text{SNR}) = 14.5$. MB-OFDM coded transmission with rate 1/2. QPSK WiMAX-OFDM bandwidth 7 MHz, carrier frequency $f_n = 3500$ MHz. UWB CM1 channel, non-fading WiMAX channel. Burg with $M = 8$ (solid lines) and MTM (dashed lines) spectral estimation techniques, for $P \in \{2, 5, 50\}$ symbols. For comparison: BER with no spectral estimation, perfect spectral estimation, and no interference (thick dash-dotted lines).

interval. Interference estimation is performed anew before each MB-OFDM data packet transmission, and the estimates are then fixed for the duration of the MB-OFDM packet.

In Figure 6.7, we plot the MB-OFDM BER versus $10\log_{10}(\text{SIR})$ for coded transmission with rate 1/2 and $10\log_{10}(\text{SNR}) = 14.5$. For the MB-OFDM system, we adopt the UWB channel model CM1 (cf. Chapter 3), and average over 500 channel realizations. The interferer is a QPSK WiMAX-OFDM system with bandwidth 7 MHz and carrier frequency $f_n = 3500$ MHz. We consider both the Burg with $M = 8$ (solid lines) and MTM (dashed lines) spectral estimation techniques, for $P \in \{2, 5, 50\}$ symbols. For comparison we also include the MB-OFDM BER with no spectral estimation, perfect

spectral estimation, and no interference (thick dash-dotted lines). The perfect spectral estimation curves are obtained by assuming the receiver has perfect knowledge of the noise variance σ_n^2 and interference variances $\sigma_{i,k}^2$ (given by (6.25)) when calculating the branch metric weights as described in Section 6.5.2.

We make several observations about the results in Figure 6.7. Firstly, for small numbers of estimation symbols $P \in \{2, 5\}$ the MTM estimation technique performs poorly, because such small observation lengths are not sufficient to provide reliable non-parametric estimation. On the other hand, for $P = 50$ observation symbols the MTM method is comparable to the parametric approach. Secondly, we observe that for low values of SIR, the Burg estimator performance is relatively invariant to the choice of P, while at higher SIR there are slight gains with increasing P. Finally, we note that both the parametric (with $P = 50$) and non-parametric approaches perform relatively close to the perfect estimation limit, and also provide substantial performance improvements in comparison with the case of no interference mitigation.

In Figure 6.8, we examine the effect of varying the Burg AR model order M. We adopt a non-fading MB-OFDM channel, code rate 1/2, $10\log_{10}(\text{SNR}) = 4.1$, one WiMAX-OFDM interferer with bandwidth 1.75 MHz, AR model orders $M \in \{4, 8, 16, 32\}$ and $P \in \{2, 10, 50\}$ estimation symbols. We can see that at low SIR all model orders have relatively similar performance, with $M = 4$ providing slightly better performance than for larger M. At higher SIR, increased model orders lead to better performance for $P = 50$, but poor performance for the short estimation interval $P = 2$. At intermediate values of SIR, model order $M = 4$ is insufficient, with inaccurate modeling of the interference spectrum leading to degrading performance with increasing SIR. These results indicate the importance of choosing appropriate estimation parameters M and P in order to guarantee reasonable interference mitigation performance.

We consider a more complicated interference scenario in Figure 6.9, with two WiMAX-

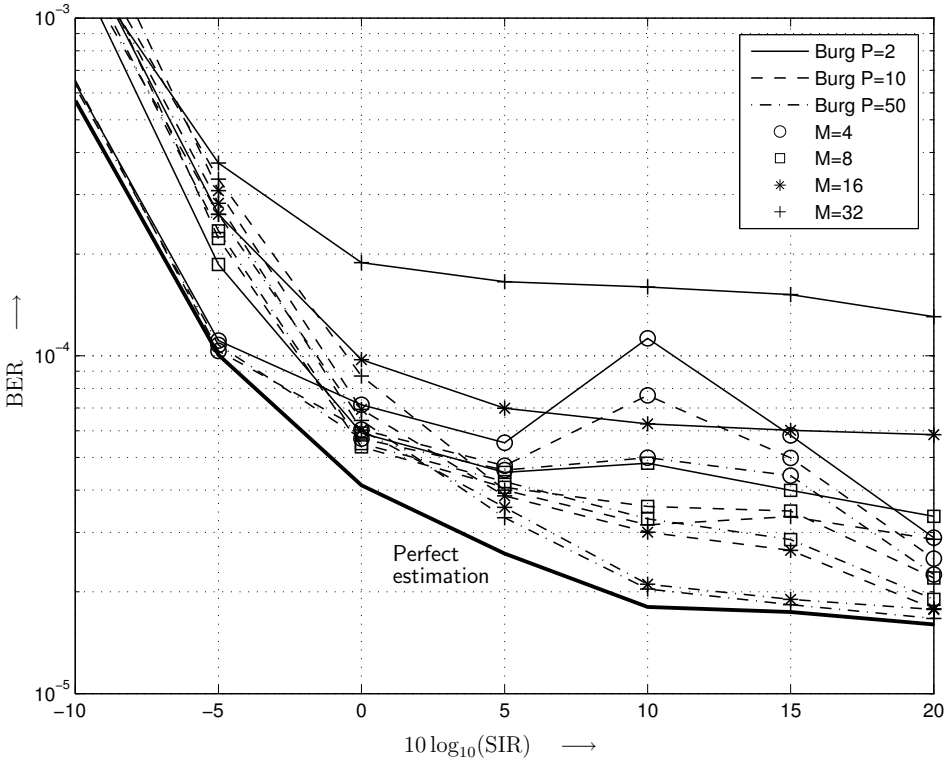

Figure 6.8: BER versus $10\log_{10}(\text{SIR})$ for $10\log_{10}(\text{SNR}) = 4.1$. MB-OFDM coded transmission with rate 1/2. QPSK WiMAX-OFDM bandwidth 1.75 MHz, carrier frequency $f_n = 3500$ MHz. Non-fading WiMAX and MB-OFDM channels. Burg spectral estimation technique, AR model orders $M \in \{4, 8, 16, 32\}$ and $P \in \{2, 5, 50\}$ symbols. For comparison: perfect spectral estimation (thick solid line).

OFDM systems operating at 3475 MHz and 3500 MHz, each with a bandwidth of 7 MHz. The MB-OFDM system operates over UWB channel CM1. We also consider a higher code rate of 3/4, which provides less error protection to the transmitted MB-OFDM data. We can see that in this case, the Burg spectral estimator with $M = 8$ does not perform well in the intermediate SIR range, due to the inability of the $M = 8$ tap AR model to accurately represent the interference spectrum. On the other hand, both the MTM and Burg with $M = 16$ perform well for all values of SIR. This result indicates that some consideration of the potential interference environment must be made in the design of interference mitigation techniques for MB-OFDM systems. In general, if larger

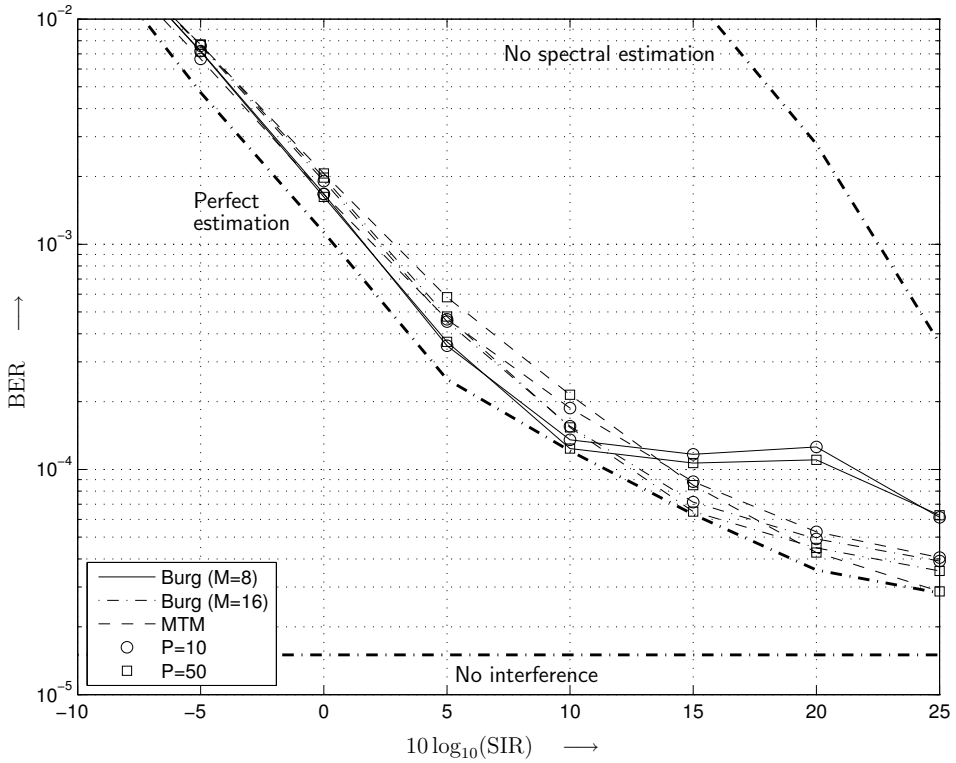

Figure 6.9: BER versus $10\log_{10}(\text{SIR})$ for $10\log_{10}(\text{SNR}) = 18$. MB-OFDM coded transmission with rate 3/4. Two QPSK WiMAX-OFDM interferers with bandwidth 7 MHz, carrier frequencies $f_n = \{3475, 3500\}$ MHz. UWB CM1 channel, non-fading WiMAX channel. Burg with $M \in \{8, 16\}$ (solid, dash-dotted lines) and MTM (dashed lines) spectral estimation techniques, for $P \in \{10, 50\}$ symbols. For comparison: BER with no spectral estimation, perfect spectral estimation, and no interference (thick dash-dotted lines).

values of P can be tolerated, the MTM estimator may be preferable, while for smaller P a Burg estimator with properly selected M offers reasonable performance.

6.7 Conclusions

Coexistence and the ability to appropriately handle interference from incumbent narrowband systems are important aspects of the design of UWB devices. The particular example of WiMAX in the 3.5 GHz band is of practical interest due to the potential for

large-scale WiMAX deployment in the near future.

In this chapter, we have presented both exact (using Laplace transform techniques) and approximate analysis of the uncoded BER of MB-OFDM in the presence of WiMAX interference. The two analysis methods are in excellent agreement, and furthermore are corroborated by simulation results. We have also shown via BER comparisons that the WiMAX interference has an approximately Gaussian behaviour on a per-subcarrier basis.

Motivated by the approximately Gaussian nature of the interference, we have presented a two-stage interference mitigation technique, consisting of interference spectral estimation followed by interference mitigation during Viterbi decoding. We have compared parametric and non-parametric approaches for several interference scenarios of practical interest. In the presence of WiMAX interference, the two-stage interference mitigation provides substantial gains in performance in return for modest increases in receiver complexity and without requiring any modifications to the MB-OFDM transmitter or signal structure. However, our results show that the expected interference environment should be carefully considered during the design of such mitigation techniques.

7 Conclusions and Future Work

In this final chapter, we summarize our results and highlight the contributions of this dissertation. We also suggest topics and open problems for further research.

7.1 Research Contributions

This dissertation as a whole has focused on several aspects of MB-OFDM UWB systems which are practically relevant, namely: (1) system performance; (2) techniques to reduce the system power requirements and/or increase the system range; (3) methods to analyze the MB-OFDM error rate without resorting to simulation techniques; and (4) the performance impact and mitigation of narrowband interference to MB-OFDM systems.

We first reviewed the channel models developed for IEEE 802.15 TG3a, conducted a study of the channel model from a frequency-domain perspective suited for OFDM transmission, and quantified several parameters of interest (Chapter 3).

In Chapter 4 we presented the results of a performance analysis of the MB-OFDM system, as well as proposed system performance enhancements through the application of advanced error correction schemes and OFDM bit-loading. Our methodology consisted of (a) development and quantification of appropriate information-theoretic performance measures, (b) comparison of these measures with simulation results for the MB-OFDM

standard as well as our proposed extensions, and (c) the consideration of the influence of practical, imperfect channel estimation on the performance. We found that MB-OFDM performs in the vicinity of the channel cutoff rate, and that our proposed extensions improve the system power efficiency by over 6 dB at a data rate of 480 Mbps, providing a 100% range increase.

We then attacked the problem of how to estimate the MB-OFDM error rate without resorting to simulations (Chapter 5). We formulated this problem in a general way, applicable to generic BICM-OFDM systems operating over quasi-static fading channels, and presented two novel analytical methods for BER estimation. In the first method, the approximate performance of the system was calculated for each realization of the channel. The second method assumed Rayleigh distributed frequency-domain subcarrier channel gains and knowledge of their correlation matrix, was suitable for directly obtaining the average BER performance. We used both methods to study the performance of a tone-interference-impaired MB-OFDM system.

In Chapter 6 another practically relevant problem, namely that of MB-OFDM performance in the presence of interference from incumbent narrowband systems, was studied. We performed an analysis of the performance of MB-OFDM in the presence of interference from WiMAX systems. We presented an exact analysis of the uncoded BER of the MB-OFDM system, as well as a simple and relatively accurate Gaussian approximation for the WiMAX interference. Motivated by the Gaussian approximation, we proposed a simple two-stage interference mitigation technique for coded MB-OFDM transmissions, consisting of interference spectrum estimation during silent periods followed by appropriate bit metric weighting during Viterbi decoding. We compared parametric and non-parametric spectrum estimation techniques for various scenarios of interest. In the presence of WiMAX interference, the two-stage interference mitigation provided substantial gains in performance in return for modest increases in complexity and without

requiring any modifications to the MB-OFDM transmitter or signal structure.

7.2 Future Work

There are several immediate extensions of the work presented in this dissertation. We present a (by no means comprehensive) list below.

The first obvious extension is to incorporate the effects of the dual-carrier modulation scheme (discussed in Section 2.4.2) into the results of all chapters. This will be decidedly non-trivial for the analysis of Chapter 5 and 6, but would be a nice addition to the results already presented herein.

As mentioned in Chapter 1, there is some previous work on the use of multiple antennas in MB-OFDM systems (cf. e.g., [39]). However, the use of multiple receive antennas to suppress narrowband interference would be an interesting topic to explore. In particular, the results of Chapter 6 could be extended to account for the possibility of multiple receive antennas in the MB-OFDM system, and interference suppression techniques could be developed using both the multiple antennas as well as the error correction decoding for improved performance.

The error rate analysis for coded multicarrier systems presented in Chapter 5 can be extended in numerous ways. The effects of bit-loading and/or power-loading could be incorporated into the analysis. In addition, other system aspects such as alternative coding schemes or multiple-input multiple-output techniques could be considered. In particular, the possible use of similar techniques to study Turbo, RA, or LDPC codes is an open problem of some interest.

A further open area is the development of detection and avoidance (DAA) techniques for UWB systems such as MB-OFDM. Recently, the regulations for UWB in Europe and Japan have mandated the use of DAA, and, since UWB devices are on the verge of being

commercialized, this regulatory requirement presents an important and timely challenge for the UWB research community. DAA can be viewed as a form of spectral agility (also referred to as cognitive radio [67]). The successful development of DAA techniques for UWB could serve as a springboard for the design of more general spectrally-agile wireless systems.

A Closed-form Expression for $\beta_{k,\ell}$ for WiMAX-SC

In (6.17), we have given an expression for the parameter $\beta_{k,\ell}$ for WiMAX-SC in terms of a single integral with finite limits. In this appendix, we give a closed-form expression for $\beta_{k,\ell}$, suitable for fast numerical evaluation.

We first make a number of notational simplifications

$$a = 4\alpha \tag{A.1}$$

$$b = \frac{\pi}{T_p} \tag{A.2}$$

$$c = \left(\frac{4\alpha}{T_p}\right)^2 \tag{A.3}$$

$$d = -2\pi(Qk - \Delta) \tag{A.4}$$

$$g = \ell T_p + \tau \tag{A.5}$$

where α is the roll-off factor of the square-root raised cosine pulse. Using the following form of the pulse

$$p(t) = \frac{4\alpha t \cos(\pi(1+\alpha)t/T_p) + T_p \sin(\pi(1-\alpha)t/T_p)}{\pi t(1-(4\alpha t/T_p)^2)}\,, \tag{A.6}$$

and by shifting the limits of integration, (6.17) can be re-written as

$$\beta_{k,\ell} = \frac{\exp(j2\pi QT_g k)}{\sqrt{T_p T_d}} \exp(jdg) \left[\zeta(T_s - g) - \zeta(T_g - g)\right] \tag{A.7}$$

where ζ is given by

$$\zeta(t) = \int \frac{e^{jdt}\left[at\cos((\alpha+1)bt) + T_p \sin((1-\alpha)bt)\right]}{\pi t - c\pi t^3} \mathrm{d}t \tag{A.8}$$

Using a computer algebra system such as Mathematica[1], we obtain the following solution

$$\begin{aligned}
\zeta(t) = \frac{1}{4\pi\sqrt{c}} \Bigg[& \exp\left(-\frac{j(b+d+b\alpha)}{\sqrt{c}}\right) \\
& \cdot \Bigg[2j\sqrt{c}\exp\left(\frac{j(b+d+b\alpha)}{\sqrt{c}}\right) T_p \mathrm{Ei}\left(j(d+b(\alpha-1))t\right) \\
& - 2j\sqrt{c}\exp\left(\frac{j(b+d+b\alpha)}{\sqrt{c}}\right) T_p \mathrm{Ei}\left(j(-\alpha b+b+d)t\right) \\
& - j\sqrt{c}\exp\left(\frac{2j(d+b\alpha)}{\sqrt{c}}\right) T_p \mathrm{Ei}\left(\frac{j(d+b(\alpha-1))(\sqrt{c}t-1)}{\sqrt{c}}\right) \\
& + j\sqrt{c}\exp\left(\frac{2j(b+d)}{\sqrt{c}}\right) T_p \mathrm{Ei}\left(-\frac{j(\alpha b-b-d)(\sqrt{c}t-1)}{\sqrt{c}}\right) \\
& - a\exp\left(\frac{2jd}{\sqrt{c}}\right) \mathrm{Ei}\left(-\frac{j(\alpha b+b-d)(\sqrt{c}t-1)}{\sqrt{c}}\right) \\
& - a\exp\left(\frac{2j(\alpha b+b+d)}{\sqrt{c}}\right) \mathrm{Ei}\left(\frac{j(\alpha b+b+d)(\sqrt{c}t-1)}{\sqrt{c}}\right) \\
& - j\sqrt{c}\exp\left(\frac{2jb}{\sqrt{c}}\right) T_p \mathrm{Ei}\left(\frac{j(d+b(\alpha-1))(\sqrt{c}t+1)}{\sqrt{c}}\right) \\
& + j\sqrt{c}\exp\left(\frac{2jb\alpha}{\sqrt{c}}\right) T_p \mathrm{Ei}\left(-\frac{j(\alpha b-b-d)(\sqrt{c}t+1)}{\sqrt{c}}\right)
\end{aligned}$$

[1]Online version available at http://integrals.wolfram.com

$$+ a \exp\left(\frac{2jb(\alpha+1)}{\sqrt{c}}\right) \mathrm{Ei}\left(-\frac{j(\alpha b+b-d)(\sqrt{c}t+1)}{\sqrt{c}}\right) + a\mathrm{Ei}\left(\frac{j(\alpha b+b+d)(\sqrt{c}t+1)}{\sqrt{c}}\right)\Bigg]\Bigg] , \quad \text{(A.9)}$$

where the exponential integral function is given by

$$\mathrm{Ei}(z) = E_1(-z) + \frac{1}{2}\left(\log(z) - \log(1/z)\right) - \log(-z) , \quad \text{(A.10)}$$

and

$$E_1(z) = \int_1^\infty \frac{e^{-zt}}{t}\mathrm{d}t \qquad \mathrm{Re}(z) > 0 . \quad \text{(A.11)}$$

We note that $E_1(z)$ can be evaluated without integration, cf. e.g. the `expint` function in Matlab.

In summary, $\beta_{k,\ell}$ can be evaluated numerically through (A.7) and (A.9)–(A.11) without any explicit numerical integration.

Bibliography

[1] John G. Proakis. *Digital Communications*. McGraw-Hill, fourth edition, 2001.

[2] Qing Zhao and Brian M. Sadler. A Survey of Dynamic Spectrum Access. *IEEE Signal Processing Mag.*, 24(3):79–89, May 2007.

[3] Terence W. Barrett. History of UltraWideBand (UWB) Radar & Communications: Pioneers and Innovators. In *Proc. Progress in Electromagnetics Symposium*, Cambridge, MA, July 2000.

[4] C. Leonard Bennett and Gerald F. Ross. Time-Domain Electromagnetics and Its Applications. *Proc. IEEE*, 66(3):299–318, March 1978.

[5] Robert A. Scholtz. Multiple Access with Time-Hopping Impulse Modulation. In *Proc. IEEE Military Communications Conf. (MILCOM)*, pages 447–450, Boston, 1993.

[6] Moe Z. Win and Robert A. Scholtz. Impulse radio: How it works. *IEEE Commun. Lett.*, 2(2):36–38, February 1998.

[7] Moe Z. Win and Robert A. Scholtz. On the Robustness of Ultra-Wide Bandwidth Signals in Dense Multipath Environments. *IEEE Commun. Lett.*, 2(2):51–53, February 1998.

[8] Moe Z. Win and Robert A. Scholtz. On the Energy Capture of Ultrawide Bandwidth Signals in Dense Multipath Environments. *IEEE Commun. Lett.*, 2(9):245–247, September 1998.

[9] Moe Z. Win and Robert A. Scholtz. Ultra Wide Bandwidth Time-Hopping Spread-Spectrum Impulse Radio for Wireless Multiple Access Communications. *IEEE Trans. Commun.*, 48(4):679–691, April 2000.

[10] Fernando Ramirez-Mireles. Performance of Ultrawideband SSMA Using Time Hopping and M-ary PPM. *IEEE J. Select. Areas Commun.*, 19(6):1186–1196, June 2001.

[11] Special Issue on Ultra-Wideband Radio in Multiaccess Wireless Communications. *IEEE J. Select. Areas Commun.*, December 2002.

[12] G. Roberto Aiello and Gerald D. Rogerson. Ultra-Wideband Wireless Systems. *IEEE Microwave*, 4(2):36–47, June 2003.

[13] Sumit Roy, Jeffrey R. Foerster, V. Srinivasa Somayazulu, and Dave G. Leeper. Ultrawideband Radio Design: The Promise of High-Speed, Short-Range Wireless Connectivity. *Proc. IEEE*, 92:295–311, February 2004.

[14] Liuqing Yang and Georgios B. Giannakis. Ultra-Wideband Communications: An Idea Whose Time Has Come. *IEEE Signal Processing Mag.*, 21(6):26–54, November 2004.

[15] Federal Communications Commission (FCC). Revision of Part 15 of the Commissions Rules Regarding Ultra-Wideband Transmission Systems. First Report and Order, ET Docket 98-153, FCC 02-48; Adopted: February 14, 2002; Released: April 22, 2002.

[16] IEEE 802.15 WPAN High Rate Alternative PHY Task Group 3a (TG3a). [Online]: http://www.ieee802.org/15/pub/TG3a.html.

[17] IEEE 802.15 WPAN Low Rate Alternative PHY Task Group 4a (TG4a). [Online]: http://www.ieee802.org/15/pub/TG4a.html.

[18] Anuj Batra *et al.* Multiband OFDM Physical Layer Proposal for IEEE 802.15 Task Group 3a. IEEE P802.15-03/268r3, March 2004.

[19] Reed Fisher, Ryuji Kohno, Michael McLaughlin, and Matt Welborn. DS-UWB Physical Layer Submission to 802.15 Task Group 3a. IEEE P802.15-04/0137r4, January 2005.

[20] John A.C. Bingham. *ADSL, VDSL, and Multicarrier Modulation*. John Wiley & Sons, 2000.

[21] IEEE 802.11. Wireless LAN Medium Access Control (MAC) Physical Layer (PHY) Specifications, Amendment 1: High-Speed Physical Layer in the 5 GHz Band, July 1999.

[22] IEEE Std 802.16-2004. Part 16: Air Interface for Fixed Broadband Wireless Access Systems, October 2004.

[23] WiMedia Alliance. [Online]: http://www.wimedia.org/.

[24] ECMA. Standard ECMA-368: High Rate Ultra Wideband PHY and MAC Standard, December 2005. [Online]: http://www.ecma-international.org/publications/standards/Ecma-368.htm.

[25] USB-IF. Certified Wireless USB. [Online]: http://www.usb.org/developers/wusb/.

[26] John A.C. Bingham. Multicarrier modulation for data transmission: An idea whose time has come. *IEEE Commun. Mag.*, 28(5):4–14, May 1990.

[27] Giuseppe Caire, Giorgio Taricco, and Ezio Biglieri. Bit-Interleaved Coded Modulation. *IEEE Trans. Inform. Theory*, 44(3):927–946, May 1998.

[28] Anuj Batra, Jaiganesh Balakrishnan, G. Roberto Aiello, Jeffrey R. Foerster, and Anand Dabak. Design of a Multiband OFDM System for Realistic UWB Channel Environments. *IEEE Trans. Microwave Theory Tech.*, 52(9):2123–2138, September 2004.

[29] Oh-Soon Shin, Saeed S. Ghassemzadeh, Larry J. Greenstein, and Vahid Tarokh. Performance Evaluation of MB-OFDM and DS-UWB Systems for Wireless Personal Area Networks. In *Proc. IEEE Intl. Conf. on Ultra-Wideband (ICUWB)*, September 2005.

[30] W. Pam Siriwongpairat, Weifeng Su, and K.J. Ray Liu. Performance Characterization of Multiband UWB Communication Systems Using Poisson Cluster Arriving Fading Paths. *IEEE J. Select. Areas Commun.*, 24(4):745–751, April 2006.

[31] Matts-Ola Wessman, Arne Svensson, and Erik Agrell. Frequency Diversity Performance of Coded Multiband-OFDM Systems on IEEE UWB Channels. In *Proc. IEEE Vehic. Tech. Conf., Fall (VTC)*, volume 2, pages 1197–1201, Los Angeles, September 2004.

[32] Matts-Ola Wessman and Arne Svensson. Performance of Coherent Impulse Radio and Multiband-OFDM on IEEE UWB Channels. In *Proc. Nordic Radio Symposium*, 2004.

[33] Brian Gaffney, Anthony D. Fagan, and Scott Rickard. Upper Bound on the Probability of Error for Repetition MB-OFDM in the Rayleigh Fading Channel. In *Proc. IEEE Intl. Conf. on Ultra-Wideband (ICUWB)*, September 2005.

[34] Iyappan Ramachandran, Yves-Paul Nakache, Philip Orlik, Andreas F. Molisch, and Jinyun Zhang. Symbol Spreading for Ultrawideband Systems Based on Multiband OFDM. In *Proc. IEEE Intl. Symposium on Personal, Indoor and Mobile Radio Communications (PIMRC)*, pages 1204–1209, Barcelona, September 2004.

[35] Xiaoming Peng, Khiam-Boon Png, and Francois Chin. Performance Improvement of Chip Interleaved Scheme for MB-OFDM System for 480Mbps. In *Proc. IEEE Vehic. Tech. Conf., Spring (VTC)*, volume 3, pages 1161–1165, May 2006.

[36] Brian Gaffney and Anthony D. Fagan. Walsh Hadamard Transform Precoded MB-OFDM: An Improved Data Rate Ultrawideband System. In *Proc. IEEE Intl. Symposium on Personal, Indoor and Mobile Radio Communications (PIMRC)*, September 2006.

[37] Liuqing Yang and Georgios B. Giannakis. Crossband Flexible UWB Multiple Access for High-Rate Multipiconet WPANs. *IEEE Trans. Commun.*, 54(11):2023–2032, November 2006.

[38] F. Berens, A. Ruegg, T. Scholand, A. Hessamian-Alinejad, and P. Jung. Fast Frequency Hopping Diversity Scheme for OFDM-Based UWB Systems. *IEE Electronics Letters*, 43(1):41–42, January 2007.

[39] W. Pam Siriwongpairat, Weifeng Su, Masoud Olfat, and K.J. Ray Liu. Multiband-OFDM MIMO Coding Framework for UWB Communication Systems. *IEEE Trans. Signal Processing*, 54(1):214–224, January 2006.

[40] W. Pam Siriwongpairat, Weifeng Su, Masoud Olfat, and K.J. Ray Liu. Space-Time-Frequency Coded Multiband UWB Communication Systems. In *Proc. IEEE Wireless Comm. & Networking Conf. (WCNC)*, volume 1, pages 426–431, March 2005.

[41] Alireza Seyedi, Vasanth Gaddam, and Dagnachew Birru. Performance of Multi-Band OFDM UWB System with Multiple Receive Antennas. In *Proc. IEEE Wireless Comm. & Networking Conf. (WCNC)*, volume 2, pages 792–797, March 2006.

[42] Thanongsak Himsoon, Weifeng Su, and K.J. Ray Liu. Multiband Differential Modulation for UWB Communication Systems. In *Proc. IEEE Global Telecomm. Conf. (GLOBECOM)*, November 2005.

[43] Khiam-Boon Png, Xiaoming Peng, and Francois Chin. Performance Studies of a Multi-band OFDM System Using a Simplified LDPC Code. In *Intl. Workshop on Ultra-Wideband Systems*, pages 376–380, May 2004.

[44] Sang-Min Kim, Jun Tang, and Keshab K. Parhi. Quasi-Cyclic Low-Density Parity-Check Coded Multiband-OFDM UWB Systems. In *Proc. Intl. Symp. on Circuits and Systems (ISCAS)*, volume 1, pages 65–68, May 2005.

[45] Zhengyuan Xu and Liu Liu. Power Allocation for Multi-band OFDM UWB Communication Networks. In *Proc. IEEE Vehic. Tech. Conf., Fall (VTC)*, volume 1, pages 368–372, September 2004.

[46] W. Pam Siriwongpairat, Zhu Han, and K.J. Ray Liu. Energy-Efficient Resource Allocation for Multiband UWB Communication Systems. In *Proc. IEEE Wireless Comm. & Networking Conf. (WCNC)*, volume 2, pages 813–818, March 2005.

[47] W. Pam Siriwongpairat, Weifeng Su, Zhu Han, and K.J. Ray Liu. Employing Cooperative Diversity for Performance Enhancement in UWB Communication Systems. In *Proc. IEEE Wireless Comm. & Networking Conf. (WCNC)*, 2006.

[48] R. Simon Sherratt and Sou Makino. Numerical Precision Requirements on the Multiband Ultra-Wideband System for Practical Consumer Electronic Devices. *IEEE Trans. Consumer Electron.*, 51(2):386–392, May 2005.

[49] Ye (Geoffrey) Li, Andreas F. Molisch, and Jinyun Zhang. Practical Approaches to Channel Estimation and Interference Suppression for OFDM-Based UWB Communications. *IEEE Trans. Wireless Commun.*, 5(9):2317–2320, September 2006.

[50] Uzoma Onunkwo, Ye (Geoffrey) Li, and Ananthram Swami. Effect of Timing Jitter on OFDM-Based UWB Systems. *IEEE J. Select. Areas Commun.*, 24(4):787–793, April 2006.

[51] Hung-Quoc Lai, W. Pam Siriwongpairat, and K.J. Ray Liu. Performance Analysis of Multiband OFDM UWB Systems with Imperfect Synchronization and Intersymbol Interference. *IEEE. J. Select. Topics in Signal Processing*, 1(3):521–534, October 2007.

[52] Chin Wee Yak, Zhongding Lei, Suttinan Chattong, and Thiang Tjeng Tjhung. Timing Synchronization for Ultra-Wideband (UWB) Multi-Band OFDM Systems. In *Proc. IEEE Vehic. Tech. Conf., Fall (VTC)*, volume 3, pages 1599–1603, September 2005.

[53] Y.-H. You, I.-T. Hwang, C.-K. Song, and H.-K. Song. PAPR Analysis for Multi-Band OFDM Signals. *IEE Electronics Letters*, 41(5):261–262, March 2005.

[54] Chin-Der Wann and Shih-Wei Yang. Modified GML Algorithm for Estimation of Signal Arrival Time in UWB Systems. In *Proc. IEEE Global Telecomm. Conf. (GLOBECOM)*, November 2006.

[55] Sung-Won Chung and Kyu-Ho Park. OFDM Symbol Shaping for Reducing D/A Requantization Error in Multiband UWB Systems. In *Proc. IEEE Vehic. Tech. Conf., Fall (VTC)*, volume 7, pages 5026–5030, September 2004.

[56] Zhongjun Wang, Wenzhen Li, Lee Guek Yeo, Yanxin Yan, Yujing Ting, and Masayuki Tomisawa. A Technique for Demapping Dual Carrier Modulated UWB OFDM Signals with Improved Performance. In *Proc. IEEE Vehic. Tech. Conf., Fall (VTC)*, volume 1, pages 38–42, September 2005.

[57] R. Simon Sherratt and Runfeng Yang. A Dual QPSK Soft-demapper for Multiband OFDM Exploiting Time-Domain Spreading and Guard Interval Diversity. *IEEE Trans. Consumer Electron.*, 53(1):46–49, January 2007.

[58] Jun Tang, Ahmed H. Tewfik, and Keshab K. Parhi. Reduced Complexity Sphere Decoding and Application to Interfering IEEE 802.15.3a Piconets. In *Proc. IEEE Intl. Conf. on Communications (ICC)*, volume 5, pages 2864–2868, June 2004.

[59] Youssef Dhibi and Thomas Kaiser. Impulsive Noise in UWB Systems and its Suppression. *Mobile Netw. Appl.*, 11:441–449, 2006.

[60] Seung Young Park, Gadi Shor, and Yong Suk Kim. Interference Resilient Transmission Scheme for Multiband OFDM System in UWB Channels. In *Proc. Intl. Symp. on Circuits and Systems (ISCAS)*, volume 5, pages 23–26, May 2004.

[61] Hirohisa Yamaguchi. Active Interference Cancellation Technique for MB-OFDM Cognitive Radio. In *Proc. 34th European Microwave Conference*, volume 2, pages 1105–1108, October 2004.

[62] Kai Shi, Yi Zhou, Burak Kelleci, Timothy Wayne Fischer, Erchin Serpedin, and Aydin Ilker Karşilayan. Impacts of Narrowband Interference on OFDM-UWB Receivers: Analysis and Mitigation. *IEEE Trans. Signal Processing*, 55(3):1118–1128, March 2007.

[63] Timothy Wayne Fischer, Burak Kelleci, Kai Shi, Aydin Ilker Karşilayan, and Erchin Serpedin. An Analog Approach to Suppressing In-Band Narrow-Band Interference in UWB Receivers. *IEEE Trans. Circuits Syst. I*, 54(5):941–950, May 2007.

[64] Shridhar Mubaraq Mishra, Robert W. Broderson, Stephan ten Brink, and Ravishankar Mahadevappa. Detect and Avoid: An Ultra-Wideband/WiMAX Coexistence Mechanism. *IEEE Commun. Mag.*, 45(6):68–75, June 2007.

[65] Kevin A. Shelby, Johann Chiang, and Jim Lansford. Modified Adjacent Frequency Coding for Increased Notch Depth in MB-OFDM under DAA/Spectral Sculpting. In *Proc. Intl. Conf. on Cognitive Radio Oriented Wireless Networks and Communications (CROWNCOM)*, pages 1–5, June 2006.

[66] Dimitrie C. Popescu and Prasad Yaddanapudi. Narrowband Interference Avoidance in OFDM-Based UWB Communication Systems. *IEEE Trans. Commun.*, 55(9):1667–1673, September 2007.

[67] Simon Haykin. Cognitive Radio: Brain-Empowered Wireless Communications. *IEEE J. Select. Areas Commun.*, 23(2):201–220, February 2005.

[68] Johann Chiang and Jim Lansford. Use of Cognitive Radio Techniques for OFDM Ultrawideband Coexistence with WiMAX. In *Proc. Texas Wireless Symposium*, pages 91–95, 2005.

[69] Anuj Batra, Srinivas Lingam, and Jaiganesh Balakrishnan. Multi-band OFDM: A Cognitive Radio for UWB. In *Proc. Intl. Symp. on Circuits and Systems (ISCAS)*, pages 4094–4097, May 2006.

[70] Bertrand Muquet, Zhengdao Wang, Georgios B. Giannakis, Marc de Courville, and Pierre Duhamel. Cyclic Prefixing or Zero Padding for Wireless Multicarrier Transmissions? *IEEE Trans. Signal Processing*, 50(12):2136–2148, December 2002.

[71] Peng Tan and Norman C. Beaulieu. A Comparison of DCT-Based OFDM and DFT-Based OFDM in Frequency Offset and Fading Channels. *IEEE Trans. Commun.*, 54(11):2113–2125, November 2006.

[72] Jeff Foerster. Channel Modeling Sub-committee Report (Final). IEEE P802.15-02/368r5-SG3a, November 2002.

[73] Andreas F. Molisch, Jeffrey R. Foerster, and Marcus Pendergrass. Channel Models for Ultrawideband Personal Area Networks. *IEEE Wireless Commun. Mag.*, 10(6):14–21, December 2003.

[74] Adel A.M. Saleh and Reinaldo A. Valenzuela. A Statistical Model for Indoor Multipath Propagation. *IEEE J. Select. Areas Commun.*, SAC-5(2):128–137, February 1987.

[75] Claude Berrou and Alain Glavieux. Near Optimum Error Correcting Coding and Decoding: Turbo-Codes. *IEEE Trans. Commun.*, 44(10):1261–1271, October 1996.

[76] Sam Dolinar and Dariush Divsalar. Weight Distribution for Turbo Codes Using Random and Nonrandom Permutations. JPL Progress Report 42-122, August 1995.

[77] Stewart Crozier and Paul Guinand. High-Performance Low-Memory Interleaver Banks for Turbo-Codes. In *Proc. IEEE Vehic. Tech. Conf., Fall (VTC)*, volume 4, pages 2394–2398, October 2001.

[78] 3GPP. 3G Technical Specification: Multiplexing and Channel Coding, TR 25.212 v6.2.0, 2004.

[79] Dariush Divsalar, Hui Jin, and Robert J. McEliece. Coding Theorems for "Turbo-Like" Codes. In *Proc. 36th Allerton Conf. on Communications, Control, and Computing*, pages 201–210, 1998.

[80] Lorenzo Piazzo. Fast Algorithm for Power and Bit Allocation in OFDM Systems. *IEE Electronics Letters*, 35(25):2173–2174, December 1999.

[81] Peter S. Chow, John M. Cioffi, and John A.C. Bingham. A Practical Discrete Multitone Transceiver Loading Algorithm for Data Transmission over Spectrally Shaped Channels. *IEEE Trans. Comm.*, 43(2/3/4):773–775, Feb-Mar-Apr. 1995.

[82] Xiaodong Cai and Georgios B. Giannakis. Error Probability Minimizing Pilots for OFDM With M-PSK Modulation Over Rayleigh-Fading Channels. *IEEE Trans. Veh. Technol.*, 53(1):146–155, January 2004.

[83] Joachim Hagenauer, Elke Offer, and Lutz Papke. Iterative Decoding of Binary Block and Convolutional Codes. *IEEE Trans. Inform. Theory*, 42(2):429–445, March 1996.

[84] David J.C. MacKay. Gallager Codes — Recent Results. Technical report, University of Cambridge. [Online] http://www.inference.phy.cam.ac.uk/mackay/.

[85] Amal Ekbal, Kee-Bong Song, and John M. Cioffi. Outage Capacity and Cut-off Rate of Bit-Interleaved Coded OFDM under Quasi-State Frequency Selective Fading. In *Proc. IEEE Global Telecomm. Conf. (GLOBECOM)*, volume 2, pages 1054–1058, December 2003.

[86] Jingxian Wu, Chengshan Xiao, and Norman C. Beaulieu. Optimal Diversity Combining Based on Noisy Channel Estimation. In *Proc. IEEE Intl. Conf. Comm. (ICC)*, volume 1, pages 214–218, June 2004.

[87] Ezio Biglieri, John Proakis, and Shlomo Shamai. Fading Channels: Information-Theoretic and Communications Aspects. *IEEE Trans. Inform. Theory*, 44(6):2619–2692, October 1998.

[88] Huaiyu Dai and H. Vincent Poor. Turbo Multiuser Dectection for Coded DMT VDSL Systems. *IEEE J. Select. Areas Commun.*, 20(2):351–362, February 2002.

[89] Tao Li, Wai Ho Mow, and Man Hung Siu. A Joint Approach to Erasure Marking and Viterbi Decoding for Impulsive Noise Channels. In *Proc. 4th IEEE Workshop on Signal Processing Advances in Wireless Communications (SPAWC)*, pages 180–184, Rome, June 2003.

[90] Israel Koffman and Vincentzio Roman. Broadband Wireless Access Solutions Based on OFDM Access in IEEE 802.16. *IEEE Commun. Mag.*, 40(6):96–103, April 2002.

[91] Esa Malkamäki and Harry Leib. Evaluating the Performance of Convolutional Codes over Block Fading Channels. *IEEE Trans. Inform. Theory*, 45(5):1643–1646, July 1999.

[92] Yiuman S. Leung, Stephen G. Wilson, and John W. Ketchum. Multifrequency Trellis Coding with Low Delay for Fading Channels. *IEEE Trans. Commun.*, 41(10):1450–1459, October 1993.

[93] Marco Chiani, Andrea Conti, and Velio Tralli. Further Results on Convolutional Code Search for Block-Fading Channels. *IEEE Trans. Inform. Theory*, 50(6):1312–1318, June 2004.

[94] Mats Cedervall and Rolf Johannesson. A Fast Algorithm for Computing Distance Spectrum of Convolutional Codes. *IEEE Trans. Inform. Theory*, 35(6):1146–1159, November 1989.

[95] Ezio Biglieri, Giuseppe Caire, Giorgia Taricco, and Javier Ventura-Traveset. Computing Error Probabilities over Fading Channels: a Unified Approach. *European Transactions on Telecommunications*, 9:15–25, January/February 1998.

[96] Mischa Schwartz, W.R. Bennett, and Seymour Stein. *Communication Systems and Techniques*. McGraw-Hill, New York, 1966.

[97] Jorge Nocedal and Stephen J. Wright. *Numerical Optimization*. Springer, 1999.

[98] Venugopal V. Veeravalli. On Performance Analysis for Signaling on Correlated Fading Channels. *IEEE Trans. Commun.*, 49(11):1879–1883, November 2001.

[99] V. Srinivasa Somayazulu, Jeffrey R. Foerster, and Richard D. Roberts. Detect and Avoid (DAA) Mechanisms for UWB Interference Mitigation. In *Proc. IEEE Intl. Conf. on Ultra-Wideband (ICUWB)*, pages 513–518, Waltham, MA, USA, September 2006.

[100] Annalisa Durantini, Romeo Giuliano, Franco Mazzenga, and Francesco Vatalaro. Performance Evaluation of Detect and Avoid Procedures for Improving UWB Coexistence with UMTS and WiMAX systems. In *Proc. IEEE Intl. Conf. on Ultra-Wideband (ICUWB)*, pages 501–506, Waltham, MA, USA, September 2006.

[101] Bo Hu and Norman C. Beaulieu. Performance of an Ultra-Wideband Communication System in the Presence of Narrowband BPSK- and QPSK-Modulated OFDM Interference. *IEEE Trans. Commun.*, 54(10):1720–1724, October 2006.

[102] Ove Edfors, Magnus Sandell, Jan-Jaap van de Beek, Daniel Landström, and Frank Sjöberg. An Introduction to Orthogonal Frequency-Division Multiplexing. [Online]: http://www.sm.luth.se/csee/sp/research/report/esb96rc.pdf, 1996.

[103] Athanasios Papoulis. *Probability, Random Variables, and Stochastic Processes*. McGraw-Hill, 2nd edition, 1984.

[104] Marvin K. Simon and Mohamed-Slim Alouini. *Digital Communication over Fading Channels*. Wiley, 2nd edition, 2005.

[105] Donald B. Percival and Andrew T. Walden. *Spectral Analysis for Physical Applications: Multitaper and Conventional Univariate Techniques*. Cambridge University Press, 1993.

[106] Tao Li, Wai Ho Mow, Vincent K.N. Lau, Manhung Siu, Roger S. Cheng, and Ross D. Murch. Robust Joint Interference Detection and Decoding for OFDM-Based Cognitive Radio Systems with Unknown Interference. *IEEE J. Select. Areas Commun.*, 25(3):566–575, April 2007.